

Electron Paramagnetic Resonance with Shaped Microwave Pulses

Dissertation
zur Erlangung des Doktorgrades
der Naturwissenschaften

vorgelegt beim Fachbereich 14
der Johann Wolfgang Goethe-Universität
in Frankfurt am Main

von

Philipp Emanuel Spindler
aus Pfaffenhofen an der Ilm

Frankfurt (2014)

D30

vom Fachbereich 14 der

Johann-Wolfgang Goethe-Universität als Dissertation angenommen

Dekan: Prof. Dr. Thomas F. Prisner

Gutachter: Prof. Dr. Thomas F. Prisner, Dr. Björn Corzilius

Datum der Disputation:

1 Abstract

Pulsed Electron Paramagnetic Resonance (EPR) spectroscopy is the most powerful tool to investigate structural properties and dynamics of paramagnetic substances. Up to date the electron spin is almost exclusively manipulated by rectangular shaped microwave pulses generated with switches. These pulses are unselective which means they excite outside their nominal bandwidth which is in most cases shallow compared to the overall spectral width of the spin system. Shaped pulses which are widely applied in NMR promise higher bandwidth and selectivity. The use of amplitude and phase modulated pulses was not possible for EPR due to the three orders of magnitude faster timescale compared to NMR. In this work, for the first time, an AWG (arbitrary waveform generator) operating with a 1 ns time resolution and 14 bit amplitude resolution was implemented into a commercial Bruker pulsed EPR spectrometer.

First results were obtained with broadband excitation pulses derived by optimum control theory (OCT). The OCT-pulse used excites transverse magnetization with 98% efficiency over a more than four times larger bandwidth than common rectangular pulse generating the same B_1 field. The benefit of such a pulse was demonstrated for magnitude FT-EPR spectroscopy on organic radicals in liquid phase.

Due to Spectrometer deadtime an FID cannot be observed for most inhomogeneous spin systems. For that reason prefocused pulses have been evaluated for their applicability to EPR spectroscopy. OCT-derived prefocused pulses can be understood as a compact Hahn Echo sequence in one monolithic pulse. Here, two problems have been encountered. 1) The limited bandwidth of the active and passive microwave components in the excitation path as well as microwave resonator cause linear distortions of the pulse shape which results in inferior pulse performance. This could be circumvented by measuring the impulse response function of the whole spin excitation path and including this information in the pulse optimization procedure. 2) Anisotropic hyperfine interaction which was not taken into account during the pulse optimization also caused efficiency losses.

PELDOR spectroscopy is a valuable tool to measure distance distributions between two or more paramagnetic centers in the range from 2-8 nm. It is demonstrated that the S/N ratio of PELDOR experiments can be substantially increased by substituting the rectangular shaped pump pulse by an adiabatic inversion pulse. The damping of the dipolar oscillations

introduced by the prolonged pump pulse towards shorter distances could be circumvented by introducing a second time reversed pump pulse.

By substituting the refocused echo of the well-known 4-pulse PELDOR with a CPMG sequence the dipolar evolution time and thus the validity of PELDOR experiments would be increased. To achieve the maximum dipolar evolution time in a CPMG PELDOR for each refocusing pulse one pump pulse has to be applied. This could only be achieved with the new adiabatic inversion pulses since multiple inversions with efficiency close to one are not possible with rectangular pulses. Even with adiabatic pump pulses a reduced efficiency was observed due to hardware limitations thus limiting the sequence to three refocusing pulses. An iterative method was developed to remove the residual dipolar signals attributed to the reduced inversion efficiency.

The new 7-pulse CPMG PELDOR sequence enabled measuring reliable distance distributions between the protomers of the trimeric betaine transporter BetP. With these it could be shown that the asymmetries found for the 2 and 3-dimensional crystal structures are even larger in frozen detergent.

2 Content

1	ABSTRACT	1
2	CONTENT	3
3	DEUTSCHE ZUSAMMENFASSUNG	5
4	INTRODUCTION	9
4.1	MOTIVATION AND AIM	9
4.2	SPIN PHYSICS	11
4.2.1	BLOCH PICTURE AND ROTATING FRAME	11
4.2.2	SPIN HAMILTONIAN	14
4.2.3	DENSITY MATRIX	17
4.2.4	TIME EVOLUTION OF THE DENSITY MATRIX	18
4.3	ADIABATIC PULSES	19
4.3.1	THE PRINCIPLE OF ADIABATICITY	19
4.3.2	THE SECH/TANH PULSE	23
4.3.4	THE WURST PULSE	25
4.4	PELDOR	29
4.4.1	THE PELDOR SIGNAL	29
4.4.2	THE PAKE DOUBLET	33
4.4.3	TIME WINDOW AND DISTANCE RESOLUTION	34
4.4.4	EFFECT OF NUCLEAR SPIN DIFFUSION ON T_2	34
4.4.5	MINIMIZING THE EFFECT OF NUCLEAR SPIN DIFFUSION BY MULTIPLE REFOCUSING	36
5	AMPLITUDE AND PHASE MODULATED MICROWAVE PULSES	39
5.1	AMPLITUDE AND PHASE MODULATION OF MICROWAVE IN THE NS REGIME	39
5.1.1	THE PULSE-SHAPING UNIT	40
5.1.2	ALTERNATIVE APPROACHES	42
5.2	IMPLEMENTING THE PULSE SHAPER INTO A BRUKER ELEXSYS E580 SPECTROMETER	43
5.3	CALIBRATION OF THE PULSE-SHAPER	47
5.4	SYNCHRONIZING THE AWG WITH THE SPECTROMETER	48
6	RESULTS AND DISCUSSION	49
6.1	BROADBAND EXCITATION OF TRANSVERSE MAGNETIZATION	49
6.1.1	BROADBAND EXCITATION OF FLORANTHENE	49
6.1.2	BROADBAND LIQUID STATE FT-EPR	53
6.1.3	LINEAR PULSE DISTORTION AND ITS EFFECT ON OPTIMAL CONTROL PREFOCUSED PULSES	56
6.1.4	SPECTROMETER IMPULSE RESPONSE FUNCTION	56
6.1.5	PREFOCUSED PULSE IN THE PRESENCE OF ANISOTROPIC HYPERFINE INTERACTION	67
6.2	BROADBAND INVERSION PELDOR SPECTROSCOPY	72
6.2.1	REQUIREMENTS ON SHAPED PULSES AS PELDOR PUMP PULSES	72

6.2.2	THE MODIFIED SECH/TANH PELDOR PUMP-PULSE	74
6.2.2	BROADBAND INVERSION PELDOR ON A BISNITROXIDE - AND COBALT(II)-PORPHYRIN-NITROXIDE-BIRADICAL.....	75
6.2.4	DISTORTION INTRODUCED BY THE OFFSET DEPENDENT ZERO TIME	80
6.3.3	OFFEST INDEPENDENT 5-PULSE SEQUENCE.....	82
6.3.4	5-PULSE PELDOR ON Co-NO BIRADICAL WITH ULTRA-WIDEBAND WURST PUMP PULSES	89
6.3	7-PULSE PELDOR FOR ENHANCED DIPOLAR WINDOW	92
6.3.1	7-PULSE CPMG-PELDOR SEQUENCE	95
6.3.2	SIGNAL FOR 7-PULSE PELDOR.....	96
6.3.3	APPLICATION OF THE 7-PULSE PELDOR SEQUENCE ON THE TRIMERIC BETAINE TRANSPORTER BETP. 100	
6.3.4	REQUIREMENTS ON PUMP PULSES FOR 7-PULSE PELDOR.....	102
6.3.5	SIGNAL ROUNDING IN 7-PULSE PELDOR	104
6.3.6	INCREMENTATION OF THE PUMP PULSES.....	104
6.3.7	SEPARATION OF THE INTERMOLECULAR AND INTRAMOLECULAR SIGNAL FOR 7-PULSE PELDOR.....	105
6.3.8	EXTRACTING THE 7-PULSE EVOLUTION ITERATIVELY.....	109
7	CONCLUSION AND OUTLOOK.....	116
8	REFERENCES.....	117
9	ACKNOWLEDGEMENT	122
10	LIST OF FIGURES.....	123
12	CURRICULUM VITAE	128
14	PUBLICATIONS.....	129

3 Deutsche Zusammenfassung

Für die bis dato ausschließlich üblichen rechteckförmigen Anregungspulse in der gepulsten ESR (Elektronen Spin Resonanz) -Spektroskopie korreliert die nutzbare Anregungsbandbreite direkt mit dem erzeugbaren B_1 Feld. In den meisten Fällen hat man es mit paramagnetischen Spezies zu tun, deren spektrale Breite bei weitem die Anregungsbandbreite der zur Verfügung stehenden Mikrowellenpulse übertrifft. Dies ist begründet mit der vor allem zu hohen Frequenzen hin sehr begrenzten Mikrowellenleistung, die nur Pulse zulässt, deren anregendes B_1 Feld wesentlich geringer ist als die spektrale Breite der untersuchten paramagnetischen Spezies. Im Rahmen dieser Arbeit wurden erstmalig amplituden- und phasenmodulierte Mikrowellenpulse in der gepulsten ESR Spektroskopie eingesetzt, um sowohl die Anregungsbandbreite, Effizienz und Selektivität gegenüber rechteckförmigen Pulsen zu erhöhen.

Der Pulsformer, welcher zum Einsatz kam, ist aus einem schnellen 2-kanaligen digital-analog Wandler aufgebaut, welcher eine Auflösung von 14 bit bei einer Taktrate von 1 GHz bietet. Mittels zweier IQ Modulatoren ist es möglich, Mikrowellenpulse im S-Band (2-4 GHz) sowie im X-Band (8-12 GHz) sowohl in Amplitude als auch in der Phase im Zeitbereich zu modulieren. Die hier präsentierten Ergebnisse wurden an einem kommerziellen BRUKER E580 Puls-ESR Spektrometer erzielt, in welches der Pulsformer implementiert wurde.

Zu einem wesentlichen Teil besteht die vorliegende Arbeit aus Vergleichen von für die EPR neuen Anregungsschemas mit den konventionellen rechteckförmigen Pulsen gleicher Mikrowellenleistung. Die am Ende vorgestellte Symbiose aus PELDOR Spektroskopie mit einer CPMG Beobachtungs-Sequenz ist jedoch erst durch die für die ESR-Spektroskopie neuen Pulse möglich geworden.

In Kapitel 6.1 geht es um breitbandige Anregung transversaler Magnetisierung. Die gezeigten Anregungsspektren wurden mit einer sehr schmalbandigen Perylen Probe erstellt, die es erlaubte, durch Variation des B_0 -Feldes das Anregungsprofil abzutasten. Es konnte gezeigt werden, dass ein mittels Optimum Control Theory (OCT) optimierter Puls über einen Bereich von 200 MHz in der Lage ist, thermische Gleichgewichtsmagnetisierung zu 98% in Transversalmagnetisierung zu überführen. Das Signal eines rechteckförmigen 90° Pulses, der die gleiche Mikrowellenleistung zur Verfügung hat, ist schon bei 25 MHz Offset um die Hälfte abgesunken. Diese eindrucksvolle Zunahme an Bandbreite wurde dann mittels flüssig

Phasen Fourier-Transform ESR an dem Radikal Phenalylen demonstriert, wo der OCT Puls auch off-resonant eingestrahlt das Spektrum mit richtigen Amplitudenverhältnissen wiedergab und der rechteckförmige Puls in dieser Beziehung völlig versagte. Bei der Arbeit mit pre-fokussierenden Pulsen, die als eine monolithische Hahn Echo Sequenz in einem OCT Puls gesehen werden können, tauchten sowohl Limitierungen durch Hardware als auch Artefakte verursacht durch anisotrope Kopplungen, die bei der Pulsoptimierung nicht berücksichtigt wurden, auf. Die linearen Verzerrungen der Pulsform durch die bandbreitenlimitierte Elektronik und den Mikrowellenresonator wurden erfasst und in die Pulsoptimierung miteinbezogen. Dazu wurde mit einer Sonde die B_1 Antwort auf eine pseudostochastische Sequenz gemessen, aus der die Impulsantwort des gesamten Anregungszweiges extrahiert werden konnte.

PELDOR Spektroskopie ermöglicht Abstände zwischen zwei oder mehr paramagnetischen Zentren, die zwischen 2 und 8 nm voneinander entfernt sind, zu bestimmen. Hierbei wird der sog. A-Spin mit einer Echo-Sequenz beobachtet und der zu ihm gekoppelte B-Spin mit einem zeitlich inkrementierten Mikrowellenpuls anderer Frequenz invertiert. Das Echo ist mit der Frequenz der dipolaren Kopplungsstärke moduliert, aus welcher direkt auf den Abstand geschlossen werden kann. Die Modulationstiefe ist direkt proportional zur Menge an B-spins die der Pump-Puls invertiert. Limitierend ist auch hier die Bandbreite und Inversionseffizienz des Pumpulses. In Kapitel 6.2 ist dargestellt, wie die Modulationstiefe und damit das Signal-zu-Rausch Verhältnis von PELDOR Experimenten durch den Einsatz speziell optimierter adiabatischer Inversionspulse verbessert werden kann. Für den Fall eines Biradikals mit einem Abstand von 3.4 nm zwischen den zwei Nitroxid-gruppen konnte die Modulationstiefe und damit das S/R-Verhältnis durch einen modifizierten sech/tanh Pump-Puls um einen Faktor größer 2 verbessert werden.

Der sech/tanh Pump-Puls wurde an einem anspruchsvolleren Modellsystem bestehend aus einem spektral sehr breiten Co^{2+} Spinsystem verbunden mit einem Nitroxidradikal über einen relativ kurzen Abstand von etwa 2.1 nm getestet. Um den tatsächlichen Zuwachs an Modulationstiefe zu testen wurde auf dem spektral breiten Cobalt gepumpt. Da ein adiabatischer Puls die B-Spins innerhalb seiner Bandbreite nicht gleichzeitig sondern nacheinander invertiert, ist eine Verschleifung des Nullpunktes über die Zeit, in der der Puls effektiv invertiert, die Folge. Die zeitliche Verschleifung bewirkt einen Tiefpass im Frequenzbereich der die Abstandsverteilungsfunktion verzerrt. Es wird jedoch gezeigt, dass die Dämpfung der dipolaren Oszillation bedingt durch die Verschleifung des Zeitnullpunktes

im Falle des adiabatischen Pulses durch einen zusätzlichen Pump-Puls refokussiert werden kann. Der zusätzliche Pump-Puls muss dazu eine dem 1. Pump-Puls entgegengesetzte Sweep-Rate haben und wurde zeitlich nicht inkrementiert. Mit dieser neuen breitbandigen 5-Puls PELDOR Sequenz konnte ein Zuwachs im S/R um einen Faktor größer 3 gegenüber der klassischen 4-Puls Sequenz erzielt werden.

Im letzten Teil der Arbeit (Kapitel 6.3) wird eine neue 7-Puls PELDOR Sequenz vorgestellt, die unter bestimmten Bedingungen eine erhebliche Vergrößerung des dipolaren Zeitfensters ermöglicht. Eine Vergrößerung des Zeitfensters erhöht nicht nur die Auflösung im Frequenz- und damit Abstandsbereich sondern ermöglicht auch eine wesentlich präzisere Auftrennung in inter- und intramolekulare Signale.

Ist Kernspindiffusion eine wesentliche Ursache der Dekohärenz auf dem beobachteten A-Spin, so ist es möglich, durch wiederholtes refokussieren (CPMG Sequenz) den Beobachtungszeitraum einer Kohärenz deutlich zu verlängern. In der 7-Puls Sequenz wird der A-Spin dreimal refokussiert, was drei Pump-Pulse erfordert. Die Anforderung an die Pump-Pulse ist, dass eine bestimmte B-Spin Fraktion mehrmals quantitativ invertiert wird. Rechteckförmige Pulse invertieren nur in Resonanz quantitativ und fallen dann bezüglich ihrer Inversionseffizienz sehr schnell ab und sind somit ungeeignet für multiple Inversionen. Adiabatische sech/tanh Pulse sind jedoch in der Lage, über einen festgelegten Bereich mit einer Effizienz von nahezu 1 zu invertieren und außerhalb dieses Bereiches keine Anregung durchzuführen. Die Kombination einer CPMG Beobachtungssequenz mit PELDOR Spektroskopie ist somit mit rechteckförmigen Pump-Pulsen nicht möglich.

Da auch sech/tanh Pump-Pulse eine in der Praxis durch B_1 Inhomogenitäten, Hardware-Imperfektionen und T_2 -Effekten reduzierte Inversionseffizienz zeigen, ist eine gewohnt einfache Umsetzung der Messdaten in eine Abstandsverteilung nicht möglich. Durch die reduzierte Inversionseffizienz ist das Zeitsignal aus $2^3=8$ dipolaren Pfaden mit unterschiedlichen Gewichten zusammengesetzt. Zur Korrektur wurde ein iterativer Weg beschritten der außer der Kenntnis der Inversionseffizienz keine zusätzlichen Messungen benötigt. Die nicht 7-Puls Signale werden aus der 7-Puls Messung konstruiert und dann mit ihrer Wahrscheinlichkeit gewichtet subtrahiert. Das Resultat ist eine verbesserte 7-Puls Entwicklung aus der wiederum die nicht-7 Puls Signale berechnet werden, um diese dann von dem Hintergrund-korrigierten Ursprungssignal abzuziehen. Es genügen meist wenige Iterationsschritte bis zur Konvergenz.

Mit der neuen 7-Puls PELDOR Sequenz gelang es zu zeigen, dass die Asymmetrien, welche der aus drei identischen Untereinheiten aufgebaute Betain Transporter BetP in 2 und 3-dimensionalen Kristallstrukturen zeigt, in gefrorenem Detergenz zunehmen.

4 Introduction

4.1 Motivation and aim

EPR spectroscopy is the most important method to explore paramagnetic substances. Paramagnetic centers are either naturally occurring or are artificially introduced by irradiation[1] or spin labeling techniques[2] and reveal valuable information of their magnetic surrounding which then allows to draw inferences on the structure. In contrast to NMR spectroscopy where pulsed methods superseded the cw-technique very soon, pulsed EPR spectroscopy remained exotic until the early eighties. The slow development of pulsed EPR methods was caused by the approximately three orders of magnitude faster timescale of EPR compared to NMR. As soon as pulsed EPR spectrometers became available methods like pulsed ENDOR, ESSEM spectroscopy and pulsed ELDOR came up which not only gave a deeper insight into the magnetic environment of radical centers but also enabled to study chemical dynamics on the ns-timescale[3] .

The strength of magnetic dipole-dipole interactions strongly depends on the inter-spin distance and their orientation. This information is in most cases buried in the inhomogeneous broadening of the EPR transition. Pulsed EPR spectroscopy however made it possible to measure dipolar couplings between unpaired electrons with other electrons or nuclei independent of the inhomogeneous line-width[4, 5]. With the ability to measure dipolar couplings between electrons separated by 2 -8 nm pulsed EPR techniques for distance determinations became the main branch of pulsed EPR spectroscopy and is nowadays a powerful tool for structural investigations in material science[6] , structural biology[7, 8] and chemistry[9, 10].

Since its very beginnings pulse EPR spectroscopy has struggled with technical hurdles originating from the huge inhomogeneous line broadening of most paramagnetic species in combination with very fast phase relaxation. The microwave pulses for excitation are produced by fast switches which generate a sinc-type excitation profile in the frequency domain. Rectangular shaped excitation pulses are regarded to work efficiently within a bandwidth $\Delta\nu$ which corresponds to the excitation field strength $B_1 = \mu_0 H_1$ times the gyromagnetic ratio γ .

$$\Delta\nu < \gamma \cdot B_1$$

Outside this range strong artifacts are introduced by amplitude and phase errors in the off-resonant magnetization. Typical B_1 fields created by X (10 GHz) - and Q (34 GHz) -band spectrometers are in the range of 10 G. The spectral width of a nitroxide spin-system covers already more than 60 G at these frequencies. The situation becomes worse for paramagnetic transition metals often covering a bandwidth of several GHz. NMR spectroscopy is not as affected by bandwidth problems like EPR but the unselectivity and poor efficiency of rectangular shaped rf-pulses caused a rapid growth in alternative excitation pulses providing better selectiveness and efficiency[11]. At first instance Fourier arguments which are valid for small flip-angles have been used to derive Gaussian, sinc, or other type of rf-pulses. In recent years optimum control theory gathered widespread interest in the field of NMR due to its success in optimizing pulses or pulse sequences with a huge parameter space in moderate time. Almost arbitrary excitation patterns[12] have been generated. The question of optimized coherence transfer[13] has been addressed as well as the design of cooperative pulses[14]. Completely new broadband excitation schemes have been developed (bebop-pulses) which create transverse magnetization with an arbitrary or even linear phase slope[15] over a certain bandwidth which could never be addressed by rectangular pulses of the same incident B_1 field-strength. Broadband inversion of magnetization is not as critical as excitation and is covered by the adiabatic pulse family[16]. These however fail to refocus transverse magnetization since they perform point to point rotations instead of universal rotations needed for refocusing[17].

A pulse-shaper suitable for EPR spectroscopy should have a bandwidth comparable to the spectral width of the spin systems. To address off-resonant spins within a few hundreds of MHz a time resolution in the ns-regime is needed. Since AWG's (arbitrary waveform generators) which work on an ns time resolution have been available since recent years shaped pulses were not applied in EPR spectroscopy.

In this work an AWG with a 1 ns time resolution has been implemented into a BRUKER ELEXSYS E580 pulsed EPR spectrometer and for the first time shaped microwave pulses have been successfully applied in EPR at X-and Q-band frequencies.

4.2 Spin physics

The following chapter resembles the important aspects of theory about magnetic resonance needed to prepare the work at hand.

4.2.1 Bloch picture and rotating frame

In the Bloch picture the electron spin behaves like a classical rotating charge. The magnetic moment $\vec{\mu}$ which arises is connected with the quantum mechanical angular momentum \vec{I} through the gyromagnetic ratio γ . The treatment is classical even though the angular momentum is a quantum mechanical feature.

$$\vec{\mu} = \gamma \cdot \vec{I} \quad (1)$$

If a magnetic field \vec{H} is present with a component perpendicular to $\vec{\mu}$ a torque \vec{M} is exerted on the magnetic moment $\vec{\mu}$.

$$\vec{M} = \vec{\mu} \times \vec{H} \quad (2)$$

The torque \vec{M} is the rate of change of the angular momentum \vec{I} , and therefore the time derivative of $\vec{\mu}$ is given by:

$$\dot{\vec{\mu}} = \gamma \vec{\mu} \times \vec{H} \quad (3)$$

Equation (3) states that the magnetic moment $\vec{\mu}$ is moving perpendicular to the magnetic field, which means that without damping the two would never align. $\vec{\mu}$ precesses around \vec{H} . The frequency of this movement is the Larmor frequency ν_L given by :

$$\nu_L = \gamma H \quad (4)$$

Experiments are described in a frame rotating with the operating frequency of the spectrometer. This, as it is shown later removes the fast precession originating from the roughly three orders of magnitudes stronger static magnetic field \vec{H}_0 compared to the excitation field \vec{H}_1 .

The magnetic moment seen in a frame with coordinates $\vec{i}, \vec{j}, \vec{k}$ rotating about an axis $\vec{\Omega}$ is given by:

$$\vec{\mu}_{\text{rot}} = \vec{i}\mu_{x_{\text{lab}}} + \vec{j}\mu_{y_{\text{lab}}} + \vec{k}\mu_{z_{\text{lab}}} \quad (5).$$

Where the orthogonal unit vectors in the laboratory frame are $\vec{i}, \vec{j}, \vec{k}$ and $|\vec{\Omega}|$ is the rotation in radians. The time derivative of $\vec{\mu}$ in the rotating frame is given by :

$$\dot{\vec{\mu}}_{\text{rot}} = \vec{i}\dot{\mu}_i + \vec{j}\dot{\mu}_j + \vec{k}\dot{\mu}_k \quad (6).$$

The derivative of $\vec{\mu}$ in the laboratory frame is the sum of the derivative in the rotating frame and the rate induced by the rotation.

$$\dot{\vec{\mu}}_{\text{lab}} = \dot{\vec{\mu}}_{\text{rot}} + \vec{\Omega} \times \vec{\mu}_{\text{lab}} \quad (7)$$

If one combines Equation (3) and (7):

$$\dot{\vec{\mu}}_{\text{rot}} = \vec{\mu}_{\text{lab}} \times (\vec{\Omega} + \gamma\vec{H}) \quad (8)$$

Equation (8) shows that if one chooses $\vec{\Omega} + \gamma\vec{H} = \mathbf{0}$, $\vec{\mu}$ is stationary in the rotating frame. An oscillating field $\vec{H}_1 = (H_1 \cos(\omega t + \varphi), 0, 0)$ applied to manipulate $\vec{\mu}$. The field has to be perpendicular to \vec{H}_0 .

$$\dot{\vec{\mu}}_{\text{rot}} = \vec{\mu}_{\text{lab}} \times (\vec{\Omega} + \gamma(\vec{H}_0 + \vec{H}_1)) \quad (9)$$

The field \vec{H}_1 which is oscillating in the x,y-plane if $\vec{H}_0 \parallel z$ in the laboratory frame can be split up in two counter rotating components:

$$\vec{H}_1 = (0.5H_1 \cos(\omega t + \varphi), 0.5H_1 \sin(\omega t + \varphi), 0) + (0.5H_1 \cos(\omega t + \varphi), -0.5H_1 \sin(\omega t + \varphi), 0) \quad (10)$$

If a frame is chosen such that it rotates with a frequency $\omega/2\pi$, one component is fixed in that frame whereas the other rotates with $2\omega/2\pi$ which can be neglected since it does not affect $\vec{\mu}$. If also $\gamma\vec{H}_0 = -\vec{\Omega}$, which means the spectrometer frequency matches the Larmor frequency of the spin, resonance occurs. The effective field which is experienced by the spin in the rotating frame is perpendicular to the thermal equilibrium magnetization. The

spin precesses around $\vec{H}_{1_{\text{rot}}}$ with a frequency $\frac{1}{2}\gamma\vec{H}_1$. Thus, no matter how small the microwave field is compared to the static field the magnetization will rotate away from its thermal equilibrium. If $\gamma\vec{H}_0 \neq -\vec{\Omega}$, a component $\vec{H}_{0_{\text{rot}}} = \vec{H}_0 - \frac{\vec{\Omega}}{\gamma}$ along z remains and the total effective field is the vector sum of these fields:

$$\vec{H}_{\text{eff}} = (0,0,H - \Omega/\gamma) + (\cos(\varphi)H_1/2, \sin(\varphi)H_1/2,0) \quad (11)$$

The excitation and the detection of transverse magnetization is accomplished by the same device. This device, a microwave resonator, can be thought as an impedance matching device between the waveguide and the generator which is the precessing magnetic moment of the sample. For excitation microwave is applied and the resonator generates the excitation field which oscillates perpendicular to the static magnetic field \vec{H}_0 and turns the magnetization vector in the rotating frame with the nutation frequency $\omega_{\text{nut}} = \sqrt{\gamma|\vec{H}_0| - |\vec{\Omega}| + \gamma|\vec{H}_1|}$. If the microwave irradiation is stopped and the transverse components of the magnetic moment are nonzero these will precess with their Larmor frequency in the laboratory frame. The transverse component of $\vec{\mu}$ generates circular polarized microwave which is coupled to the resonance mode of the resonator which couples to the waveguide. In all commercial spectrometers only one component of the circular polarized signal can be detected since the resonance structure can only detect along one polarization axis. The circular polarized nature of the emitted microwave is used in high field EPR where quasi optical devices are used. Linear polarized microwave is used for excitation which enables to detect on the orthogonal polarization since the sample-emitted microwave is circular polarized[18, 19].

The detection of transverse magnetization also occurs in the rotating frame. This is accomplished by mixing the emitted microwave with the spectrometer frequency and subsequent low pass filtering. This is done with two orthogonal phases which generates a complex signal which enables to distinguish positive and negative frequency offsets between spectrometer frequency and Larmor frequency in the rotating frame.

4.2.2 Spin Hamiltonian

The trajectory of a magnetic moment in a time dependent magnetic field as described in 4.1.1 shows the time average of a single spin or an ensemble average of multiple spins which are not coupled. It does not describe the motion of a single spin or coupled spins since these are quantum mechanical objects which have to be treated in the formalism of quantum mechanics. The spin of an electron couples to static and time-dependent external magnetic fields, to other magnetic moments like nuclei which bear a magnetic moment, to other electrons or to its own orbital angular momentum. The expression “spin Hamiltonian” is chosen because only the spin is contained in the operator while all other dimensions which depend upon spatial coordinates are summed up in empirical constants or second rank tensors if anisotropy is present.

The Hamiltonian of a spin \vec{S} in a static magnetic field \vec{B}_0 , which is called the Zeeman interaction is:

$$\hat{H}_Z = \gamma \vec{B}_0 \underline{\underline{g}} \hat{S} \quad (12)$$

With the total spin operator $\hat{S} = \frac{\hbar}{2} \begin{pmatrix} \sigma_x \\ \sigma_y \\ \sigma_z \end{pmatrix}$ and σ_i being the Pauli matrices. The matrix $\underline{\underline{g}}$

describes the anisotropy of the Zeeman interaction. This interaction is caused by orbital angular momentum which couples to the electron spin. Since $\underline{\underline{g}}$ is a symmetric 3x3 matrix it can always be diagonalized by a rotation of the coordinate system. For radicals in solution or solids the orbital angular momentum is quenched if no external field is applied. Orbital angular momentum can only exist if degenerate states are present. Non degenerate states can always be chosen such that the wave function is real and, since the angular momentum operator is complex the expectation value for pure real states has to be zero. The crystal field present in liquids and solids destroys the degeneracy and causes the wavefunction to be real, thus eliminating all orbital angular momentum. If an external magnetic field is applied, the non-degenerate states mix which generates a small amount of orbital angular momentum which increases or decreases the external field acting on the electron spin. The amount of orbital angular momentum generated is proportional to the strength of the applied field causing the anisotropy of the Zeeman interaction to scale with the applied field.

The coupling of the electron spin to other magnetic nuclei, the hyperfine interaction is covered by:

$$\hat{H}_{\text{HF}} = \hat{S} \underline{\underline{\hat{A}}} \quad (13)$$

The hyperfine coupling tensor $\underline{\underline{\hat{A}}}$ contains the isotropic and anisotropic interaction. The anisotropic part originates from dipole-dipole interaction between the electron spin and the nuclear spin. The anisotropy is caused by a non-spherical distribution of the electron density around the nucleus. The isotropic part describes the dipolar coupling between the electron spin and nuclear spin inside the nucleus and is only seen if the wave function of the unpaired electron possesses s-orbital contributions because only these bear a non-zero probability density in the nucleus.

The interaction between two unpaired electrons has two contributions: \hat{H}_{Dip} which describes the classical dipolar coupling between two or more electron spins whereas \hat{H}_{Ex} has a pure quantum mechanical origin and is a non-magnetic interaction. Exchange coupling is present if the orbitals of the unpaired electrons overlap. The overlap creates a molecular orbital for which the Pauli principle holds which states that the total wavefunction of the electron has to change sign upon coordinate exchange. The consequence is a change in spatial electron distribution if the spin state of an electron is changed which of course changes the energy of the system.

The exchange coupling is written as:

$$\hat{H}_{\text{Ex}} = J \hat{S}_A \hat{S}_B \quad (14);$$

the exchange coupling constant J has no orientation dependence.

The dipolar interaction between two electrons is derived from the classical expression of one point dipole $\vec{\mu}_A$ in the field of another point dipole $\vec{\mu}_B$ with an inter-point vector \vec{r} :

$$E_{\text{dip}} = \frac{\mu_0}{4\pi} \left(\frac{\vec{\mu}_A \vec{\mu}_B}{r^3} - \frac{3(\vec{\mu}_A \vec{r})(\vec{\mu}_B \vec{r})}{r^5} \right) \quad (15)$$

Substituting the magnetic dipole moments $\vec{\mu}$ with the corresponding operator $\gamma \hat{S}$, the quantum-mechanical counterpart is obtained:

$$\hat{H}_{\text{dip}} = \frac{\mu_0 \mathbf{g}_A \mathbf{g}_B \gamma_A \gamma_B}{4\pi} \left(\frac{\hat{\mathbf{S}}_A \hat{\mathbf{S}}_B}{r^3} - \frac{3(\hat{\mathbf{S}}_A \vec{r})(\hat{\mathbf{S}}_B \vec{r})}{r^5} \right) \quad (16)$$

For further discussion it is useful to express the interspin vector \vec{r} in spherical coordinates

$$\vec{r} = \begin{pmatrix} r \sin \mathcal{G} \cos \varphi \\ r \sin \mathcal{G} \sin \varphi \\ r \cos \mathcal{G} \end{pmatrix} \quad (17)$$

This yields the following operator for the dipole-dipole interaction:

$$\hat{H}_{\text{dip}} = \frac{\mu_0 \mathbf{g}_A \mathbf{g}_B \gamma_A \gamma_B}{4\pi r^3} (\mathbf{A} + \mathbf{B} + \mathbf{C} + \mathbf{D} + \mathbf{E} + \mathbf{F}) \quad (18).$$

With:

$$\begin{aligned} \mathbf{A} &= \hat{S}_{zA} \hat{S}_{zB} (3 \cos^2 \theta - 1) \\ \mathbf{B} &= -1/4 (\hat{S}_{+A} \hat{S}_{-B} + \hat{S}_{-A} \hat{S}_{+B}) (3 \cos^2 \theta - 1) \\ \mathbf{C} &= 3/2 (\hat{S}_{+A} \hat{S}_{zB} + \hat{S}_{zA} \hat{S}_{+B}) \sin \theta \cos \theta e^{i\varphi} \\ \mathbf{D} &= 3/2 (\hat{S}_{-A} \hat{S}_{zB} + \hat{S}_{zA} \hat{S}_{-B}) \sin \theta \cos \theta e^{i\varphi} \\ \mathbf{E} &= 3/4 \hat{S}_{+A} \hat{S}_{+B} \sin^2 \theta e^{-2i\varphi} \\ \mathbf{F} &= 3/4 \hat{S}_{-A} \hat{S}_{-B} \sin^2 \theta e^{-2i\varphi} \end{aligned} \quad (19)$$

The shift operators $\hat{S}_+ = \hat{S}_x + i\hat{S}_y$ and $\hat{S}_- = \hat{S}_x - i\hat{S}_y$ are useful to decide whether a term is nonsecular under certain conditions and can therefore be neglected. PELDOR (pulsed electron double resonance) experiments require in most cases only the A- term of the dipolar alphabet as is explained in the following. The Zeeman basis $|\alpha\alpha\rangle |\alpha\beta\rangle |\beta\alpha\rangle |\beta\beta\rangle$ is assumed which means that the quantization axis is parallel to \vec{B}_0 and the Zeeman basis states do not mix. **A** has only non-zero matrix elements between equal states. **B** connects states $|\alpha\beta\rangle$ and $|\beta\alpha\rangle$ producing off-diagonal elements in the H-matrix, but have only to be taken into account if the matrix element $\frac{\mu_0 \mathbf{g}_A \mathbf{g}_B \gamma_A \gamma_B}{4\pi} \langle \beta\alpha | \mathbf{B} | \alpha\beta \rangle$ is comparable or larger than the difference in Zeeman energy of the states, which in most cases is not fulfilled. The terms **C**, **D** connect states which differ in the range of one Zeeman interaction and can therefore be neglected. The same holds for **E**, **F** which connect states $|\alpha\alpha\rangle$ and $|\beta\beta\rangle$ which differ by two electron Zeeman energies.

4.2.3 Density matrix

The density matrix formalism covers the statistical nature of experiments on many quantum objects simultaneously or on single quantum objects connected to a thermal bath. The typical EPR experiment is performed on a large number N of spins which is approximately 10^{22} . The wave function of such a system for $S=1/2$ particles would span a 2^N -dimensional Hilbert space which cannot be treated by any means.

A system may be described by an incoherent superposition of smaller subsystems with a reduced dimensionality. An example might be a nitroxide radical where an electron with spin $S=1/2$ is coupled to a nucleus with spin $I=1$ which spans a Hilbert space of dimensionality $k=6$. The complete wave function of a system containing N nitroxide radicals would have a dimensionality 6^N . If the couplings between the nitroxide radicals are small compared to the couplings within one nitroxide and to the external field one can define the nitroxide as the smallest subsystem. All the subsystems are in pure states with a wavefunction $\psi = \sum_i c_i \varphi_i$

with orthonormal basis functions φ_i and occur with a probability p_i . The outcome of a measurement of an observable Ω which is represented by the operator $\hat{\Omega}$ is then given by an average over all subensembles:

$$\langle \hat{\Omega} \rangle = \sum_{i=1}^n p_i \langle \psi_i | \hat{\Omega} | \psi_i \rangle = \sum_{i=1}^n p_i \sum_{p,j} c_p^* c_k \langle \varphi_p | \hat{\Omega} | \varphi_j \rangle = \sum_{p,j} \overline{c_p^* c_k} \langle \varphi_p | \hat{\Omega} | \varphi_j \rangle \quad (20)$$

The matrix elements $\langle \varphi_p | \hat{\Omega} | \varphi_j \rangle$ do not change during an experiment but the average over the expansion coefficients $\overline{c_p^* c_k}$ changes in time. These coefficients span a matrix, the density matrix.

$$\sigma = \sum_{i=1}^n p_i |\psi_i\rangle \langle \psi_i| = \sum_{i=1}^n p_i \sum_{p,j=1}^n c_{pi}^* c_{ji} |\varphi_j\rangle \langle \varphi_p| = \sum_{p,j=1}^n \overline{c_p^* c_j} |\varphi_j\rangle \langle \varphi_p| \quad (21)$$

The density matrix of an ensemble must not contain all information about a system but everything which is experimentally accessible. If $\sum_{i=1}^n c_i^2 = 1$, the density matrix describes a

pure state which can alternatively be written as a wave function. If $\sum_{i=1}^n c_i^2 < 1$, the system is in

a mixed state, an incoherent superposition of subensembles in pure states, which is the typical

situation for magnetic resonance experiments. A mixed state can not be written as a wave function.

If one substitutes $\langle \varphi_i | \sigma | \varphi_j \rangle = \overline{c_i c_j^*}$ in Equation (20):

$$\langle \hat{\Omega} \rangle = \sum_{p,j} c_p^* c_k \overline{\langle \varphi_p | \hat{\Omega} | \varphi_j \rangle} = \sum_{p,j} \langle \varphi_j | \sigma | \varphi_p \rangle \langle \varphi_p | \hat{\Omega} | \varphi_j \rangle = \sum_j \langle \varphi_j | \sigma \hat{\Omega} | \varphi_j \rangle = \text{tr}(\sigma \hat{\Omega})$$

Thus any expectation value is calculated independent of the basis by calculating the trace of the product of the density matrix with the operator.

4.2.4 Time evolution of the density matrix

The density matrix which contains all measurable information has to be used to describe experiments on stochastic mixtures of spins. The propagation of the density matrix in time can be derived using the Schrödinger equation:

$$\frac{d}{dt} \psi = -\frac{i}{\hbar} \hat{H} \psi \quad (22)$$

The propagation in time is a unitary transformation of the wavefunction which allows to define a propagator U

$$\psi(t) = U \psi(0) \quad (23)$$

Substituting equation (23) into equation (22) gives:

$$\frac{d}{dt} U \psi(0) = -\frac{i}{\hbar} \hat{H} U \psi(0) \quad (24)$$

Solving equation (24) gives the propagator :

$$U(t) = e^{-i/\hbar \hat{H} t} \quad (25)$$

The density operator is:

$$\sigma(t) = |\psi(t)\rangle \langle \psi(t)| \quad (26)$$

With $|\psi(t)\rangle = U |\psi(0)\rangle$

The time evolution of the density operator can then be written as:

$$\sigma(t) = U |\psi(0)\rangle\langle\psi(0)| U^* = e^{-i/\hbar\hat{H}t} |\psi(0)\rangle\langle\psi(0)| e^{i/\hbar\hat{H}t} = U \sigma(0) U^* \quad (27)$$

\hat{H} is assumed to be time independent. If this is not the case the propagator can not be written as in equation (27). For simulations \hat{H} is in general time dependent which can be treated numerically. The evolution of the density matrix is then split into several propagators which on their own can be regarded as time independent.

$$\sigma(t) = U_1 \dots U_2 U_1 \sigma(0) U_1^* U_2^* \dots U_t^* \quad (28)$$

4.3 Adiabatic pulses

4.3.1 The principle of adiabaticity

In general one speaks of adiabaticity if a property does not change significantly with respect to another while a system changes its state. Adiabaticity in thermodynamics i.e. is fulfilled if the heat exchange of a system with its environment during a process is so slow that it can be neglected.

In magnetic resonance the term adiabaticity is used for a special family of pulses mostly used for inversion purposes. The spin trajectories are described in a frame rotating with the instantaneous frequency of the pulse in contrast to the common rotating frame. This frame is called the frequency frame. If the magnetization is in thermal equilibrium along the static magnetic field, \vec{B}_0 which coincides with the z-axis in the laboratory frame, an adiabatic pulse or passage inverts the magnetization so that it points along the -z-axis after the pulse.

If the effective field has a small angular deviation from the z-axis at the beginning of the pulse, which is fulfilled for small \vec{B}_1 -amplitudes and/or significant frequency offsets, the magnetization will also precess with a small angle around the effective field. If now the angle between the z-axis and the effective field is increased slowly enough, whether by increasing the \vec{B}_1 -amplitude or/and by decreasing the frequency offset, the magnetization will continue

to precess around \vec{B}_{eff} and hence follow \vec{B}_{eff} . If the frequency offset decreases further and changes sign the effective field will end up along the -z-axis and so will the spins which followed the effective field.

The principle of adiabaticity is explained on an example of a constant-adiabaticity pulse (CAP) which has the following amplitude $B_1(t)$ and frequency modulation $\Delta\nu(t)$ functions[20]:

$$B_1(t) = B_{1\text{max}} \cos(\pi t/T). \quad (29)$$

$$\Delta\nu(t) = \gamma B_{1\text{max}} \sin(\pi t/T) \quad (30).$$

With $t \in [-T/2, T/2]$, T being the pulse duration. $\Delta\nu(t)$ is the time dependent offset frequency.

The adiabaticity parameter Q is the ratio of the Larmor frequency around the effective field and the time derivative of the angle between the effective field vector and the z-axis which is $\dot{\theta}$. This parameter is in general, but not necessary, time dependent.

$$Q = \frac{\gamma |\vec{B}_{\text{eff}}|}{\dot{\theta}} \quad (31)$$

Adiabaticity in the frequency frame is usually accomplished if $Q = \frac{\gamma |\vec{B}_{\text{eff}}|}{\dot{\theta}} \gg 1$. For the

CAP pulse $Q = \frac{\gamma B_{1\text{max}} T}{\pi}$ which is time independent. Figure 1 shows a CAP pulse calculated with a maximum excitation field of 25 MHz and a duration of 2000 ns. According to equations 29 and 30 the bandwidth of inversion is approximately 50 MHz which is small compared to other adiabatic pulse schemes. Figure 2 shows the trajectory of the on-resonant spin in the rotating frame. The principle of adiabatic tracking cannot be recognized in this picture. The principle of adiabatic tracking is recognized in Figure 3 which shows the trajectory of the on-resonant spin in the frequency frame. The trajectories have been calculated from the Bloch equations.

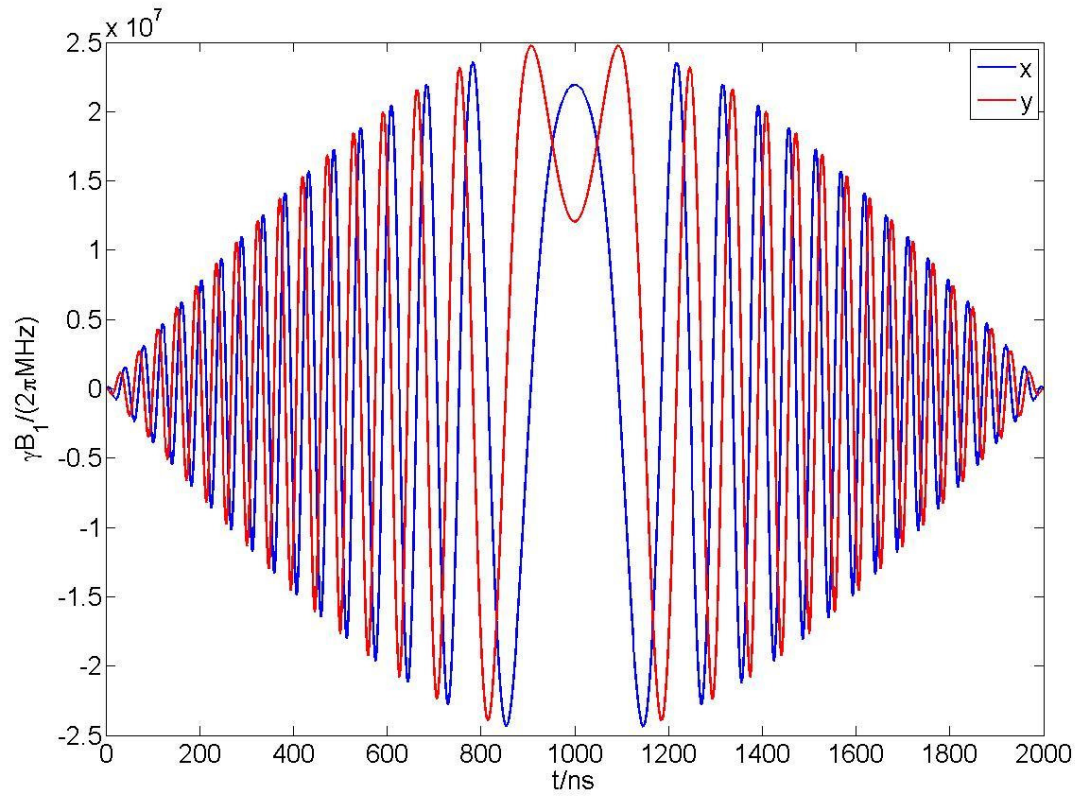


Figure 1 Shape of a CAP pulse according to Equations 29 and 30 utilizing an excitation field of 25 MHz and a duration of 2000 ns.

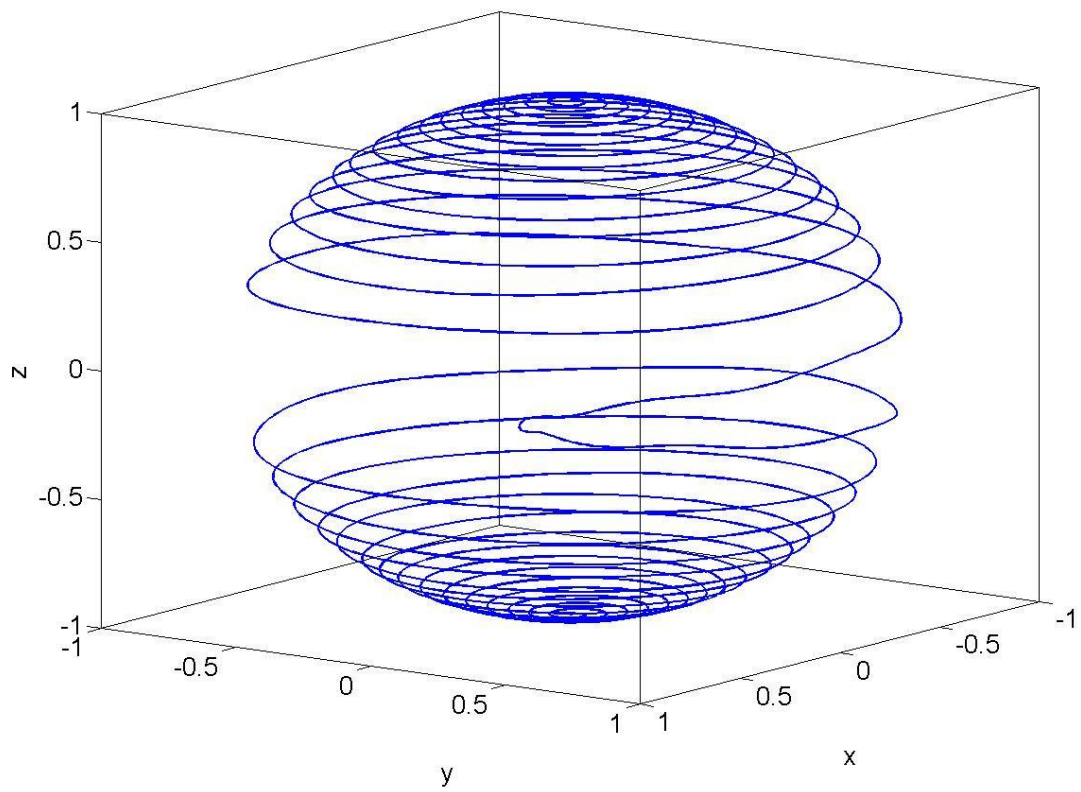


Figure 2 Trajectory of an on resonant spin in the rotating frame during the CAP pulse shown in Figure 1.

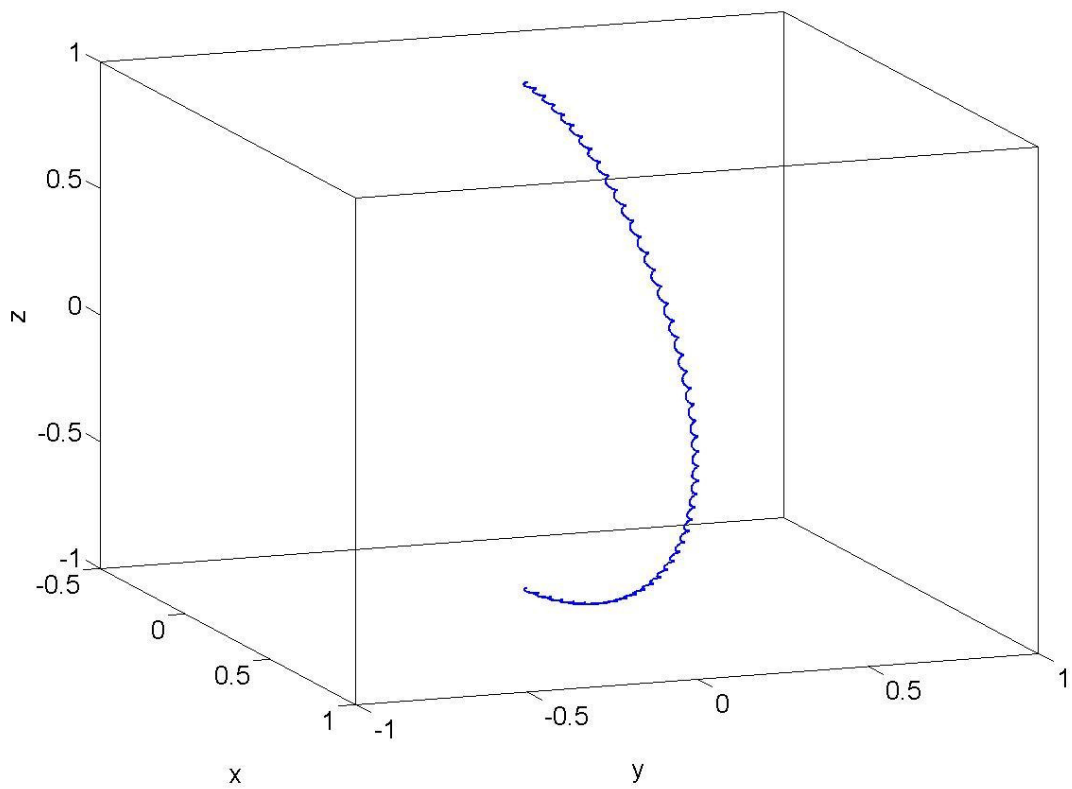


Figure 3 Trajectory of an on resonant spin with the CAP pulse shown in Figure 1 in the frequency frame.

Adiabatic pulses are described in terms of amplitude and frequency modulation functions. The actual pulse-shapes given as amplitude modulation functions for the x-and y- channel have been calculated as described in the following:

The instantaneous frequency is given by the frequency modulation function $\Delta\omega(t)$. The instantaneous frequency is the time derivative of the phase argument. Therefore the amplitude envelope function $y(t)$ is the cosine of the integral of $\Delta\omega(t)$:

$$y(t) = \cos\left(\int_0^t \Delta\omega(t)dt\right) \quad (32)$$

The carrier frequency $s(t) = \cos(\omega_0 t)$ which is the actual frequency of the spectrometer is modulated with $y(t)$. The so created image frequency makes it necessary to add a second signal

$$x(t) = \sin\left(\int_0^t \Delta\omega(t)dt\right) \quad (33)$$

which modulates the 90° phase shifted carrier. The output signal for the x- and y channel for a given frequency modulation $\Delta\omega(t)$ and amplitude modulation $B_1(t)$ is then calculated by:

$$x(t) = B_1(t) * \sin\left(\int_0^t \Delta\omega(t)dt\right) \quad (34)$$

$$y(t) = B_1(t) * \cos\left(\int_0^t \Delta\omega(t)dt\right) \quad (35)$$

4.3.2 The sech/tanh pulse

The sech/tanh pulse is an adiabatic inversion pulse which is unique among the family of adiabatic pulses due to its robust broadband response and frequency selectivity. These properties seemed ideal for EPR applications like PELDOR spectroscopy with single to multiple inversions. The modulation functions are given by[21]:

$$\Delta\omega(t) = BW * \tanh(\beta t) \quad (36)$$

$$B_1(t) = B_{1\max} \cdot \operatorname{sech}(\beta t) \quad (37)$$

The parameter BW determines the inversion bandwidth of the pulse which is twice the value of BW since $-1 < \tanh(x) < 1$. The parameter β is a measure of how fast the pulse sweeps and is typically chosen such that $\beta = 10.6/T$ which ensures a cutoff at 1% of its peak amplitude. T is the duration of the pulse with $t \in [-T/2, T/2]$.

The shape of a sech/tanh inversion pulse is shown in Figure 4 with typical pulse parameters given in the figure caption.

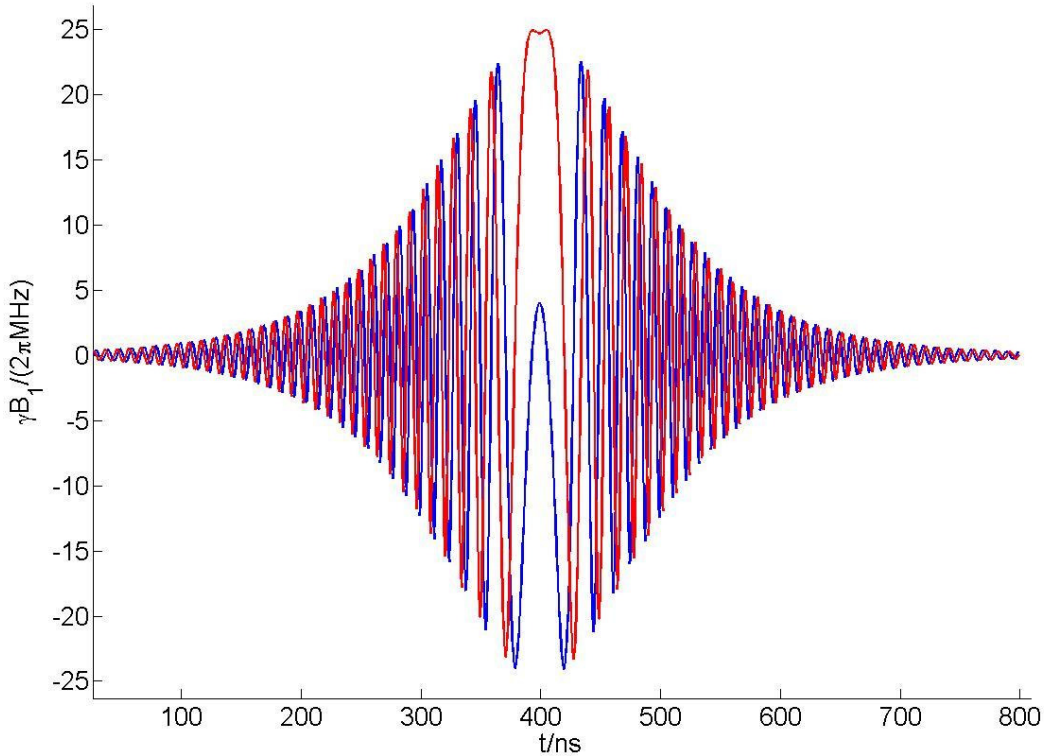


Figure 4 sech/tanh inversion pulse with $\beta = 10.6/T$; $T=800\text{ns}$, $B_{1\max}=25\text{ MHz}$ and $BW=100\text{ MHz}$.

In [20] the question is addressed whether the sech/tanh pulse is truly adiabatic or not. The sech/tanh pulse is, if a certain level of power is applied, almost independent of the excitation field strength which speaks for adiabatic behavior. The pulse shown in Figure 4 has at its center an adiabaticity parameter of $Q=0.47$ which is by no means adiabatic according to the definitions made in equation (30). It is shown that adiabatic tracking is accomplished in a frame where the z -axis follows the effective field in the frequency frame. This frame is called SORF (second order rotating frame) and since it is accelerated, an additional effective field

has to be taken into account. The magnetization follows the sum of these effective fields in the SORF .

The inversion profile of the pulse shown in Figure 4 is depicted in Figure 5. The remarkable property of the sech/tanh pulse is its robust wideband response combined with a very sharp transition region between pass-band and stop-band. This makes these pulses exceptionally suitable for EPR applications for single and multiple inversions of the spin system, especially if the spectral width of the spin system is larger than the inversion bandwidth.

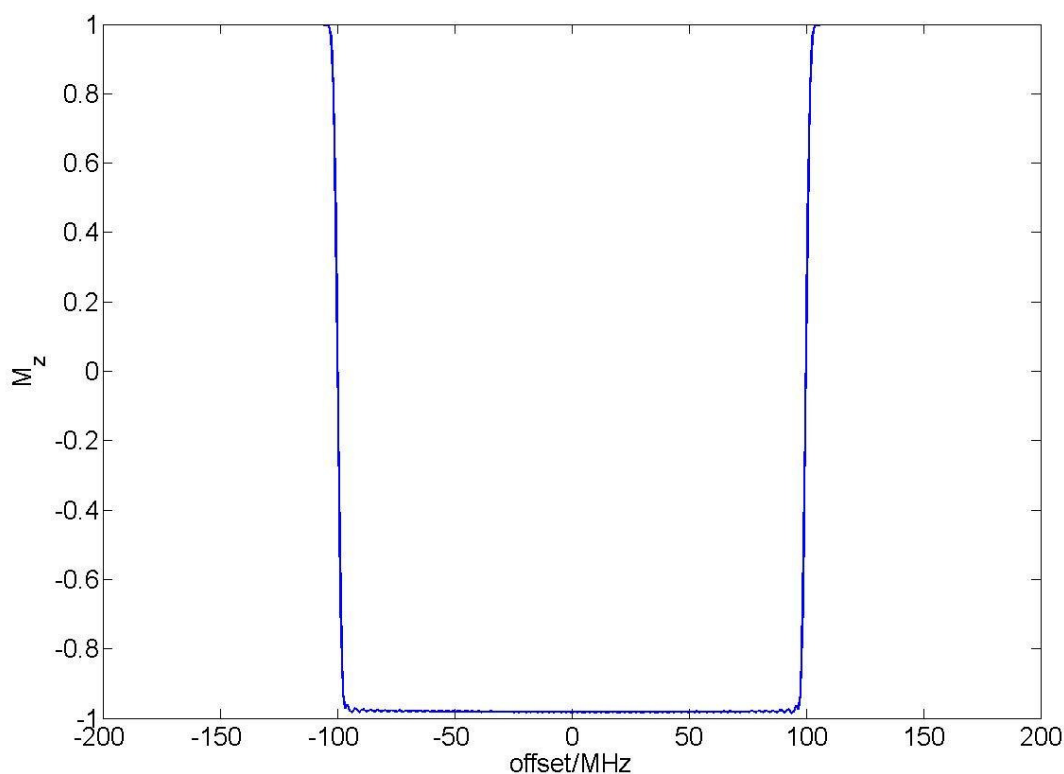


Figure 5 inversion profile of the sech/tanh pulse shown in Figure 4.

4.3.4 The WURST pulse

The WURST (wideband uniform rate smooth truncation) pulse introduced in Ref. [22] is interesting for a different purpose. If the experiment asks for a pulse which under a given maximum \mathbf{B}_1 field strength and pulse duration has the highest inversion bandwidth the WURST pulse is the optimal choice. The disadvantage compared to the sech/tanh pulse is its broader transition region between pass and stop-band. The modulation functions are given by:

$$\Delta\omega(t) = kt \quad (38)$$

$$B_1(t) = B_{1\max} * \left(1 - |\sin(\beta t)|^n\right) \quad (39).$$

The sweep rate k determines the sweep velocity. A too large sweep rate under a given maximum microwave field causes the pulse to leave the adiabatic region which sets the upper limit in bandwidth. The time variable is $t \in [-T/2, T/2]$ with T being the duration of the

pulse and $\beta = \frac{\pi}{2T}$ which causes the amplitude to be zero at the beginning and at the end of the

passage. The parameter n determines how fast the amplitude drops at the beginning and end of the pulse. The pulse performance itself is not affected too much upon variation of n . Best performance has been observed for $n=20-80$. The pulse shown in Figure 6 was calculated using a maximum excitation field of 25 MHz and a sweep rate of $k= 0.7$ MHz /ns, $n=80$ and a duration of 800 ns. This pulse is compared to a sech/tanh pulse calculated for the same experimental limitations which are maximum Power and pulse duration. The sech/tanh pulse was truncated more than usual with $\beta = 7.6/800$ to achieve a higher inversion bandwidth at the cost of some residual ripple on the pass-band. Even though the WURST pulse shows a significantly higher bandwidth of >400 MHz compared to 250 MHz (see Figure 7) for the sech/tanh pulse it does not need a larger duration or more power. The reason for the superior broadband response of the WURST pulse is recognized when comparing Figure 6 with the sech/tanh pulse shown in Figure 8. The WURST pulse utilizes the peak power almost throughout its whole duration delivering thus much more energy to the sample compared to the sech/tanh pulse which uses only in the center section the maximum power. Nonetheless is the sech/tanh pulse the most important pulse in this work due to its higher selectivity.

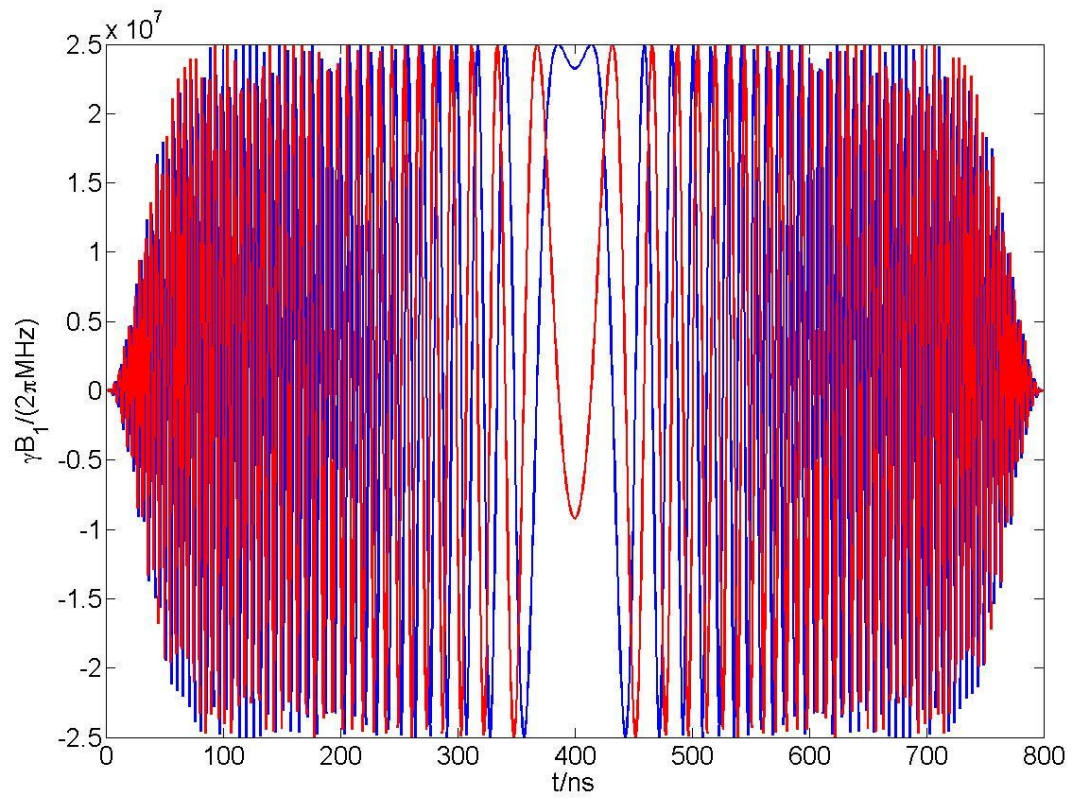


Figure 6 WURST pulse with $k=0.7$ MHz/ns, $B_{1\text{max}}=25$ MHz, $n=80$.

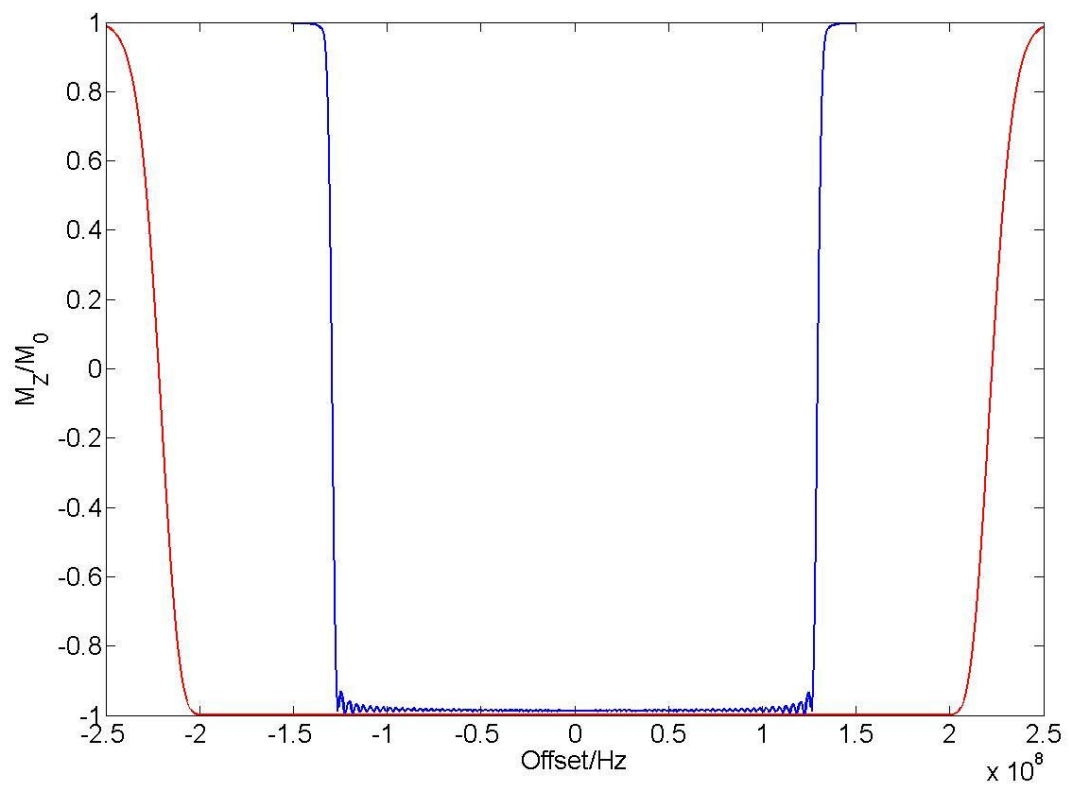


Figure 7 Inversion bandwidth comparison of a sech/tanh inversion pulse(blue) with a WURST pulse utilizing the same power and duration.

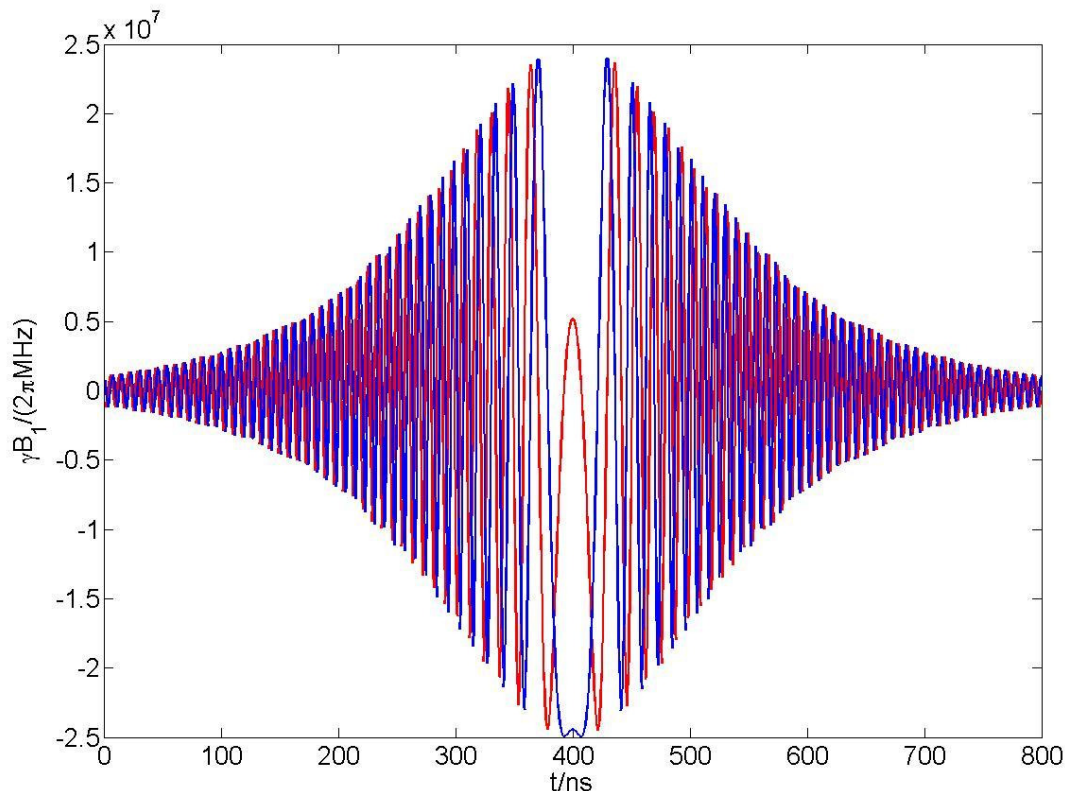


Figure 8 Sech/tanh inversion pulse used for the comparison shown in Figure 7. The pulse is slightly truncated to increase bandwidth and efficiency.

4.4 PELDOR

PELDOR which stands for pulsed electron electron double resonance or DEER (double electron electron resonance) is the currently most applied method in pulsed EPR for various subjects which all deal with distance measurements in the nm range. In contrast to cw-EPR, pulsed EPR is capable to determine couplings between an unpaired electron and other spin-bearing centers like nuclei or other unpaired electrons which are much smaller than the inhomogeneous line-width of the spin system involved.

4.4.1 The PELDOR signal

PELDOR is applied to measure distance distributions between two or more paramagnetic centers which are separated by 2-8nm. The requirement to do PELDOR measurements is the presence of paramagnetic centers which are dipolar coupled and are separated in their resonance frequencies. The separation has to be large enough to address them separately with pulses of different microwave frequencies (see Figure 9). If the difference of their resonance

frequencies is also much larger than the dipolar splitting which the dipolar Hamiltonian reduces to:

$$\hat{H}_{\text{dip}} = \frac{\mu_0 g_A g_B \gamma_A \gamma_B}{4\pi r^3} (\hat{S}_{zA} \hat{S}_{zB} (3 \cos^2 \theta - 1)) \quad (40)$$

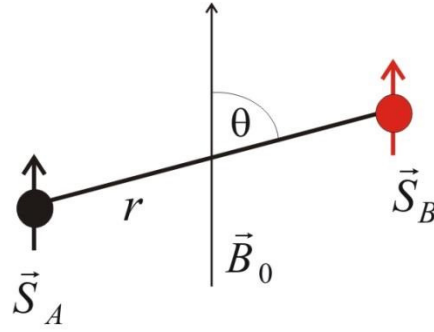


Figure 9 dipolar coupled spin pair for PELDOR spectroscopy. θ is the angle between the static magnetic field \vec{B}_0 and the interspin vector r .

The simplest pulse sequence for PELDOR is a two pulse Hahn Echo with fixed delay time τ between the $\frac{\pi}{2}$ and π pulses and a pump pulse on a different frequency which position is incremented in the first τ -period. This sequence is shown in Figure 10. To record the time zero of the dipolar evolution the pump pulse and the $\pi/2$ have to be applied simultaneously which is not possible with normal setups utilizing only one amplifier. This limitation was overcome with the invention of the dead-time free four-pulse PELDOR[23].

The pulses which build the echo act on the A-spin whereas the pump pulse acts on the B-spin. The echo is then recorded with respect to the time accumulated by the pump-pulse. The pump pulse flips the B-spin thus changing the local field experienced by the A-spin. The pump pulse ideally is a π -pulse which gives the strongest effect. The origin of the modulation is explained in the following:

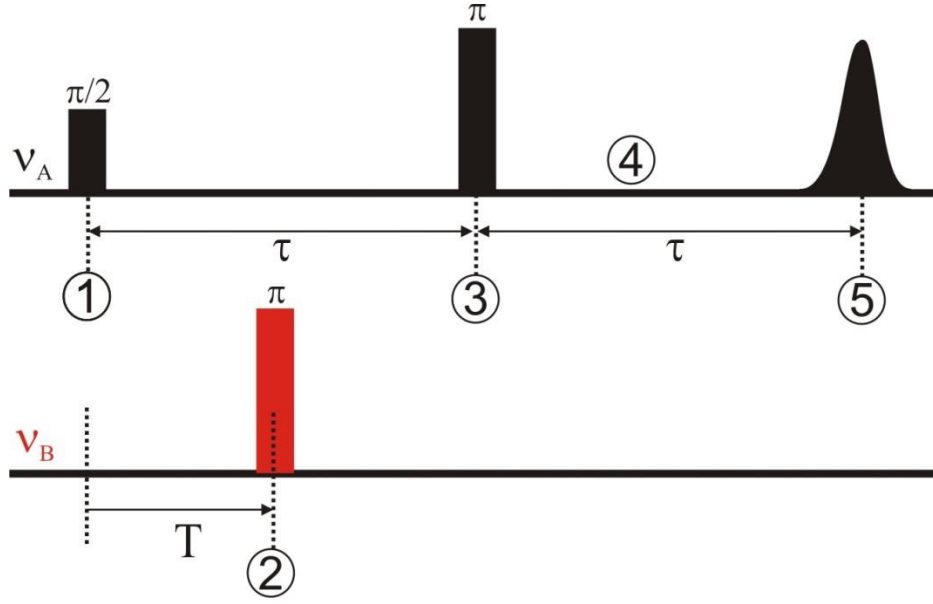


Figure 10 3-pulse PELDOR sequence. A two pulse Hahn Echo sequence is applied on the observer frequency ν_A whereas a single inversion pulse is applied on the B-spin frequency ν_B in the first τ -period.

Pulses with negligible duration are assumed. The dipolar coupling strength in radians is given by ω_{dip} . All other couplings are contained in ω_z .

The phase of the transverse magnetization at certain positions during the experiment (see Figure 10) can be written as:

Immediately after the $\pi/2$ pulse at position 1 the phase φ is zero:

$$\varphi(1) = 0 \quad (41)$$

At time $t = T$ the phase φ is given by

$$\varphi(2) = \omega_z T + \frac{1}{2} \omega_{\text{dip}} T \quad (42)$$

The pump pulse on the B-spin inverts the sign of the dipolar evolution. Furthermore inverts the π -pulse at position 3 the sign of the accumulated phase[24] thus at time $t = \tau$ at position 3:

$$\varphi(3) = -\omega_z \tau - \frac{1}{2} \omega_{\text{dip}} (2T - \tau) \quad (43)$$

At any position t in the second τ -period the phase is given by:

$$\varphi(4) = \omega_z(t - 2\tau) + \frac{1}{2}\omega_{\text{dip}}(2\tau - 2T - t) \quad (44)$$

At position 5 the Zeeman evolution is totally refocused but the pump pulse on the B-spin causes a phase of $-\omega_{\text{dip}}T$:

$$\varphi(2\tau) = \omega_z(2\tau - 2\tau) + \frac{1}{2}\omega_{\text{dip}}(2\tau - 2T - 2\tau) = -\omega_{\text{dip}}T \quad (45)$$

Yet this alone does not explain the experimental observation which is, that the Echo is modulated with the dipolar coupling frequency. At temperatures and fields where most PELDOR experiments are carried out one can assume that due to the low polarization, the probability of finding an A –spin coupled to a B-spin which is in α state is equal to the probability of finding an A-spin which is coupled to a B-spin in the β state. Thus one can split the A-spins in two manifolds, one with a B-spin pointing up which gives a phase of $-\omega_{\text{dip}}T$ and the other with a phase of $\omega_{\text{dip}}T$.

The transverse magnetization which is given by:

$$\vec{M}(t = 2\tau) \propto \begin{pmatrix} \sin(\varphi) \\ \cos(\varphi) \\ 0 \end{pmatrix} \quad (46)$$

Is then the two manifolds superimposed:

$$\vec{M}(t = 2\tau) \propto \begin{pmatrix} \sin(-\omega_{\text{dip}}T) \\ \cos(-\omega_{\text{dip}}T) \\ 0 \end{pmatrix} + \begin{pmatrix} \sin(\omega_{\text{dip}}T) \\ \cos(\omega_{\text{dip}}T) \\ 0 \end{pmatrix} = \begin{pmatrix} 0 \\ 2\cos(\omega_{\text{dip}}T) \\ 0 \end{pmatrix}. \quad (47)$$

The imaginary part of the signal is zero throughout the experiment which causes the Fourier transform of the dipolar evolution to be symmetric with respect to the zero-frequency. This corresponds to the fact that the pump pulse on the B-spin raises the Larmor frequency by the same amount in one manifold as it lowers it in the other manifold. Towards very low temperatures and high magnetic fields the cancellation is not complete due to the significant population difference, leading to an out of phase PELDOR described in[25].

4.4.2 The Pake doublet

PELDOR is applied to measure intramolecular distances. To do this the molecule has to be fixed with respect to the static magnetic field on the timescale of the experiment. If it is allowed to rotate during the experiment all angles θ (see equation (41)) occur and the dipolar coupling averages to zero. Therefore the sample is studied in a frozen solution where in most cases a glass like state is preferred which guarantees that all orientations are equally distributed. The consequence is a distribution of dipolar frequencies for a fixed interspin distance r . For a fixed distance r only the angle θ between the static magnetic field and the interspin vector \vec{r} (see Figure 9) varies the dipolar frequency (equation (41)). The angle θ is distributed with $P(\theta)d\theta = \sin(\theta)d\theta$ which gives rise to a Pake doublet which is symmetric to the zero point which due to the equal distribution of B-spins in alpha and beta state at typical PELDOR conditions.

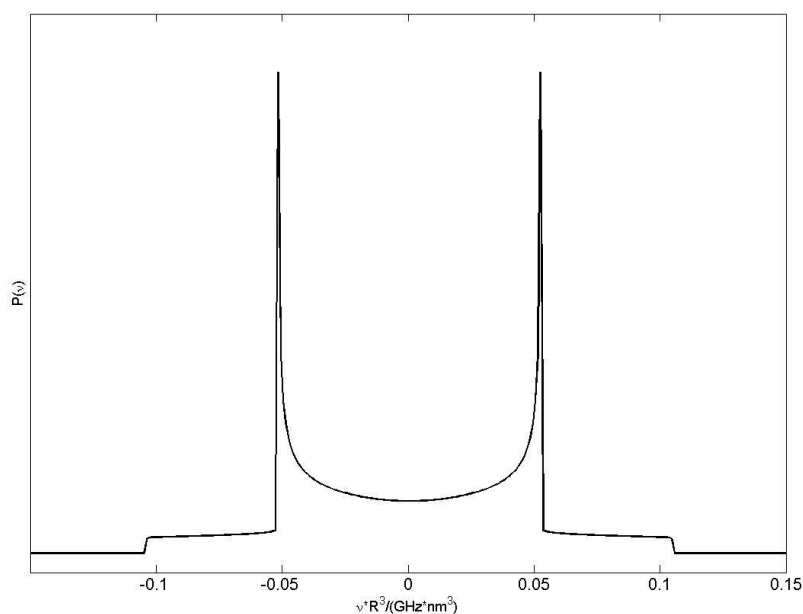


Figure 11 Pake doublet.

4.4.3 Time window and distance resolution

The interspin distance r is regardless of what type of fitting procedure is used is always determined by measuring the dipolar coupling frequency. The accuracy $\Delta\nu$ in determining a frequency is related to the time window ΔT in which the frequency can be observed by:

$$\Delta T \Delta \nu = 1 \quad (48)$$

The question how the frequency-time uncertainty translates into a distance-time uncertainty is addressed in the following. The dipolar frequency is related to the distance by :

$$\nu(r) = \frac{A}{r^3} (3 \cos^2(\theta) - 1) \quad (49)$$

For the following calculation only the singularity in the Pake pattern is considered which

means $\theta = \frac{\pi}{2}$ and therefore $\nu(r)_{\perp} = -\frac{A}{r^3}$.

With $\Delta\nu = \left(\frac{dr}{d\nu}\right)^{-1} \Delta r$ one obtains :

$$\Delta r = \frac{r^4}{3A\Delta T} \quad (50)$$

Equation (50) stresses the fact that for sufficient resolution in r-space for large distance very large time windows ΔT have to be used.

4.4.4 Effect of nuclear spin diffusion on T_2

The measurement time ΔT of a PELDOR experiment is half the time between the coherence generating 90° pulse and the position of the echo. If this time is increased the intensity of the echo decreases whether in an exponential or stretched exponential decay. All interactions which alter the Larmor frequency of a spin or introduce a sudden change of its phase during the echo sequence causes the spin not to refocus completely. There are three principle

decoherence mechanisms. 1) Electron spins which are antiparallel and dipolar coupled can undergo energy conserving flip flop processes:

A direct flip flop processes occurs between an observed spin A and its off resonant partner B which are dipolar coupled. If the B-spin is not flipped by the refocusing pulse the A spin refocuses at a time 2τ [26]. The amount of phase relaxation due to direct flip flop processes can be estimated by measuring the echo intensity as a function of the flip angle of the second pulse[27].

An indirect flip flop process occurs if two B-spins which are dipolar coupled to an observed A spin undergo a flip flop process which changes the local field experienced by the A-spin and hence its Larmor frequency. The indirect effect is much more pronounced than the direct effect[26].

2) Instantaneous diffusion occurs if the second microwave pulse flips adjacent spins which causes a change of the Larmor frequency of the observed spin and therefore introduces phase relaxation. Instantaneous diffusion can be quantified in combination with direct flip-flop processes by measuring the echo intensity as a function of the flip angle of the refocusing pulse. Under conditions where instantaneous diffusion plays a role longer and therefore less broadband refocusing pulses might lead to a higher S/N[28].

3) Librational motion of the spin bearing molecule in the presence of g and a-anisotropies cause a time dependent modulation of the Larmor frequency. For temperatures $T > 80$ K when the timescale of this motion is comparable to the timescale of the echo sequence librational motion is an additional contribution to phase relaxation [29]. The rotation of methyl groups also changes the local field. The rotation of matrix-methyl groups is not frozen at temperatures between 11-40 K [30]. The rotation of the methyl groups in the MTSSL spin labels is frozen below 60 K[31].

4) Nuclear spin diffusion is a T_2 process of magnetic nuclei, usually matrix protons which at low temperatures and low concentrations is the dominant phase relaxation mechanism[32]. Magnetic nuclei which are not detuned by the strong hyperfine field of the unpaired electron but still couple to it undergo energy conserving flip flop processes which are on the T_2 timescale of the nuclei. These change the local field at the electron spin causing phase relaxation which is governed by a stretched exponential law[30]:

$$E(2\tau) = E(0) \exp\left(-\left(2\tau/T_m\right)^x\right) \quad (51)$$

The echo intensity at time 2τ , $E(2\tau)$ depends on a power x in the exponent which is typically close to 2 for non-methyl proton containing solvents[30]. This time dependent relaxation rate as seen in the next paragraph is the reason to combine the Carr Purcel [33] sequence with the PELDOR sequence.

4.4.5 Minimizing the effect of nuclear spin diffusion by multiple refocusing

Carr and Purcell invented the Carr Purcell (CP) sequence to minimize the effect of translational diffusion on the phase memory time in solution NMR. In a CP sequence the transverse magnetization is refocused multiple times and each echo is measured. The phase error accumulated of a spin in solution due to field inhomogeneities gets smaller with the number of refocusing pulses in a given time[33]. Meiboom and Gill showed that if the coherence generating 90° pulse is in x-phase and the thereafter applied refocusing 180° pulses are in y-phase the errors of the refocusing pulses due to B_1 inhomogeneity and pulse imperfections do not accumulate [34].

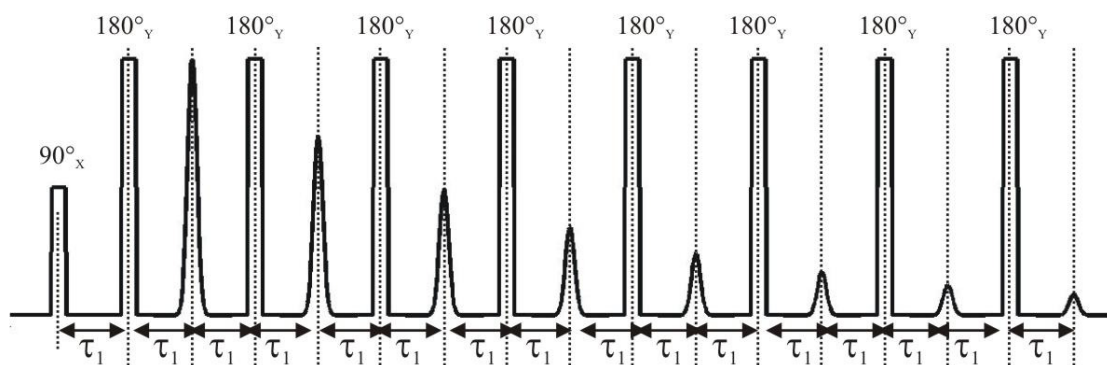


Figure 12 CPMG (Carr Purcell Meiboom Gill) sequence. For EPR applications an equal spacing between the refocusing pulses may be not appropriate due to overlay with echoes resulting from an inhomogeneous line comparable to the excitation bandwidth of the pulses.

Equation (51) states that the phase relaxation in the presence of nuclear spin diffusion is not governed by mono-exponential decay but a stretched exponential. If now the time between the

90° pulse and the observed echo is t and n refocusing pulses are applied the effective phase memory time changes as follows:

The echo intensity for the two pulse Hahn echo with a time 2τ between the 90° pulse and the echo is given by equation (51)

If the time $2\tau = t$ is split into n segments and a refocusing pulse is applied in each segment the echo intensity after time t is given by:

$$E(2\tau) = E(0) \left(\exp \left(- \left(\frac{t}{nT_M} \right)^x \right) \right)^n = E(0) \left(\exp - \left(\frac{t}{n^{\frac{x-1}{x}} T_M} \right)^x \right) \quad (52)$$

The phase memory time T_M can be replaced with an effective phase memory time $n^{\frac{x-1}{x}} T_M$ which reduces for the common case of $x = 2$ [30] to $\sqrt{n} T_M$. The power of prolonging the observation of a coherence by multiple refocusing is demonstrated in Figure 13 where echos of a spin labeled non-deuterated protein are recorded with one, two and three refocusing pulses. The number of averages as well as the detector settings is the same for all three experiments. Noticeable is that the echo for only one refocusing pulse could not even be observed.

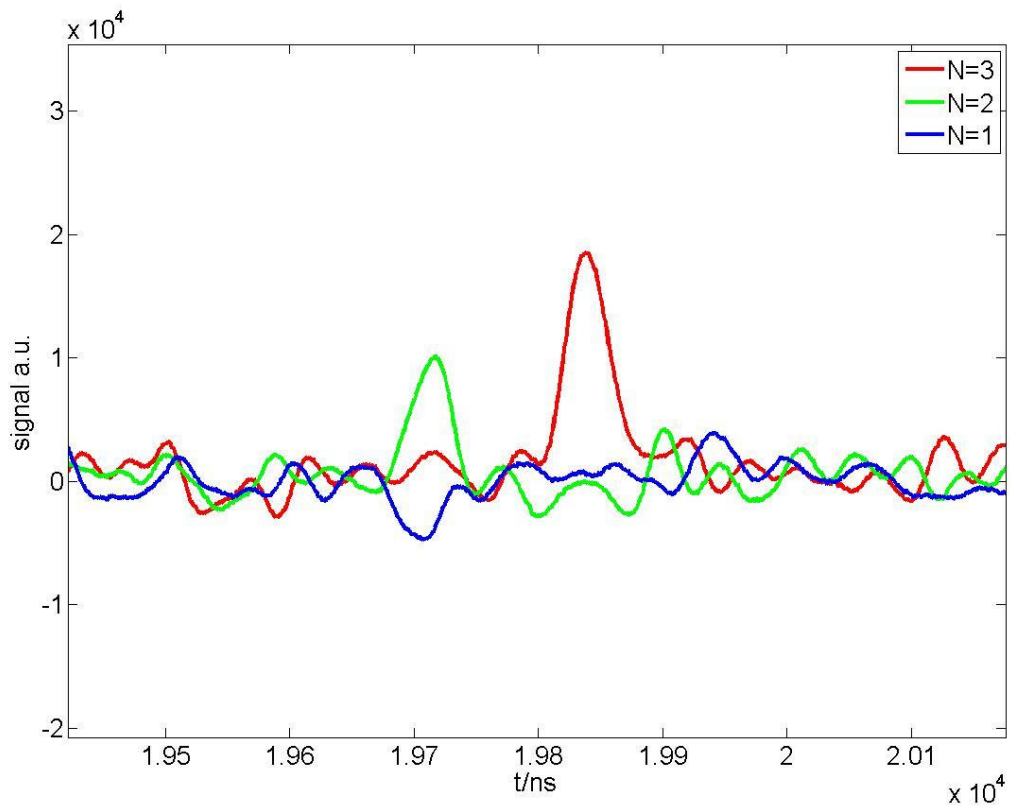


Figure 13 Echoes of a sample containing protons after roughly 20 μs . The blue line is recorded with one refocusing pulse, the green with two and the red signal was created with three refocusing pulses. In case of one refocusing pulse the echo should appear between 19.6 μs and 20 μs but is not observed in the noise. The green echo appears at 19.7 μs whereas the red echo appears after 19.8 μs .

5 Amplitude and phase modulated microwave pulses

5.1 Amplitude and phase modulation of microwave in the ns regime

Almost all pulsed EPR spectrometers up to date use fast microwave switches to create pulses. The basic principle is depicted in Figure 14. A cw-microwave (RF) source is switched by a fast PIN diode switch. These switches can only block or pass the incoming microwave thus generates only rectangular shaped microwave pulses

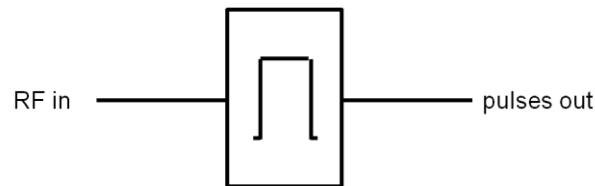


Figure 14 conventional pulsed EPR spectrometers use fast microwave switches to generate pulses.

The aim is to generate microwave pulses with arbitrary amplitude and phase. The basic scheme for amplitude modulation is depicted in Figure 15. The incoming cw-microwave (LO local oscillator) is multiplied by a control voltage (AWG) in a three port microwave device called mixer. The output microwave (RF) is proportional to the control voltage (AWG).

$$\text{RF}(t) = \text{AWG}(t) \cdot \cos(\omega_{\text{LO}}t) \quad (53)$$

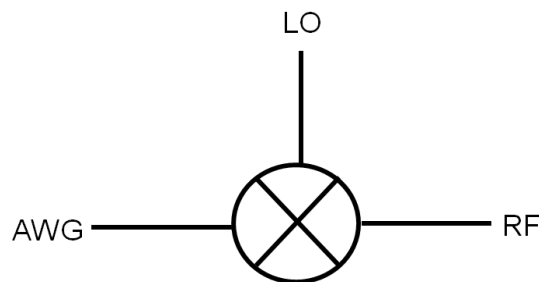


Figure 15 amplitude modulation of microwave (LO) by an control voltage (AWG)

This setup enables to produce microwave with an arbitrary amplitude modulation only limited by the individual bandwidth of the Waveform generator and mixer.

Here two modulators driven by LO carriers with a 90° phase shift are operated with two independent AWG's. The two modulator outputs are combined. This setup enables to

generate arbitrary amplitude and phase at the RF-output. The block diagram is shown in Figure 16.

$$RF(t) = AWG I(t) \cdot \cos(\omega_{LO}t) + AWG Q(t) \cdot \sin(\omega_{LO}t) \quad (54)$$

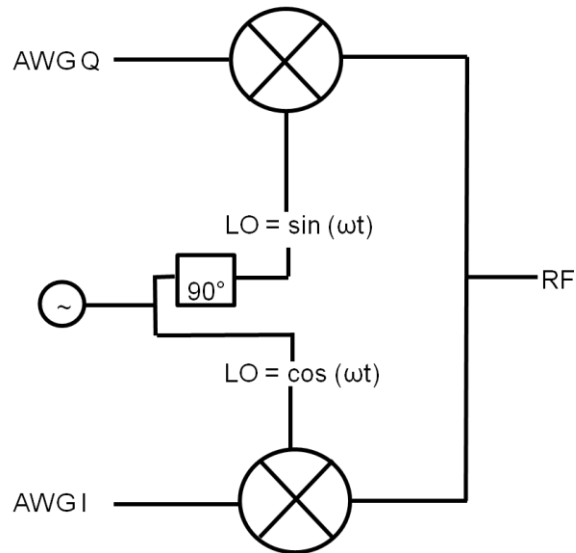


Figure 16 arbitrary amplitude and phase setup with two modulators driven by LO's which differ in phase by 90°.

5.1.1 The pulse-shaping unit

The two modulators with the phase shifter are combined to a single 4-port unit called IQ-mixer. The IQ mixer of the pulse-shaper is a marki IQ 0714LXP which has a remarkable high IF bandwidth of 500 MHz. The disadvantage of this integrated design is a slight LO frequency dependent deviation from the optimum 90 ° phase between the I and Q port of the modulator. The block diagram of the pulse-shaping unit is shown in Figure 17. The AWG itself consists of two independent programmable digital to analogue converters (DAC) with a 14-bit resolution which are clocked at 1 GHz giving a Nyquist frequency of 500 MHz. The DAC's are followed by a low-pass filter with a cut-off frequency of 450 MHz which remove the residual clock signal of 1 GHz. The Tschebyscheff filters have an almost flat response in the passband with a sharp cutoff at 450 MHz. The flat frequency response is achieved at the expense of moderate ringing at the cutoff frequency of approximately 450 MHz. The ringing occurs only if its characteristic frequency is contained in the waveform. The filtered DAC signal is amplified to -6 dBm to drive the I-Q inputs of the modulator. The modulator output

is further amplified by a CIAO wireless CA-24-280 amplifier. The AWG can play waveforms with a duration from 32 ns up to 32 μ s. The waveform can be divided in up to four segments. A ttl trigger at the segment trigger port of the AWG causes the AWG to play the next segment. The length of each segment has to be a multiple of 8 ns with a minimum duration of 32 ns.

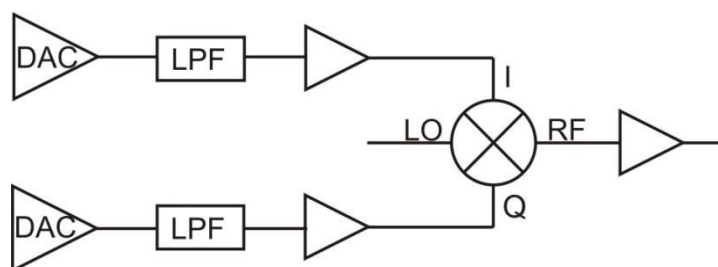


Figure 17 block diagram of the pulse-shaping unit

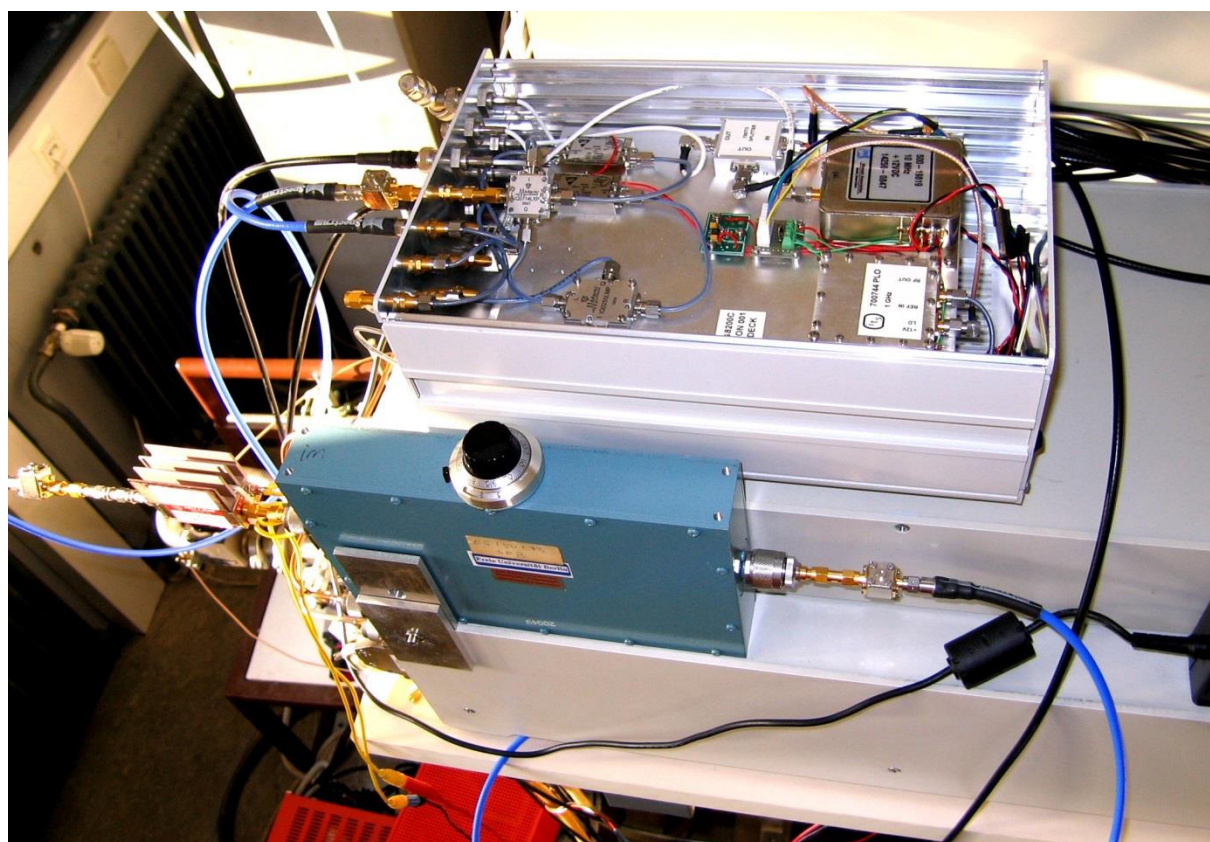


Figure 18 The pulsshaping unit connected to the ELDOR source for PELDOR applications

5.1.2 Alternative approaches

The group of Gunnar Jeschke used a different approach with a much faster clocked AWG which only needs one DAC channel and a double sideband mixer instead of a more complicated single sideband IQ mixer[35]. The AWG used by them is clocked at 12 GHz whereas the one used in this work operates at 1 GHz clock speed. An 8 GHz source is used as LO. Due to the large bandwidth of approximately 6 GHz of this AWG it is possible to upconvert the 8 GHz LO to 10 GHz by modulation. The lower sideband at 6 GHz can easily be filtered.

The modulation function of the AWG can be written as:

$$AWG(t) = A(t) \cdot \cos(\omega_{IF} t + \varphi(t)) \quad (55)$$

With:

$A(t)$: Amplitude modulation function

$\varphi(t)$: Time dependent phase

ω_{IF} : Difference frequency between local oscillator (LO) and spectrometer frequency

The mixer output $RF(t)$ is then:

$$RF(t) = A(t) \cdot \cos(\omega_{IF} t + \varphi(t)) \cdot \cos(\omega_{LO} t) = \frac{1}{2} A(t) (\cos((\omega_{LO} + \omega_{IF}) t + \varphi(t)) + \cos((\omega_{LO} - \omega_{IF}) t - \varphi(t))) \quad (56)$$

If ω_{IF} is large it is easy to remove the difference frequency $\omega_{LO} - \omega_{IF}$ by passive filtering.

Performance wise there are two major benefits of this design compared to the setup used here:

- 1) mixers always have a certain amount of LO feed through which may be disturbing if the LO frequency coincides with the spectrometer frequency. If the LO is largely separated from the spectrometer frequency as it is the case in the Jeschke setup LO leakage is not an issues.
- 2) A simple double sideband mixer can be used which omits the more complicated IQ mixer yielding a better phase response.

5.2 Implementing the pulse shaper into a Bruker Elexsys E580 Spectrometer

The setup shown on the left uses a retrofitted cw output from the microwave bridge as LO source. The benefit of this design is that all pulse channels (+x, -x, +y, -y) are maintained and can be used additionally to the shaped pulses. Since the power level of the cw output is fixed a variable attenuator has to be installed in the LO branch to precisely adjust the LO level of the modulator. An additional switch is necessary to block the the LO-leakage which is only 15 dB down when compared to the max. RF output power. The switch is driven by the Gate out-port of the AWG.

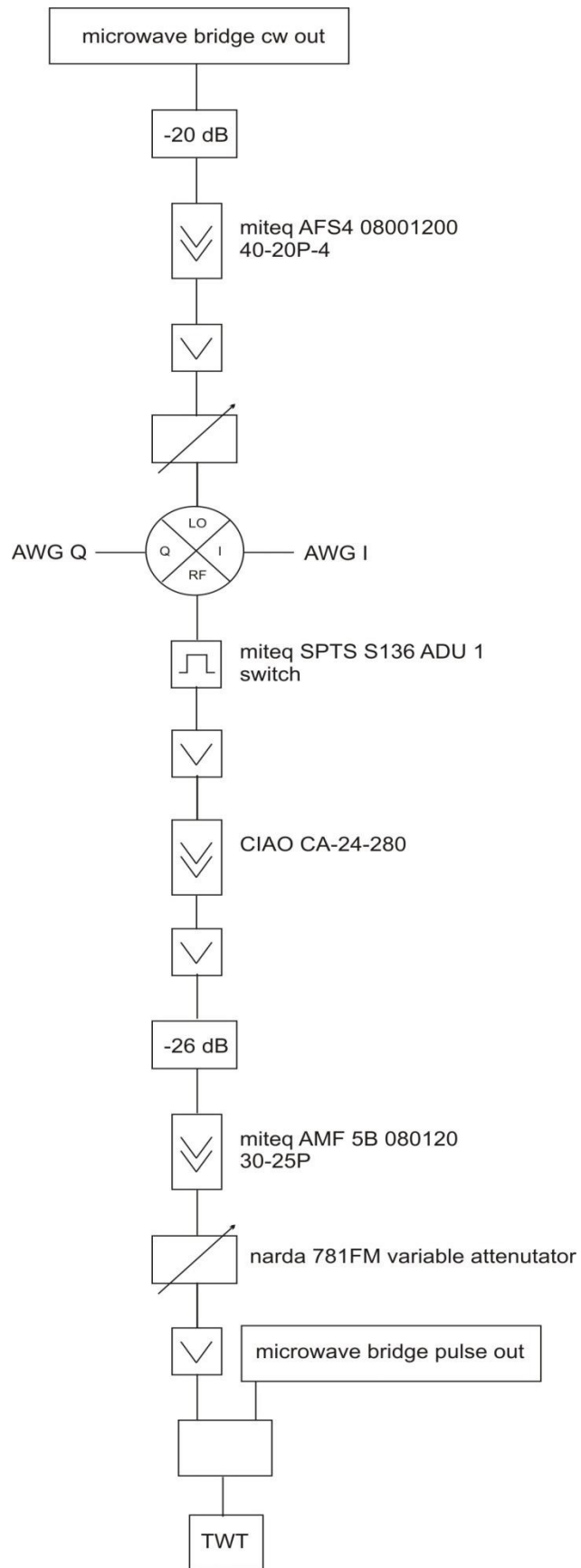


Figure 19 setup to generate shaped pulses while maintaining the standard +x, -x +y,-y channels.

The setup shown on the left utilizes the phase and amplitude network of the pulse bridge as an LO source. This setup allows generating shaped pulses with four different phases during an experiment. The power level in the LO branch is adjusted via the MPFU menu of the spectrometer software. The LO is pulsed which makes an additional switch, which blocks the LO leakage dispensable. The shaped pulses are routed to the TWT amplifier. The pulse power is adjusted via the narda attenuator.

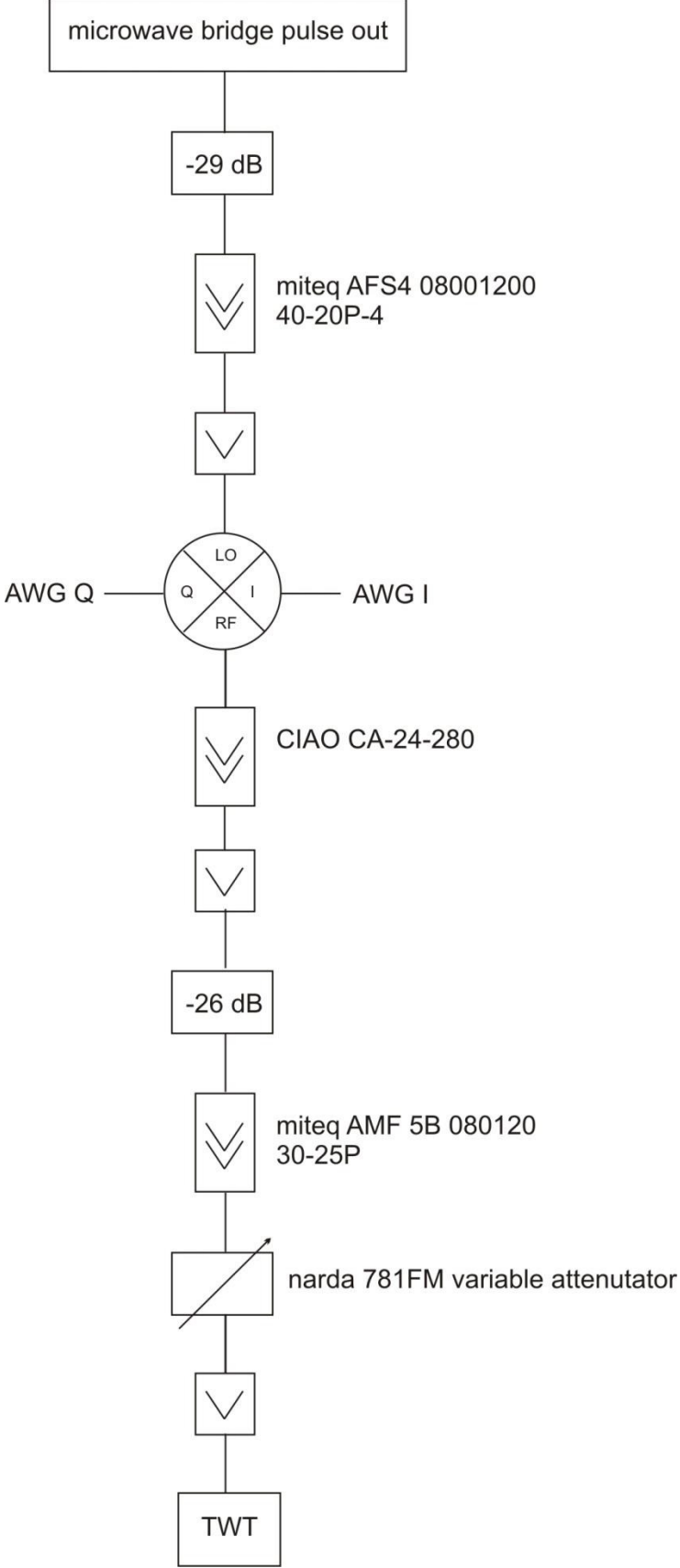


Figure 20 setup to generate shaped pulses using the amplitude and phase network of the microwave bridge as LO source

The setup which is shown on the left enables shaped pulses with a non-phase locked second ELDOR source. Due to the variable power output of the EDLOR source a variable attenuator in the LO branch is not necessary.

The shaped ELDOR pulses are routed to the ELDOR input of the main microwave bridge. The variable narda attenuator is used to adjust the power of the eldor pulses. An adjustment via the ELDOR menu is not possible with shaped pulses due to the fixed LO level.

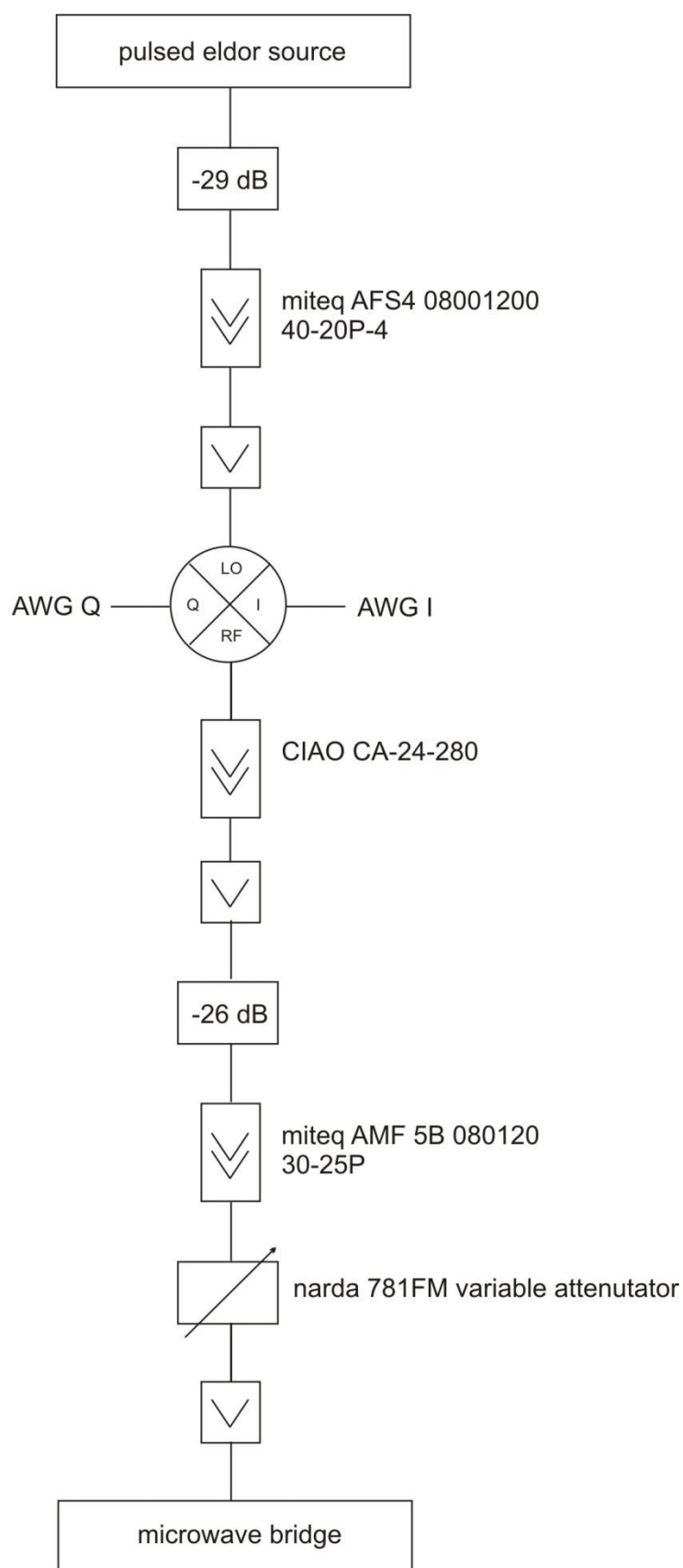


Figure 21 setup for shaped ELDOR pulses

5.3 Calibration of the pulse-shaper

Ideally with both IF-ports grounded no RF output should be measurable for an IQ mixer. This however is not the case and a substantial amount of LO can be measured at the RF port. This LO leakage is typical for mixers and can be reduced by applying DC-offsets to the I and Q ports of the modulator. The GUI of the AWG supplies the possibility to apply individual DC-offsets to the I and Q port of the modulator to reduce the LO-leakage. The DC-offset is generated by the DAC itself. For the 14-bit DAC's built into the AWG the output voltage is proportional to the DAC input in binaries ranging from -8192 – 8192 and cannot exceed these values. If for example a DC offset of 500 (in binaries) is applied the total dynamic range is reduced by 500 and the possible DAC input ranges from -8192 – 7692.

If one applies a certain IF-level to the I or Q-port of the modulator the measured RF level will vary dependent on LO drive level and frequency. This baseband amplitude deviation can also be compensated in the GUI calibration menu by channel scaling factors. These scale the stored waveform by a factor to achieve amplitude balance between the I-and Q channel. The scaling also reduces the resolution of the AWG which is not critical.

The pulse shaper was calibrated for each experiment. The procedure can be executed out as follows:

- 1) Apply a LO of the intended frequency with a power level of approximately 10-13 dBm .
- 2) Connect a microwave diode (midisco mdc1118-S) to the output of the narda variable attenuator (see Figure 19, Figure 20, Figure 21).
- 3) Connect the diode output to an oscilloscope
- 4) Load a waveform into the AWG memory consisting of four pulses of equal duration and magnitude for each phase (+x, -x,+y,-y).
- 5) Vary the LO power level such that the signal from the diode for the x pulses is approximately equal to the signal of the y pulses.
- 6) Adjust the DC-offset for the I – channel of the AWG in such a way that the amplitude of the +x pulse is the same as the amplitude of the –x pulse. The same has to be accomplished for the y pulses via the Q-channel offset.

- 7) Adjust the scaling factors for the I and Q channel until the amplitude of the x-pulses is equal to the amplitude of the y-pulses.

5.4 Synchronizing the AWG with the spectrometer

The AWG operates on an internal time base of 8 ns. A waveform is triggered by one of the pulse channels of the Bruker E 580 console. Due to the 8 ns time basis of the AWG a jitter of 8 ns between the waveform and the trigger pulse is present. To reduce this jitter a synchronization of the AWG with the spectrometer was done by connecting the 125 MHz TTL signal from the AWG to the external trigger input of the spectrometer and operating it in the external trigger mode. Care should be taken if the position of a shaped pulse is incremented in time during the experiment. If this is the case, a time increment which is a multiple of 8 ns should be chosen.

6 Results and Discussion

6.1 Broadband excitation of transverse magnetization

6.1.1 Broadband excitation of Fluoranthene

The simplest task for a broadband pulse is to excite transverse magnetization with uncorrelated phase which means that it cannot be refocused. The application of such pulses is limited to magnitude Fourier transform EPR spectroscopy in liquids where no inhomogeneous broadening occurs and therefore a FID (free induction decay) is measurable. Since power is the bandwidth limiting factor in EPR spectroscopy comparisons of new pulses were made with rectangular pulses of the same power. The excitation profile is measured with fluoranthenyl-hexafluorophosphate radicals exhibiting a very narrow linewidth of 1 μ T[36, 37].

The hyperfine interaction averages out due to the mobility of the conducting electrons in the crystal. The sample is a single crystal of fluoranthenyl-hexafluorophosphate which behaves like an uncoupled electron spin and is therefore well described by the Bloch equations. The excitation profiles have been measured by keeping the spectrometer frequency fixed while changing the static field B_0 to change the resonance frequency of the sample. At each frequency offset the FID was recorded and Fourier-transformed. These spectra have then been summed up to obtain the excitation profile of the pulse.

The broadband excitation pulse was generated by means of optimal control theory and belongs to the BEBOP-family (broadband excitation by optimized pulses)[38]. The pulse was originally optimized for a peak B_1 field of 3 MHz which was available in our S-band spectrometer operating at 3.5 GHz with a solid state amplifier. The pulses consist of 100 20 ns sub-pulses which give 100 amplitude and 100 phase values which had to be optimized. The pulse was optimized taking into account a mw inhomogeneity of $\pm 10\%$ which means that it excites transverse magnetization within a B_1 field range of 2.7-3.3 MHz .

The pulse which was initially optimized for a bandwidth BW_0 can be converted to a different bandwidth BW_1 by scaling the timescale by a factor $\frac{BW_0}{BW_1}$ and multiplying the amplitude by

$\frac{BW_1}{BW_0}$. The results shown in the following were obtained with the BEBOP pulses scaled to

200 MHz bandwidth. The pulse shape described by an amplitude modulation function for x- and y channel is depicted in Figure 22.

The following results were obtained on a Bruker Elexsys E580 spectrometer modified with the pulseshaping unit described in 5.1.1. The Spectrometer was outfitted with a Bruker MD5 probe which was maximally overcoupled to minimize bandwidth limitations. The spectrometer frequency was set to 9.642 GHz. The sample was located in a 4 mm standard quartz EPR tube.

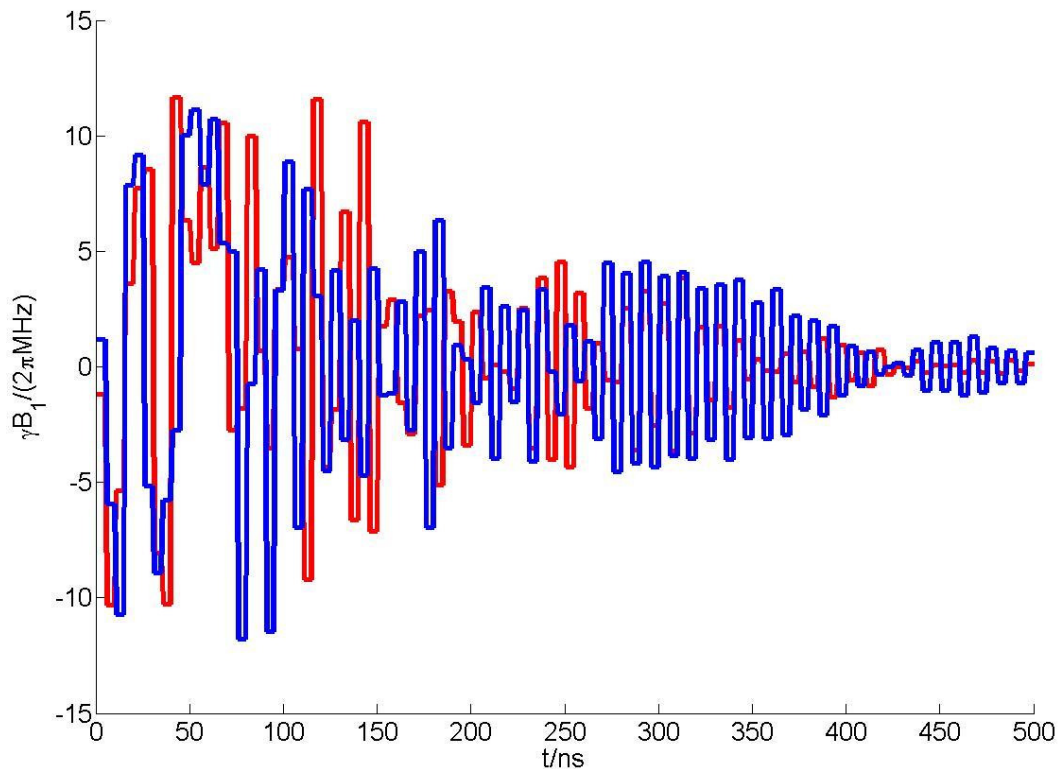


Figure 22 Bebop pulse originally optimized for 50 MHz bandwidth and duration 2000 ns with peak B_1 of 3 MHz rescaled to a bandwidth of 200 MHz and a duration of 500 ns with a peak on resonance nutation frequency of 12 MHz.

The 90° rectangular excitation pulse with an on resonance B_1 nutation of 12 MHz has a duration of 20.8 ns. The comparison of the rectangular pulse with the optimum control derived pulse is shown in Figure 23. The actual pulse shape is shown in figure a and a'. The total energy which is contained in the bebop pulse is a factor of 10 larger than for the rectangular pulse. But a rectangular pulse having approximately the same bandwidth and fidelity within 200 MHz would require an excitation field strength of at least 120 MHz which

then gives a 2.8 ns 90° pulse containing the same energy as the 200 MHz bebop pulse. Figure 23 b and b' show the simulated magnitude transverse magnetization after the pulse neglecting relaxation. Figure 23 c and c' show the measured excitation profiles for the 20.8 ns 90° pulse and the 200 MHz bebop pulse. Each spectrum consists of 300 individually recorded FIDs at different static magnetic fields incremented ranging from $\pm 35,7$ G the on-resonant field. The decay in signal intensity which is visible especially for the bebop pulse towards higher offsets is due to the limited frequency response of the video amplifier in the spectrometer detection path. To measure the bandwidth of the video amplifier frequency chirps generated with the AWG from 0-100 MHz have been recorded with an oscilloscope (Tectronix TDS 5034B) once routed through the video amplifier and once bypassed. The ratio of those signals yielded the video amplifier frequency response shown as a black line in Figure 23 c and c'. In case of c' the bandwidth of the video amplifier gives the envelope of the excitation profile which means that the pulse works in very good agreement with its simulation. It also means that this type of pulse is robust against linear and nonlinear distortions in the pulse generation amplification and coupling to the sample by the microwave resonator which turned out to be a

severe limitation for the later introduced prefocused pulse.

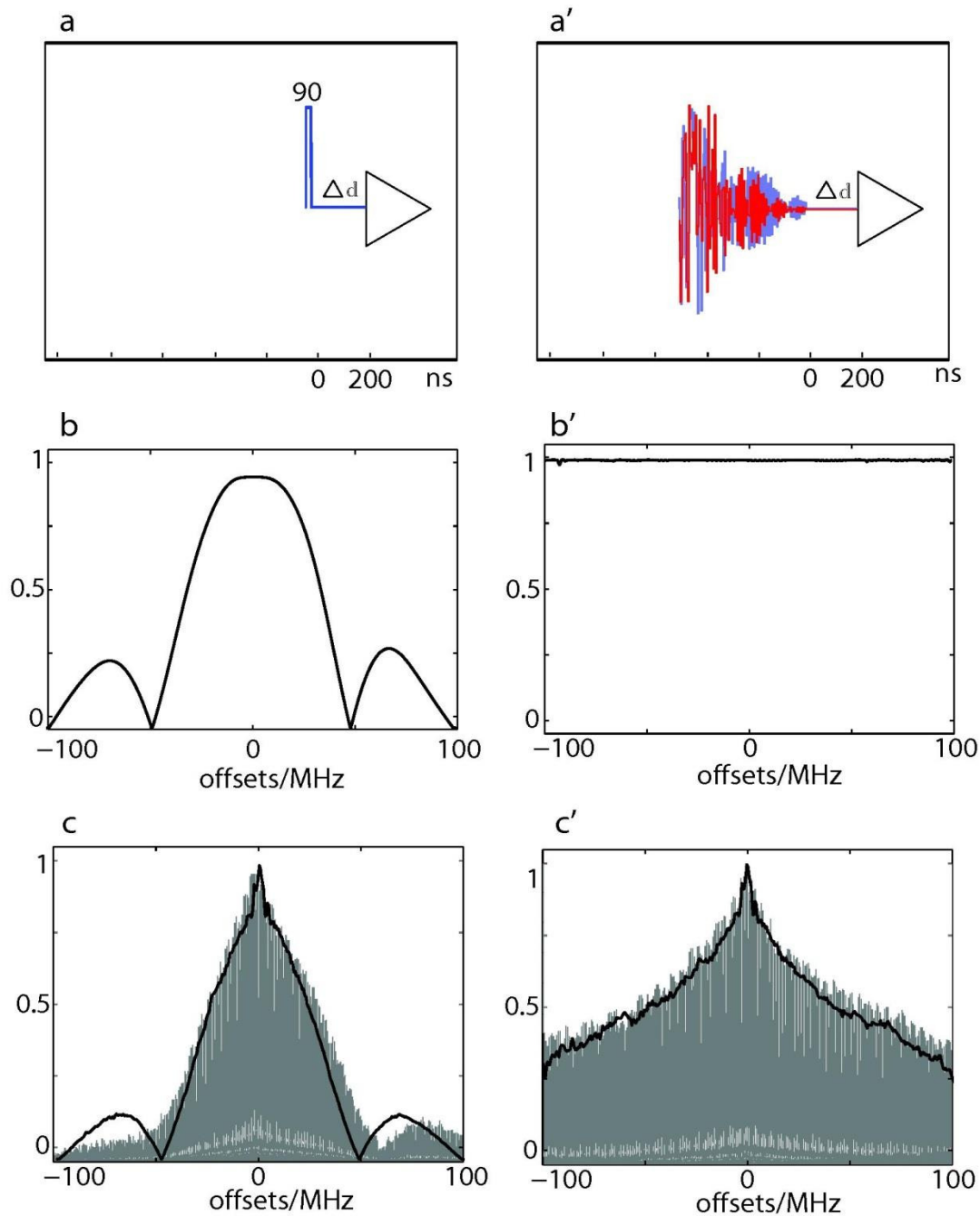


Figure 23 [39] comparison of a 200 MHz bebop pulse with a rectangular pulse utilizing the same peak B_1 field of 4.3 G. The left column compares the rectangular pulse to the BEBOP-pulse shown in the right column. Top: pulse-shape; middle: simulated magnitude transverse magnetization; bottom: measured magnitude-excitation profiles(grey) with the calculated excitation profiles shown in the middle multiplied with the frequency response of the video amplifier.

6.1.2 Broadband liquid state FT-EPR

Magnitude Fourier transform pulse EPR spectroscopy is applicable to organic radicals in liquids where the anisotropies are averaged by rotational motion of the molecule and therefore the homogeneous linewidth $\Delta\nu$ given by $\Delta\nu = T_2^{-1} = T_1^{-1}$ determines the observer time window for the fid. The structure of the spectra is determined by isotropic hyperfine interactions with almost no inhomogeneous line broadening. The substance used here for demonstration purpose is the radical form of Phenalenyl or Perinaphtenyl dissolved in mineral oil. The radical itself is shown in Figure 24 PNT radical..

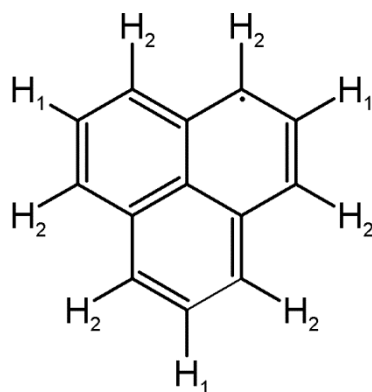


Figure 24 PNT radical.

The following comparison of the bebop pulse scaled to 200 MHz bandwidth with a rectangular pulse of the same peak B_1 field clearly shows the advantages a broadband pulse can have over the classical pulse.

Figure 25 a shows a simulated stick spectrum of PNT which was calculated using isotropic hyperfine couplings determined by cw-EPR-spectroscopy. Figure 25 c shows the magnitude fourier transform spectrum of PNT excited with a 21 ns long rectangular pulse which has to be compared with Figure 25 b where the magnitude fourier transform spectrum obtained with the 200 MHz bebop is shown. The two central lines are down by a factor of 0.6 compared to the rectangular pulse due to phase relaxation during the pulse. When it comes to fidelity of the whole spectrum, the bebop pulse clearly outperform the rectangular pulse due to its homogeneous excitation efficiency throughout the bandwidth. The ratio of the transitions appearing at -2.5 MHz and -38 MHz should be 3 which is almost fulfilled by the bebop pulse with a ratio of 3.8 after correction of the video amplifier frequency response. The rectangular pulse gives under same treatment a ratio of 9.8.

If the field is set 19 G off resonance, corresponding to 53 MHz, the importance of fidelity is stressed even more. The spectrum excited with the rectangular pulse (Figure 25 e) shows strong distortions of the true shape whereas the bebop pulse (Figure 25 d) still manages to excite the whole spectrum with good fidelity. In case of the off-resonant comparison the signal loss due to phase relaxation is more than compensated.

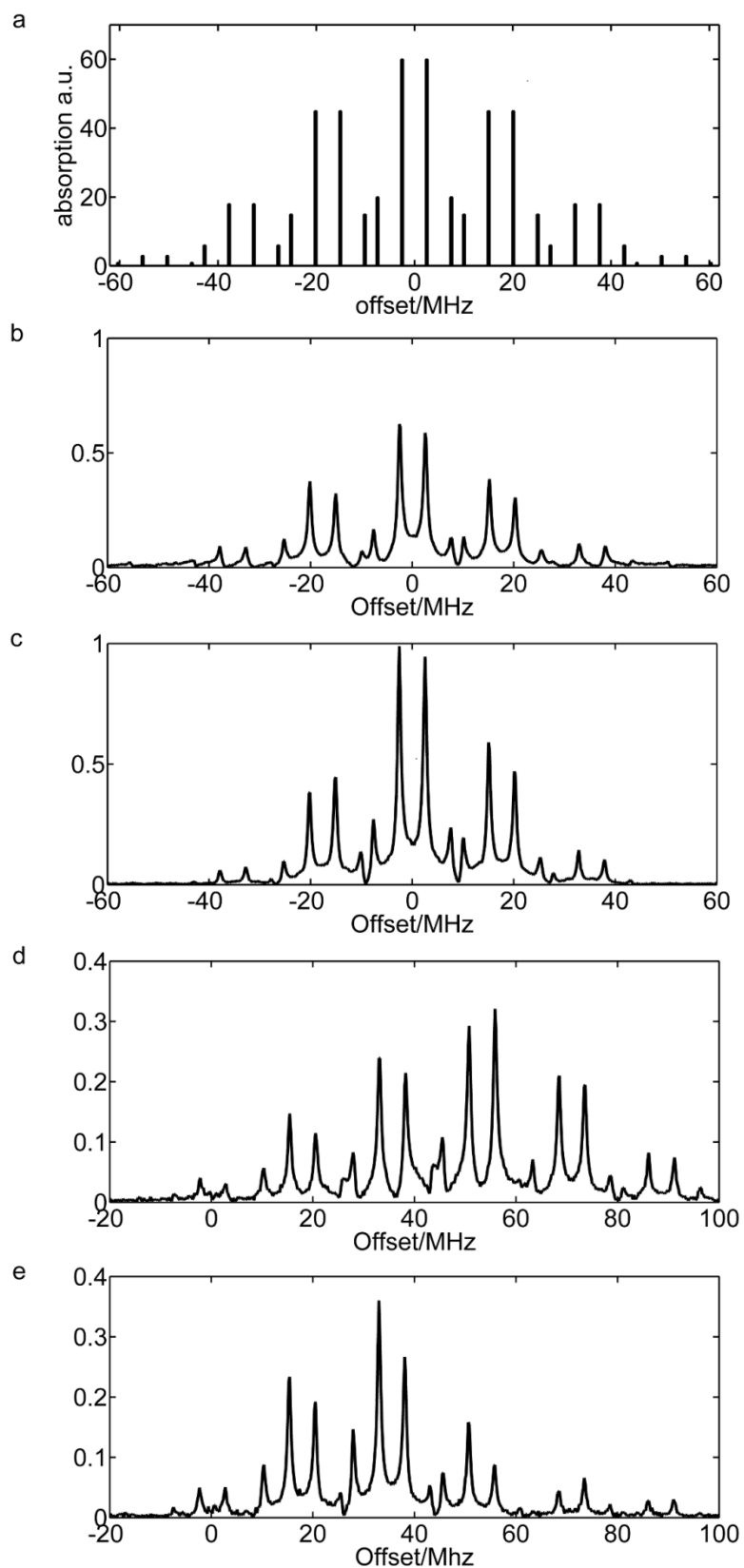


Figure 25 [39] Magnitude Fourier transform spectra of 1 mM PNT in mineral oil measured at room temperature. Stick diagram of hyperfine spectra (a). Experimental spectra excited in the center of the EPR spectra with the bebop pulse (b) and with a 21 ns 90° pulse(c). Experimental spectra excited 53 MHz off-resonance from the center with the bebop (d) and with a 21 ns 90° pulse (e).

6.1.3 Linear Pulse distortion and its effect on optimal control prefocused pulses

Every component which is in the signal transducing pathway has a non-flat frequency response and gives therefore rise to pulse distortions which causes that the calculated pulse-shape deviates from the pulse seen by the electron spin in the resonator. This means that the final state of the spin system may deviate strongly from the desired target state. If this is the case the distortions should be quantified and taken into account during the pulse optimization..

6.1.4 Spectrometer Impulse response function

The distortions can be split into a nonlinear part like the saturation of an amplifier and a linear part due to a non-flat frequency response. The non-linear part is skipped throughout this work due to its minor role compared to the linear distortions. The whole spin excitation path which includes the AWG with the modulator as well as every microwave cable and amplifier and to a large extend the microwave resonator contribute to the frequency response of the system. All time invariant linear distortions i.e. they have no memory regarding their input can be treated by means of linear response theory. Linear response theory states that once the answer of the system to a delta shaped input function is known the output $y(t)$ of any input function $x(t)$ can be calculated[40]. The response to the delta function which is called the impulse response function $h(t)$ of the system contains all linear phase and frequency information of the system.

$$y(t) = \int_{-\infty}^{\infty} h(t) x(t - \tau) d\tau \quad (57)$$

In principle every component has its own impulse response function so the total impulse response function of a chain of linear time-invariant systems is given by the convolution of the individual response functions.

Since a delta shaped function cannot be created as an input function and numerical deconvolution of the impulse response out of a measured signal is unstable a different approach by means of a pseudo stochastic MLS sequence $m(t)$ was applied[40]. A mls (maximum length sequence) is created by a liner feedback register and has the property that the autocorrelation approximates the delta function.

$$y(t) = \int_{-\infty}^{\infty} h(\tau)m(t - \tau)d\tau \quad (58)$$

$$\int_{-\infty}^{\infty} y(t)m(t + x)dt = \int_{-\infty}^{\infty} \int_{-\infty}^{\infty} h(\tau)m(t - \tau)m(t + x)dtd\tau \quad (59)$$

Yields with $\int_{-\infty}^{\infty} m(t - \tau)m(t + x)dt = \delta(x - \tau)$:

$$\int_{-\infty}^{\infty} y(t)m(t + x)dt = \int_{-\infty}^{\infty} h(\tau)\delta(x - \tau)d\tau = h(x) \quad (60)$$

A 13 bit linear feedback shift register with one XOR gate between position 12 and 13 was used here. The initial values have been set to [1 0 1 0 0 0 1 1 0 0 0 0 1] The matlab code to generate the sequence is given in the appendix. An excerpt of the 2^{13} ns = 8192 ns long sequence is shown in Figure 26. The autocorrelation function of this sequence is shown in Figure 27.

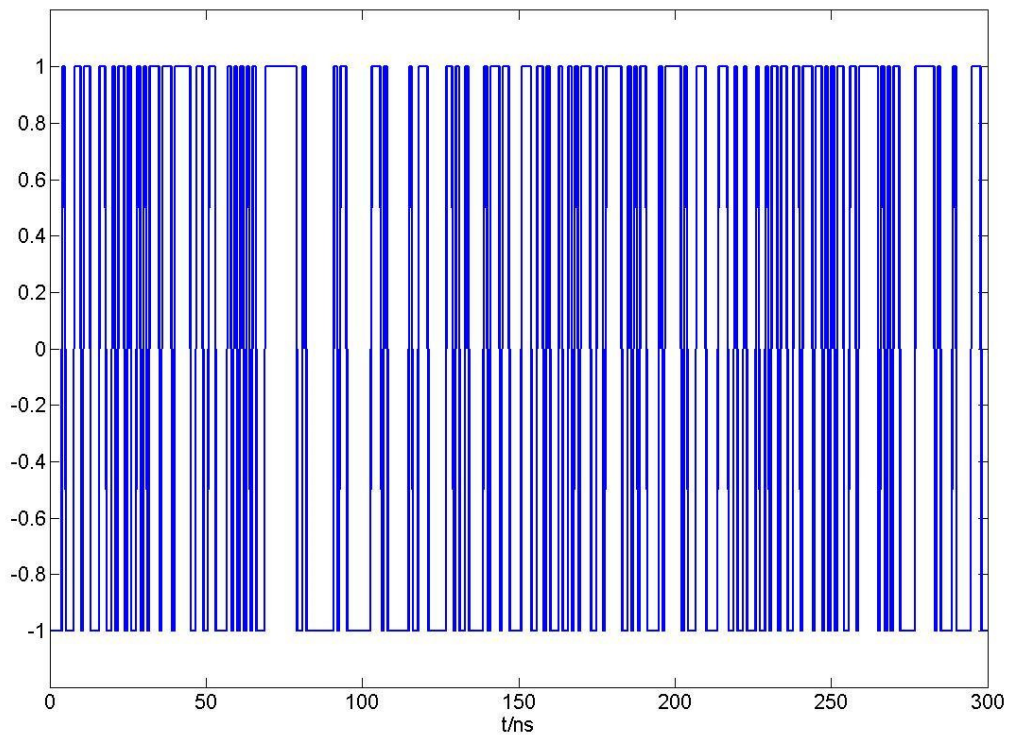


Figure 26 excerpt of the 13-bit mls sequence which was actually used to determine the spectrometer response function $h(t)$. The total length of the sequence is $2^{13} = 8192$ ns.

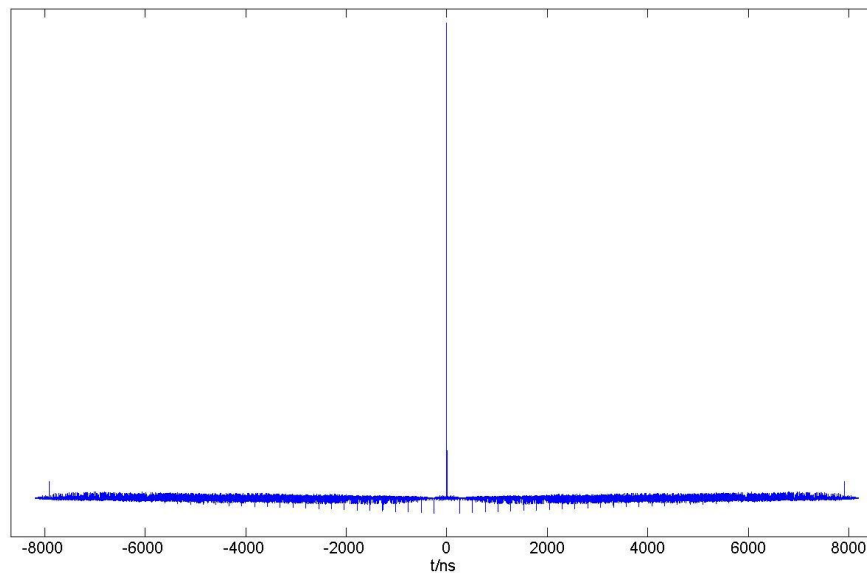


Figure 27 Autokorrelation of the 13 bit mls sequence which was used to determine the spectrometer response function $h(t)$.

Since the AWG itself is able to create the mls input function no other test-signal generator is needed. A field pick up coil made out of a 2.8 mm semi rigid coaxial cable with silver plated

copper inner and outer conductors was used as B_1 monitor. The inner conductor was bent to a small loop and soldered to the outer conductor. Ideally, the output function $y(t)$ has to be measured inside the resonator where the spins are located for the EPR experiment. Experimentally observations showed that the resonance is lost if the field pick up coil was inserted into the resonator. To avoid disturbances of the resonator the pick up coil was brought only into the stray field 3-5mm above the resonator to measure the B_1 field. The experimental setup is drafted in Figure 28. Standing waves which are not experienced by the spins inside the resonator are superimposed to the signal from the stray-field of the resonator and cannot be separated from it.

The measured output signal is also convoluted by the response function of the detection mixer (Mitec DB0418LW1) and the oscilloscope (Tectronix TDS5034B). In the following analysis these contributions are omitted since the bandwidth of the oscilloscope (300 MHz) and the detection mixer (500 MHz) is higher than the bandwidth needed for the broadband pulses (100 MHz). A Bruker probe equipped with a MD5 resonator was used for determining the impulse response function.

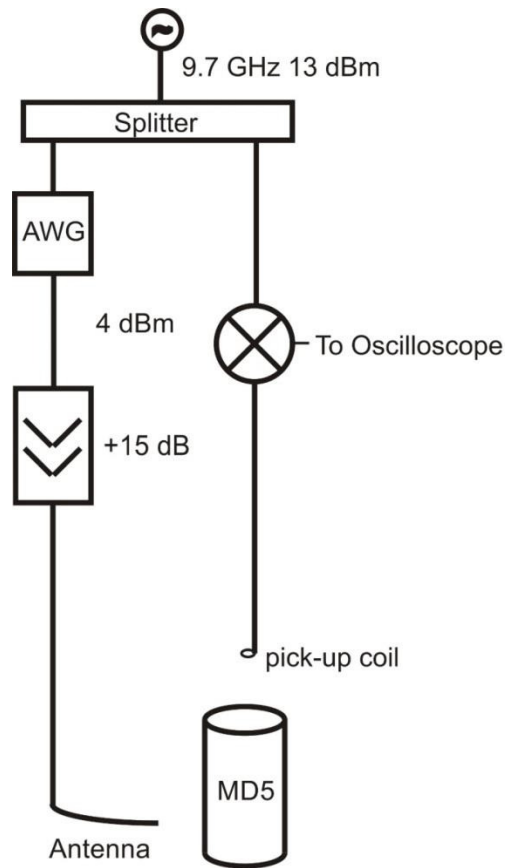


Figure 28 [39] Experimental setup to measure the B_1 field in the stray field of the resonator.

The mls input signal is applied only in one channel whereas the detection of the output signal showed that in the in-phase as well as in the quadrature component signal is present which leads to a complex impulse response.

The measured output as well as the input mls-sequence is shown in Figure 29 . The in phase component is blue and the quadrature component is drawn in red. No IQ-mixer which generally have a phase error of up to 5° was used for detection of the signal. Instead a double sideband mixer (miteq DB0418LW1) was used with a LO phase shifter which is not shown in Figure 28 was used to measure the in-phase and quadrature component subsequently.

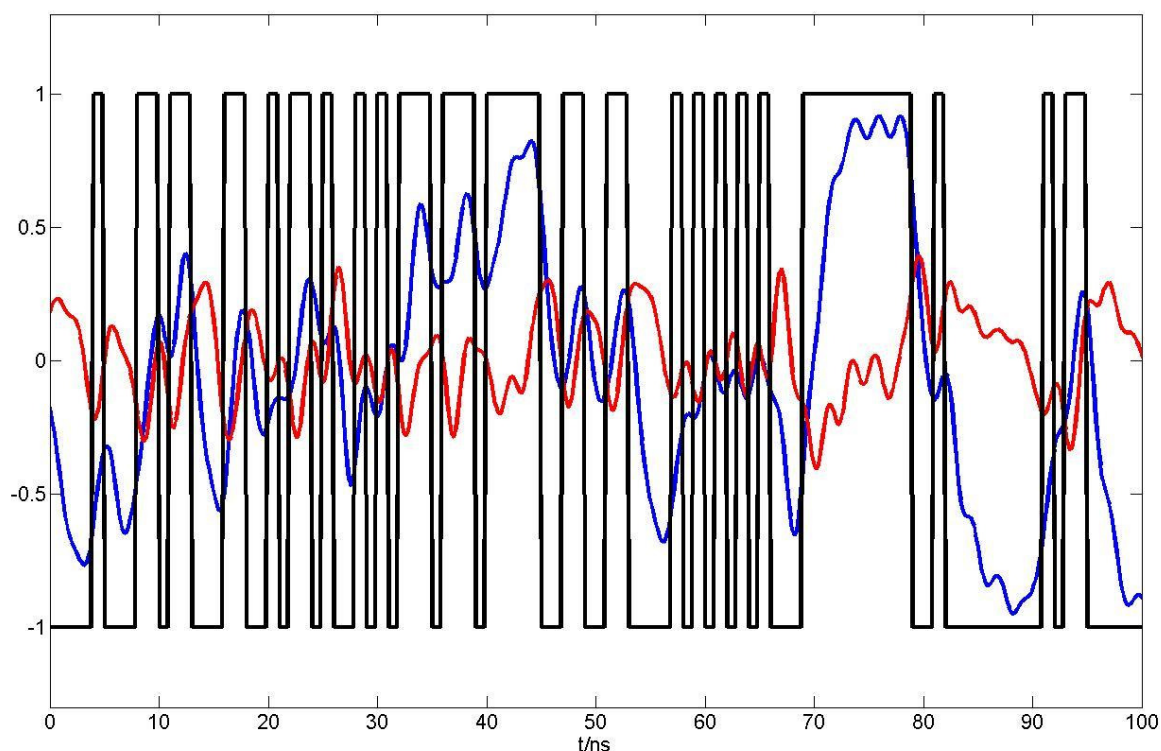


Figure 29 The input MLS sequence (black) with the measured B_1 response in in-phase (blue) and quadrature component (red). The field pick up coil was brought into the stray field app. 3-5mm above the MD 5 resonator.

The answer of the spin excitation path to the MLS test sequence is then convoluted with the input function to obtain the impulse response function which is shown in Figure 30. The response function is complex which means that the phase response is non-flat which is to be expected for a resonance structure. The impulse response function is the Fourier transform of the complex frequency response of the system. The complex frequency response of the spin excitation path calculated with the impulse response is shown in Figure 31.

To test the fidelity of the measured response function a test excitation pattern was measured with the method described in chapter 6.1.1. The pulse amplitude was set to 18 MHz instead of 20 MHz the latter is the value the pulse was optimized for. This power miscalibration combined with the frequency response of the spectrometer created a unique hole profile in the excitation pattern (Figure 32 black : overlaid Fourier transformed fluoranthene FIDs). This pattern was simulated based on the Bloch equations with the undistorted (Figure 32 blue line) as well as the distorted pulse shape (Figure 32 red line). The distorted pulse shape was obtained by convolution with the measured impulse response function. The qualitative shape of the excitation pattern is given by both simulations whereas the quantitative shape, especially

towards higher offset frequencies, is only reproduced by the simulation which takes the impulse response into account.

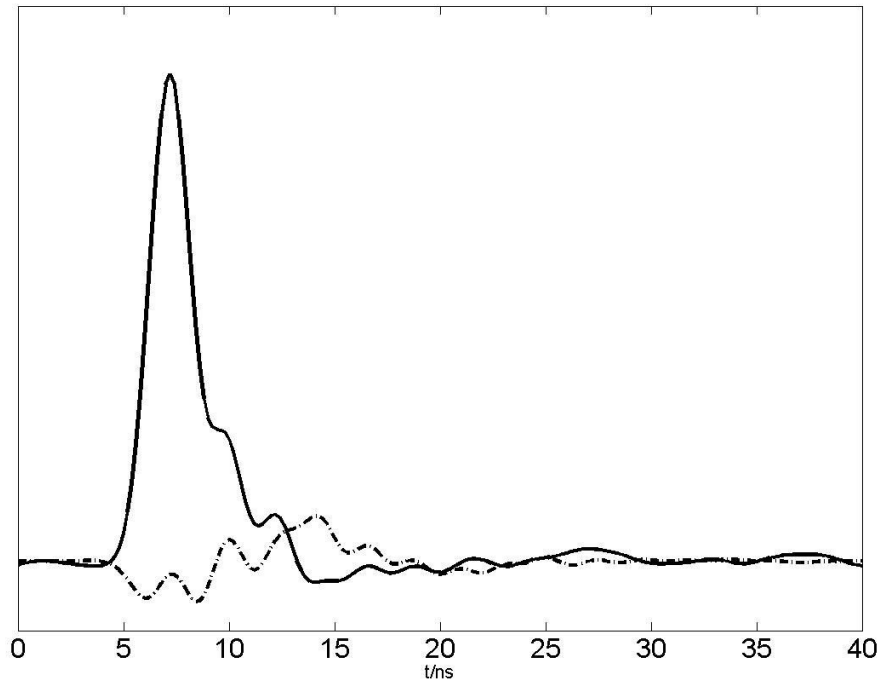


Figure 30 [39] Impulse response function obtained with the 13-bit mls sequence. In-phase component is drawn in solid black, quadrature component dashed.

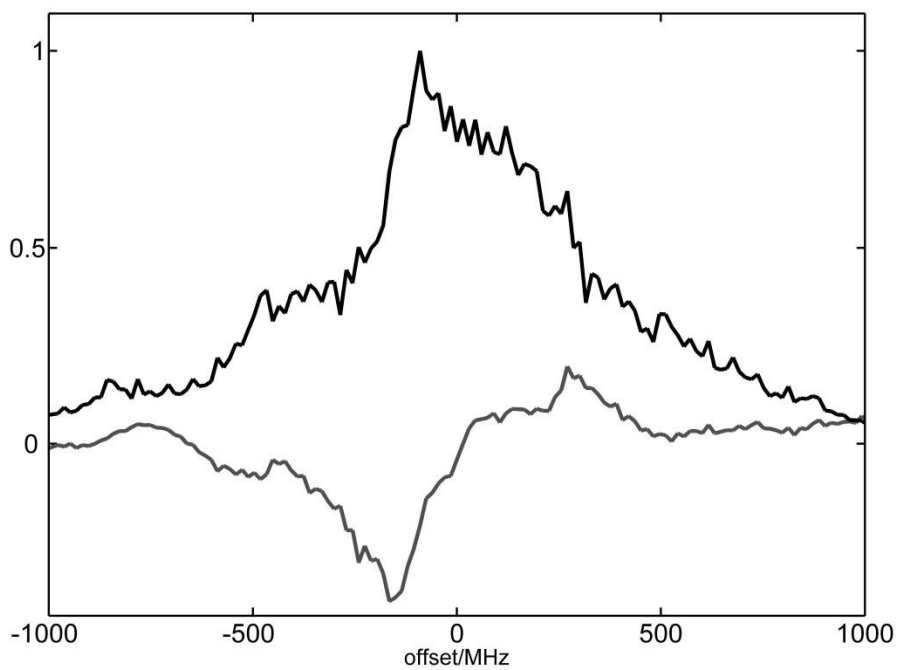


Figure 31 [39] Frequency response obtained with the impulse response shown in Figure 30. In phase component (black) and quadrature component (grey).

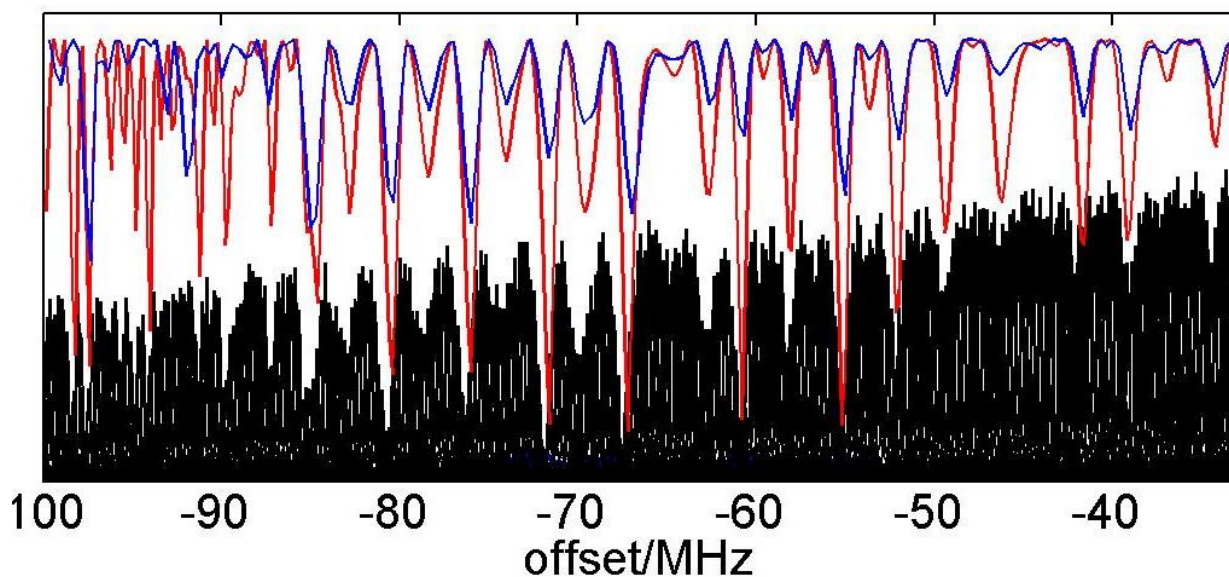


Figure 32 Magnitude-excitation pattern (measured: black) with simulations taking the impulse response into account (red line) and with the undistorted pulse (blue line).

A prefocused pulse can be considered as an excitation pulse and refocusing pulse with a fixed delay time. The advantage of optimizing both the excitation pulse as well as the refocusing pulse is a cooperative effect which might lead to a shorter pulse duration than two individually optimized pulses[14, 15]. The crucial parameter describing the properties of a prefocused pulse is the phase slope R which is for a pulse of duration T defined as:

$$R = \frac{\partial \varphi}{T \partial \omega_{\text{off}}} \quad (61)$$

With φ being the phase of the transverse magnetization at the end of the pulse. The ideal would be a phase slope of $R=0$ which causes the magnetization to focus at the end of the pulse to avoid signal loss due to phase relaxation. In practice however the ringdown of the microwave cavity does not allow to record an FID signal before a typical deadtime is past. A negative phase slope causes the magnetization to focus at a certain time after the end of the pulse which is preferable after the spectrometer-deadtime.

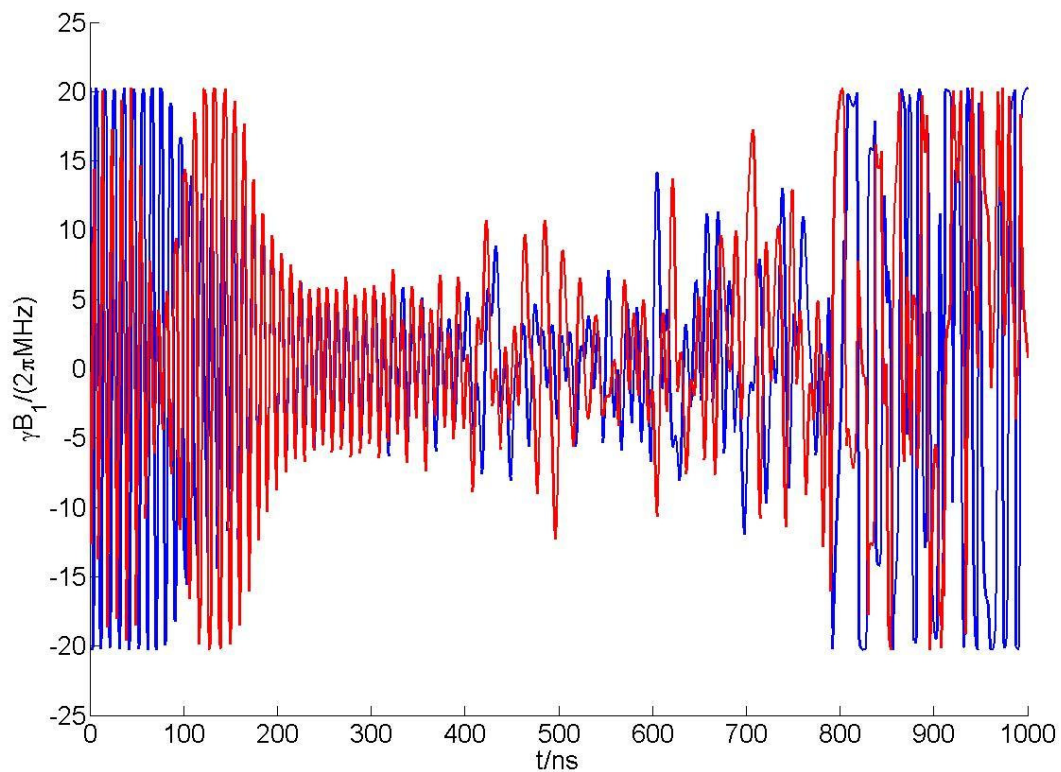


Figure 33 200 MHz prefocused pulse which focuses the transverse magnetization 200 ns after the end of the pulse. Both phases (x:blue; y: red) are shown.

The following paragraph is taken from [39] and describes the increase in performance of a prefocused pulse if the spectrometer impulse response is included in the optimization routine. How the impulse response is implemented into the optimization algorithm is described in [39].

The efficiency of the procedure described above was tested with the flouranthenyl sample for offsets ranging from - 40 MHz to + 40 MHz. Figure 34 shows the comparison between a Hahn-echo sequence with rectangular pulses (first column), the prefocused pulse sequence (second column) and the pre-compensated refocused pulse sequence which takes the impulse response function (Figure 30) into account during optimization (third column).

In the first row of Figure 34, the x-component (in blue) and the y-component (in red) of the input pulse are depicted. The second row shows the simulated output pulse, as modified by the response function. The calculated x-magnetization 200 ns after the pulse is shown in the third row of Fig. 9. The grey line shows the performance of an input pulse from the first row, assuming it is delivered with ideal fidelity by the instrumentation. The black line rEPresents

the performance of the actual output pulse delivered to the sample. As illustrated in Figure 34c', the almost ideal performance (grey) of the faithfully delivered input pulse is severely distorted (black) by these hardware limitations. When this anticipated distortion is quantified by measuring the input response function, it can be designed into the pulse presented in the third column. Now, the performance (grey, Figure 34c'') of this input pulse from row one, assumed to be unaffected by the instrumentation, is severely degraded compared to the desired performance, but the performance (black) of the actual output pulse from row two approaches the ideal. In the last row, the performance of the actual output pulse plotted in black in row three is multiplied by the measured frequency response of the video amplifier and again plotted in black. This simulates the frequency profile of the measured signal, including instrumental effects, resulting from application of the pulses in row two. Experimental cosine Fourier-transformed FID signals of the flouranthenyl sample are plotted as grey lines in the last row of Figure 34 for both prefocused pulses. There is excellent agreement between the theoretical and experimental performance of the pulses.

Although the hard pulses in column one are relatively unaffected by these instrumental effects, they perform over a very limited bandwidth which can be significantly extended using the shaped OCT pulse in column three. The comparison was made with the same B1 amplitude to emphasize that this conclusion and possibility is relevant for a range of EPR applications currently employing hard pulses.[39]

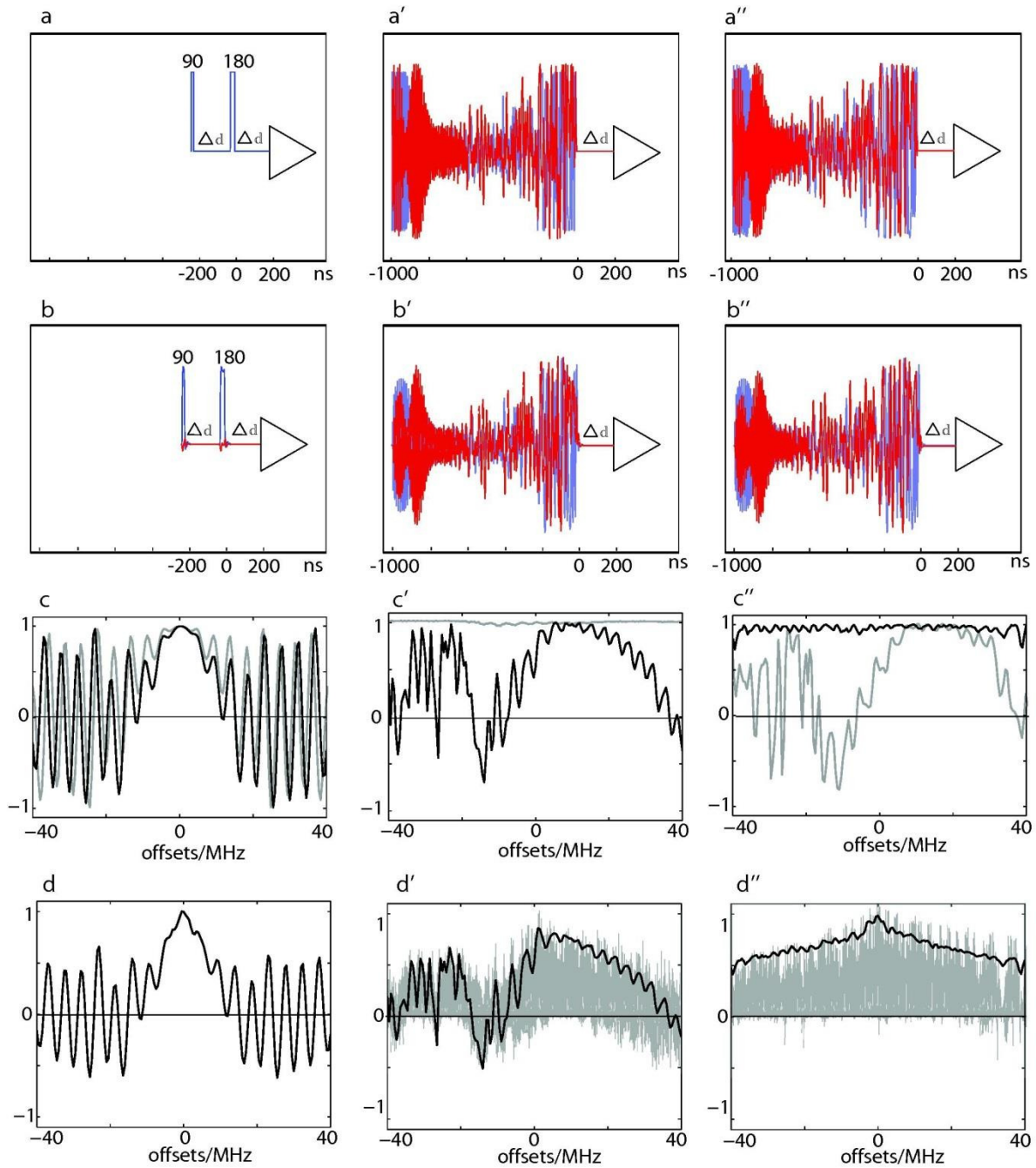


Figure 34 [39] compares conventional and optimized pulses designed to acquire signal 200 ns after the end of the last pulse and their offset profiles. The left column rEPresents a conventional echo sequence based on rectangular 90° and 180° pulses. The middle and right columns rEPresent results of optimizations without (middle column) and with (right column) transient effects taken into account in the optimization. The panels in the first (a) and second (b) row show x- (red) and y-(blue) component of simulated input and output pulses, respectively. The third row (c) shows the simulated response for the input pulse (grey curves) and for the output pulse (black curves). Finally, the black curves in the fourth row (d, d', d'') rEPresent the simulated response of the output pulses multiplied by the measured frequency response of the video amplifier. In panels d' and d'', experimental spectra are shown as grey curves.

6.1.5 Prefocussed pulse in the presence of anisotropic hyperfine interaction

Prefocussed pulses are useful for inhomogeneously broadened radicals where a fid cannot be detected.. The couplings are often anisotropic which leads to additional artifacts in the excitation pattern as discussed in the following.

The prefocused pulse was applied on a sample consisting of BDPA immobilized in polystyrene at 298 K. The 10 GHz MD 5 resonator was used. The Fourier transform of the signal beginning $t=200$ ns (Figure 35) is shown in Figure 36. The comparison with a reference cw-signal shows that the signal is modulated in the frequency domain. The prefocused pulse was optimized assuming an uncoupled spin which is not valid for immobilized BDPA where anisotropic hyperfine interactions with protons are present.

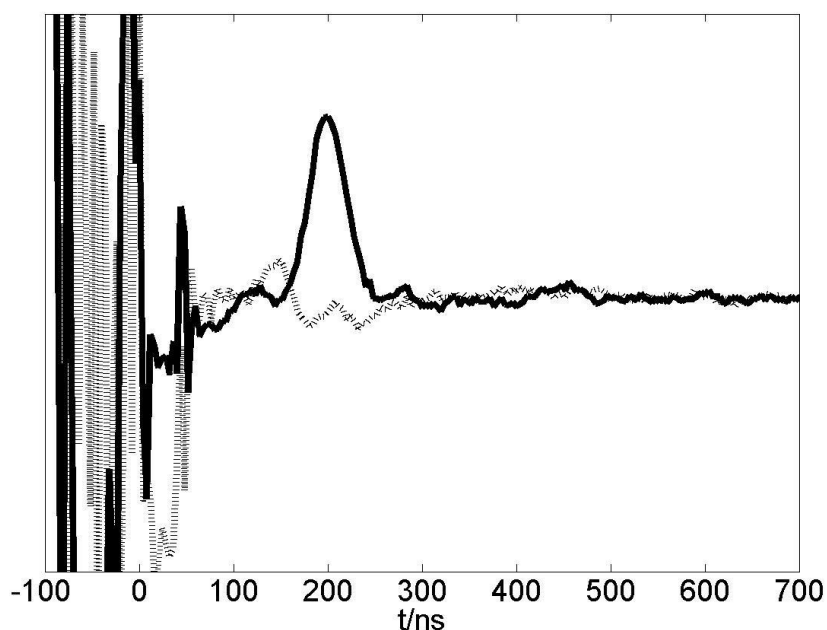


Figure 35 [39] BDPA-echo generated with the prefocused pulse shown in Figure 33. The time when the all magnetization is aligned is 200ns after the end of the pulse.

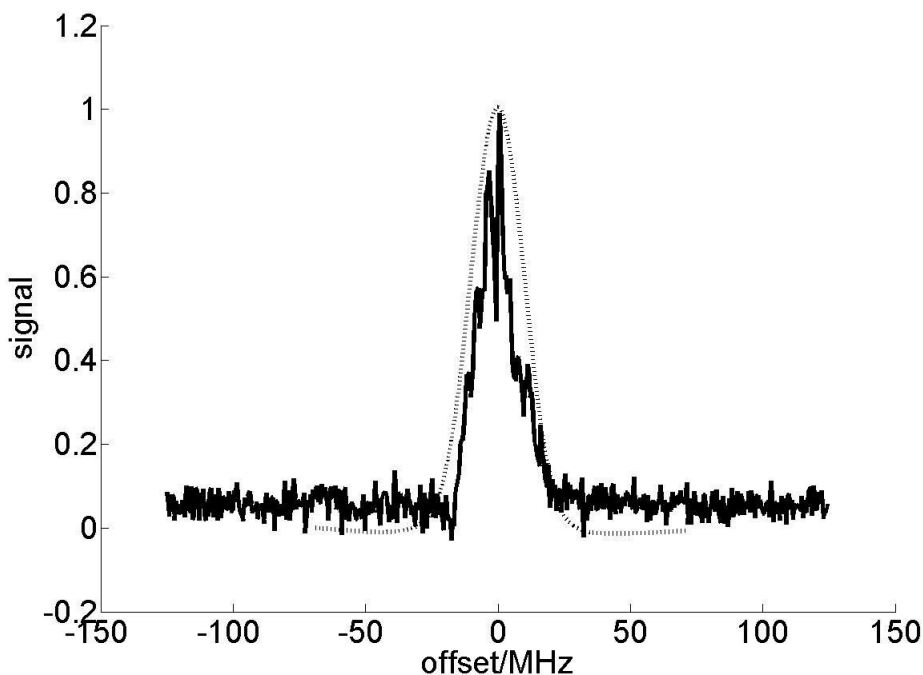


Figure 36 cos-Fourier transform of the BDPA FID generated with a 200 MHz prefocused pulse in comparison to a cw-reference (dashed).

The behavior of a spin system consisting of an electron spin and one proton with anisotropic hyperfine coupling was simulated once with a 1 ns 90° pulse and the 200 MHz optimum control prefocused pulse. The spin system is described by the electron g-tensor which was set to $g_{xx}= 2.0088$; $g_{yy}= 2.0065$, $g_{zz}=2.0027$ and the hyperfine coupling tensor which was set to $A_{xx}= 0$ G; $A_{yy}= 0$ G; $A_{zz}= 5$ G. The equilibrium density matrix was propagated in 1 ns time steps. To simulate a powder spectrum 1000 orientations have been superimposed.

The Fids are shown in Figure 37 (1 ns 90° pulse) and Figure 38 (prefocused pulse). For both simulations the density matrix was propagated for 1000 ns further the time the magnetization focuses to give an equal observation window. The cosine Fourier transformations of the fids are shown in Figure 39. The prefocused pulse shows dips in excitation efficiency compared to the 1 ns 90° hard pulse reference. The simulation shows that anisotropic hyperfine interaction causes artifacts in the excitation pattern of the prefocused pulse with a bandwidth by far exceeding the spectral width. The artifacts are not visible in simulations which are based on the Bloch equations where no anisotropic hyperfine coupling is present.

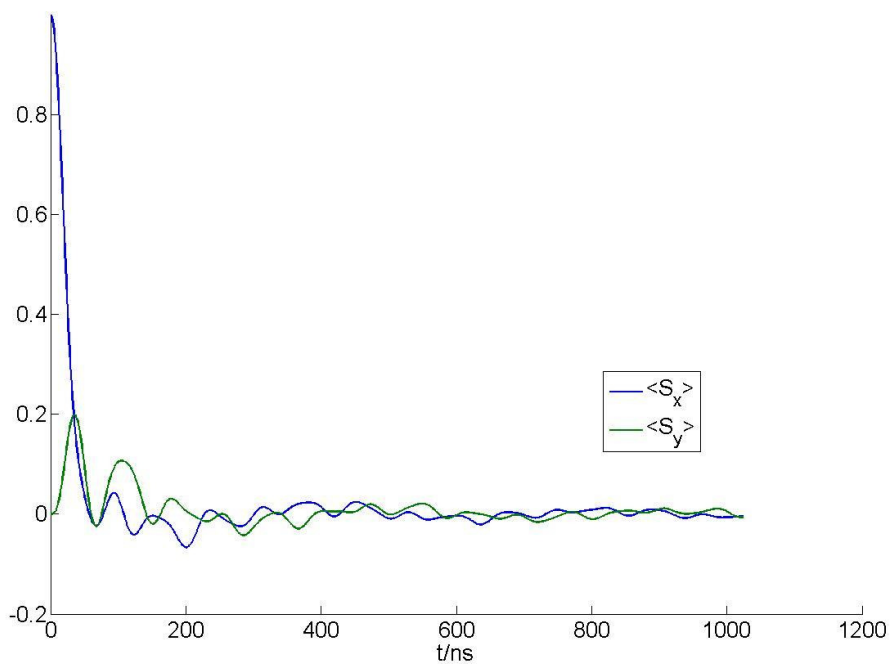


Figure 37 simulated FID of the electron proton spin system excited with a 1 ns 90° pulse.

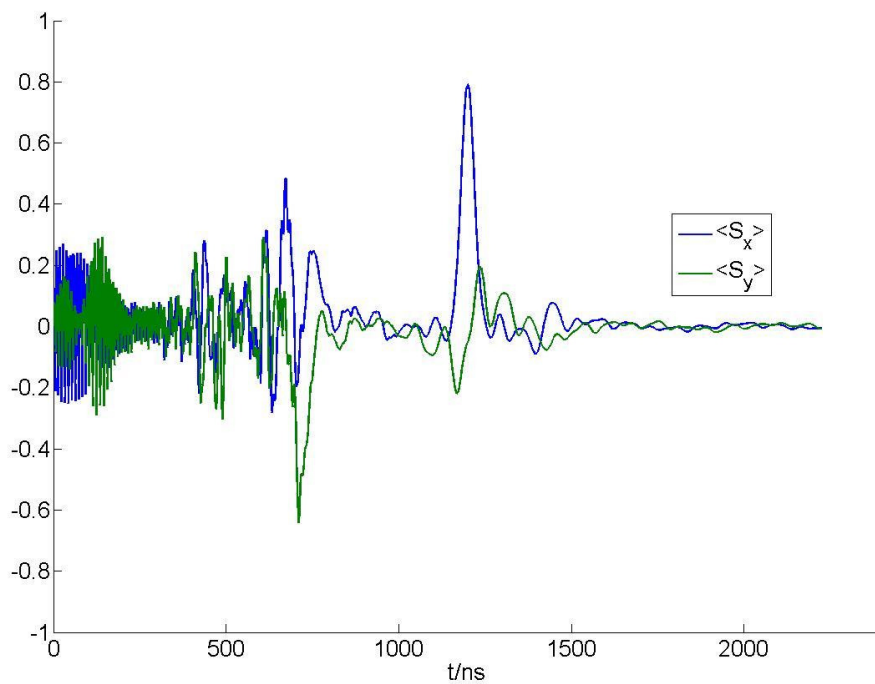


Figure 38 simulated FID of the electron proton spin system excited with a 1000 ns prefocused pulse. The maximum of the echo appears at $t = 1200$ ns which is the pulse length plus the delay time of 200 ns.

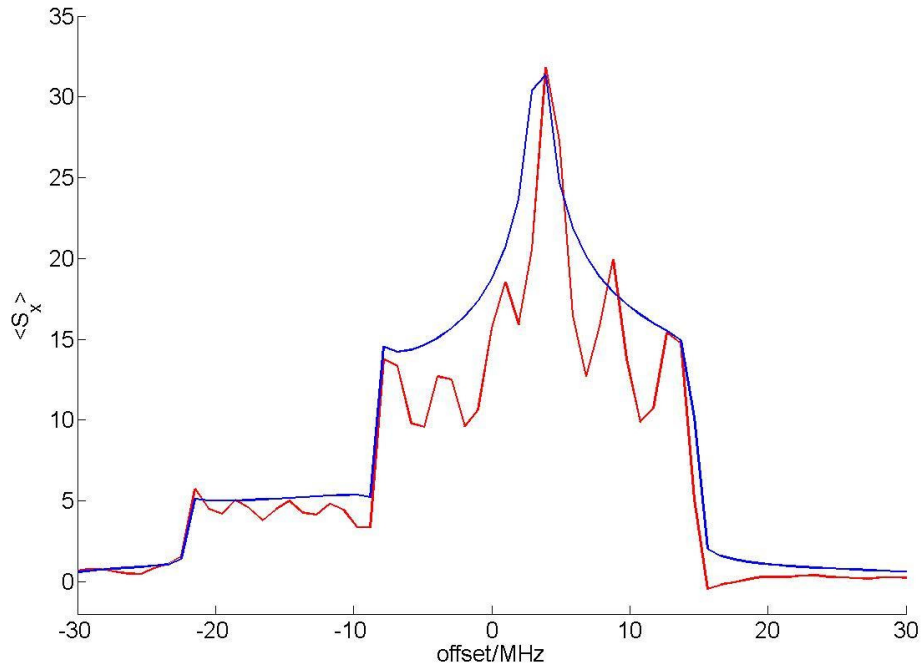


Figure 39 Cosine Fourier transforms of simulated fids for an IS spin system with anisotropic hyperfine coupling once excited by an 1ns 90° pulse (blue) and with a 200 MHz prefocused pulse (red).

To investigate if the presence of anisotropic hyperfine coupling becomes negligible for higher static fields \vec{B}_0 where the nuclear Zeeman splitting exceeds the anisotropic hyperfine interaction a \vec{B}_0 field series on an artificial electron-proton system was simulated for static fields between 0.05 T and 4.9 T. An isotropic g-tensor was assumed. The Hyperfine interaction tensor was set to $A_{xx}= 0$ G; $A_{yy}= 0$ G; $A_{zz}= 10$ G. For the simulations 300 orientations have been superimposed to create a powder pattern. The density matrix was propagated and the FIDs have been Fourier transformed to obtain the spectra. The result is shown in Figure 40 where the blue spectra are obtained by using a 1 ns 90° pulse for excitation whereas the red spectra are generated by the 200 MHz prefocused pulse shown in Figure 33. For both simulations a 1000 ns FID was generated. A superficial analysis reveals two reasons for the observed distortions in the excitation pattern. For static fields where the nuclear Zeeman interaction is comparable to the strength of the anisotropic hyperfine interaction forbidden transitions are driven [41, 42] thus the microwave pulses excite the electron spin and the nuclear spin simultaneous. These phenomena are thus related to the well-known ESEEM effects in pulsed EPR and should disappear for higher static fields. Some distortions in Figure 40 become field independent towards higher fields revealing that just the presence of the hyperfine field of the nucleus on the electron causes artifacts in the excitation profile which are then not caused by driving forbidden transitions.

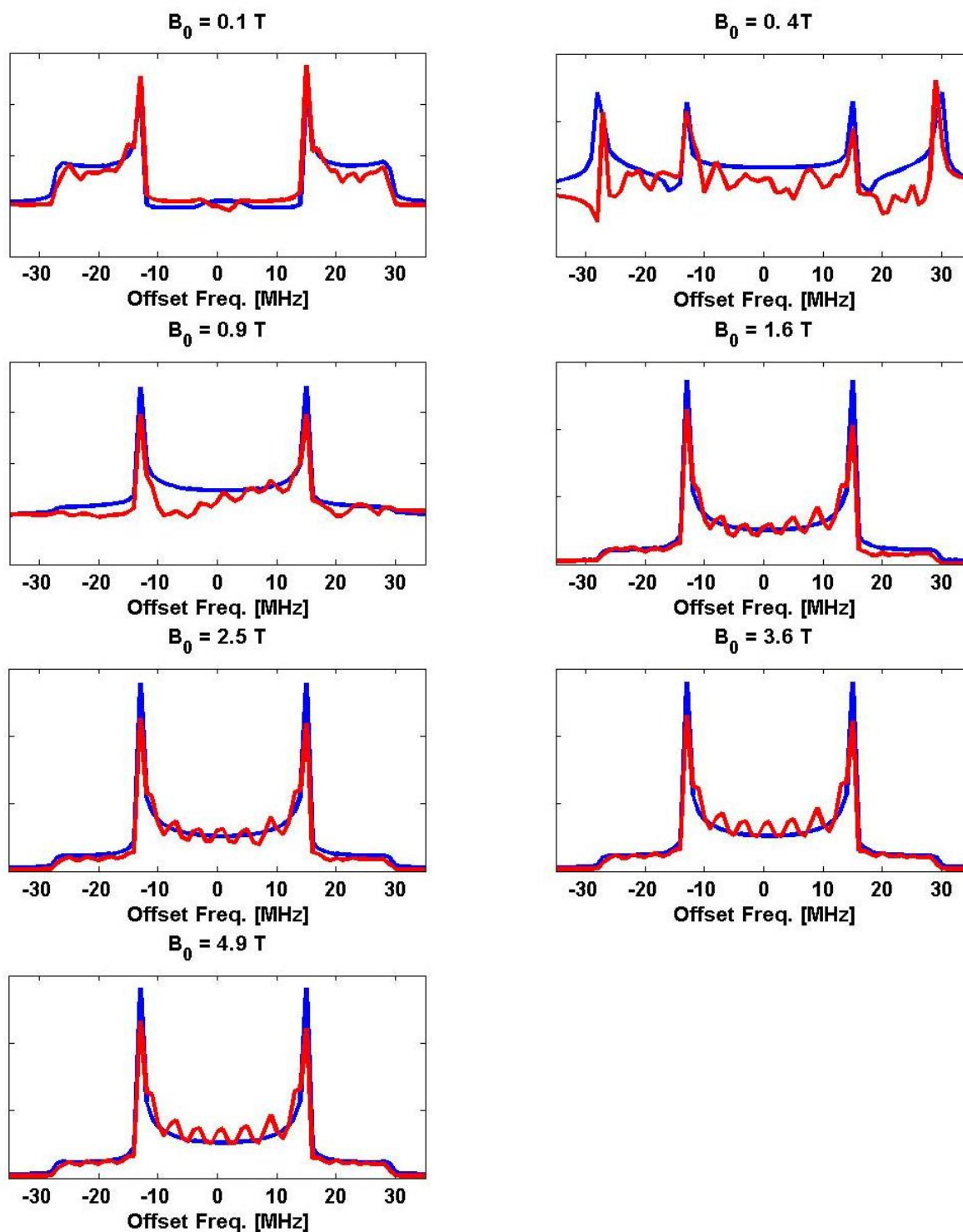


Figure 40 \vec{B}_0 -field series of an $I=1/2$ $S=1/2$ system with an isotropic g -tensor and an anisotropic hyperfine tensor $A_{xx}=0$ G; $A_{yy}=0$ G; $A_{zz}=20$ G. Shown is the Fourier transform of the simulated FIDs for different static magnetic fields. The blue spectra are obtained with an 1ns 90° excitation pulse whereas the red spectra are generated with a 200 MHz prefocused optimum control pulse. The optimum control pulse was optimized assuming only isotropic Zeeman interaction.

6.2 Broadband Inversion PELDOR Spectroscopy

6.2.1 Requirements on Shaped Pulses as PELDOR Pump Pulses

The S/N of a PELDOR experiment is proportional to the modulation depth λ . In almost all cases where PELDOR spectroscopy is applied, the bandwidth of the pump pulse does not cover the spectral width of the B-spins. For a nonrigid biradical bearing two nitroxide spins a modulation depth of 0.5-0.6 can be achieved at X-band frequencies with a 1 kW TWT amplifier. At Q-band frequencies the modulation depth obtained with a 10 W amplifier is only 0.3. The situation gets worse if the B-spins are broadband transition metals. Examples known in literature cover PEDLOR on copper complexes[43-45], iron sulfur centers [46, 47], gadolinium complexes[48-50] and manganese ions[51, 52]. The obtained modulation depth in all of these cases does not exceed a few percent.

In the following chapter the successful application of partially adiabatic pulses as pump pulses for PELDOR spectroscopy is reported.

A pump pulse for PELDOR spectroscopy has the simple task to invert the population of the B-spin ensemble at a certain time. The time of inversion should be the same for all B-spins independent of their individual resonance frequency, thus ensuring that the time zero of the dipolar evolution is equal for all radical pairs. Shaped pulses generally cannot act on all spins within a target bandwidth at once but manipulate different frequencies at varying instants of time. The effect is that the signal recorded is a superposition of sub-ensembles which in first approximation have the same dipolar coupling but different time zeros. This spread in time zero for different sub-ensembles might lead to an additional damping of the dipolar oscillation in the time-domain. In a first attempt the length of the inversion pulse is kept short relative to the inverse of the dipolar coupling frequency.

The effect on the maximum dipolar evolution time of replacing the rectangular shaped pump pulse by a prolonged broadband pump pulse is not negligible as explained in the following.

The max dipolar evolution time T_{\max} for the 4-pulse sequence[23] is the time between the first echo and the second refocusing pulse reduced by the length of the pump pulse T_{pump} to avoid any temporal overlap between A- and B-pulses (see Figure 41).

If the length of the shaped pump pulse also exceeds the first tau-period τ_1 of the refocused echo the time zero of the dipolar evolution cannot be detected. Therefore a sequence with a

larger τ_1 has to be used which also effectively reduces the dipolar evolution time T_{\max} since the second tau period τ_2 has to be decreased to achieve the same echo intensity.

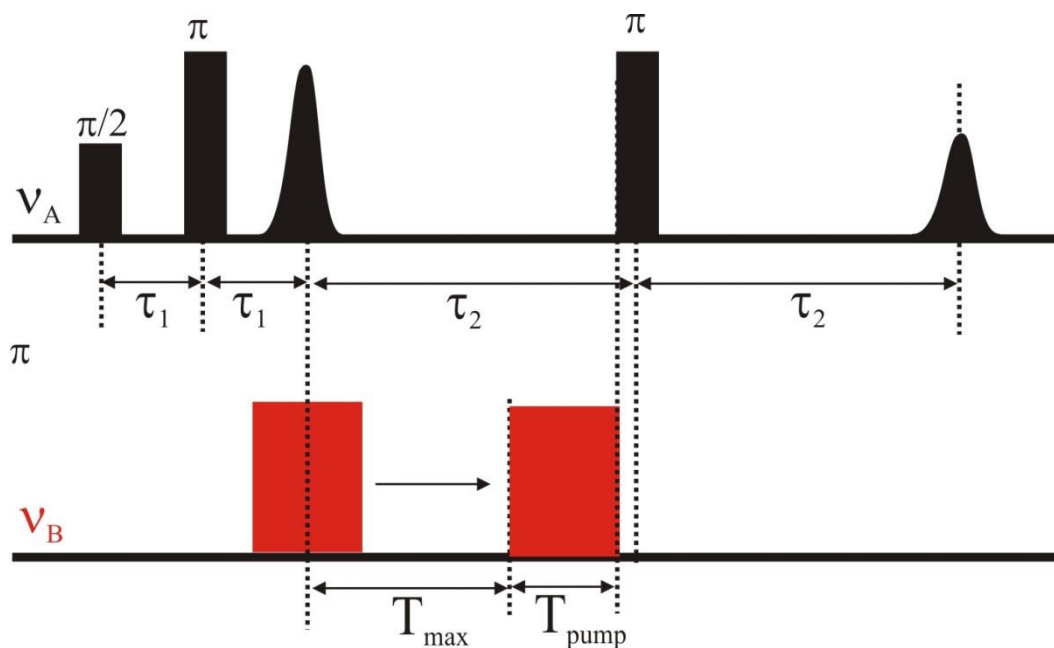


Figure 41 4-pulse PELDOR sequence. The shaped pump pulse is sketched as red boxes with a length T_{pump} . The two boxes represent the position of the pulse at the beginning and at the end of the PELDOR timetrace. The maximum dipolar evolution time is: $T_{\max} = \tau_2 - T_{\text{pump}} - \frac{L_{\pi A}}{2}$ with $L_{\pi A}$ being the length of the A-spin refocusing pulse.

Another crucial requirement on the shaped pump pulse is a well-defined transition from pass to stop band to ensure that the refocused echo is not disturbed by a spectrally overlapping pump-pulse.

All the above mentioned requirements were met to a certain degree by the in NMR familiar adiabatic sech/tanh inversion pulse. Nonetheless the pulse parameters recommended in the existing literature would have led to a too long pulse severely reducing the dipolar evolution time T_{\max} . Hence, major changes to the well-known parameters have been made as explained in the following.

6.2.2 The modified sech/tanh PELDOR pump-pulse

In order to keep the reduction of T_{\max} by a prolonged pump-pulse on a reasonable level the maximum length of the shaped pump pulse was restricted to 200 ns at first. The maximum B_1 field strength in frequency units was limited to 25 MHz. Prof Thomas Skinner from Wright State University optimized a sech/tanh pulse to the given restrictions by trial and error. The resulting sech/tanh pulse which is shown in Figure 42 has a more than three times larger inversion bandwidth than the 20 ns rectangular pulse utilizing the same peak B_1 field. To keep the pulse length short a severe truncation was conducted as shown in Figure 42. Sech/tanh pulses used in NMR are typically cut off at 1% of the peak amplitude by choosing $\beta=10.6/T$ (see equation (35) and (36)). Whereas in this case the initial/final amplitude is more than 25% of the max amplitude. The effect is seen in Figure 43 as minor drops in the inversion efficiency within the pass-band The complete pulse parameters(chapter 4.3.2) are : $\beta=4/T$; $T = 200$ ns ; $BW = 2\pi 90$ MHz ; $B_{1\max} = 8.9$ G .

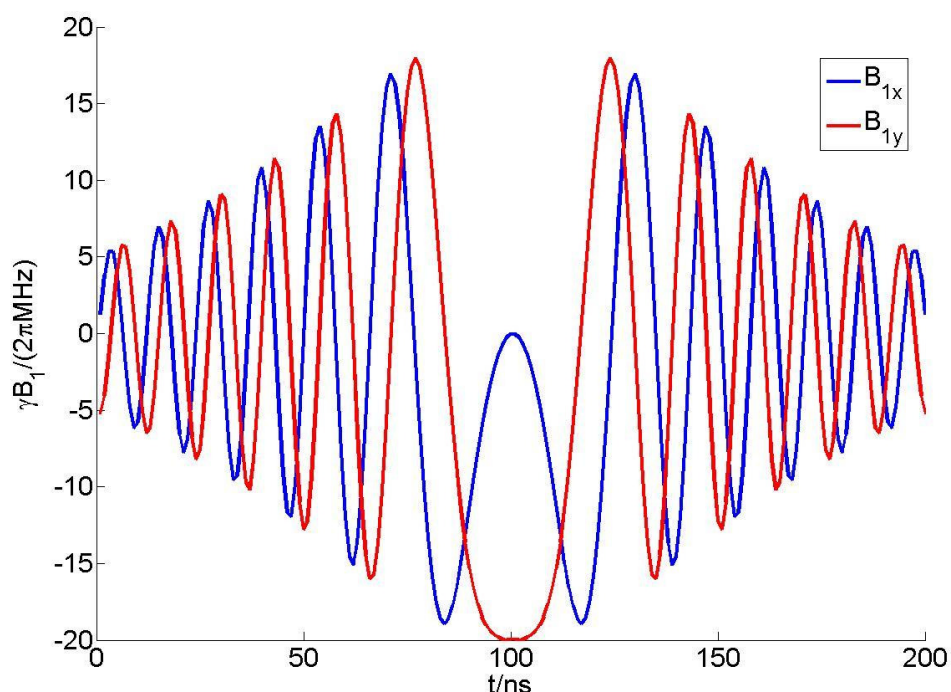


Figure 42 [53] Truncated sech/tanh inversion pulse used as a pump pulse for PELDOR spectroscopy. X-component (black) and Y-component(grey) are depicted.

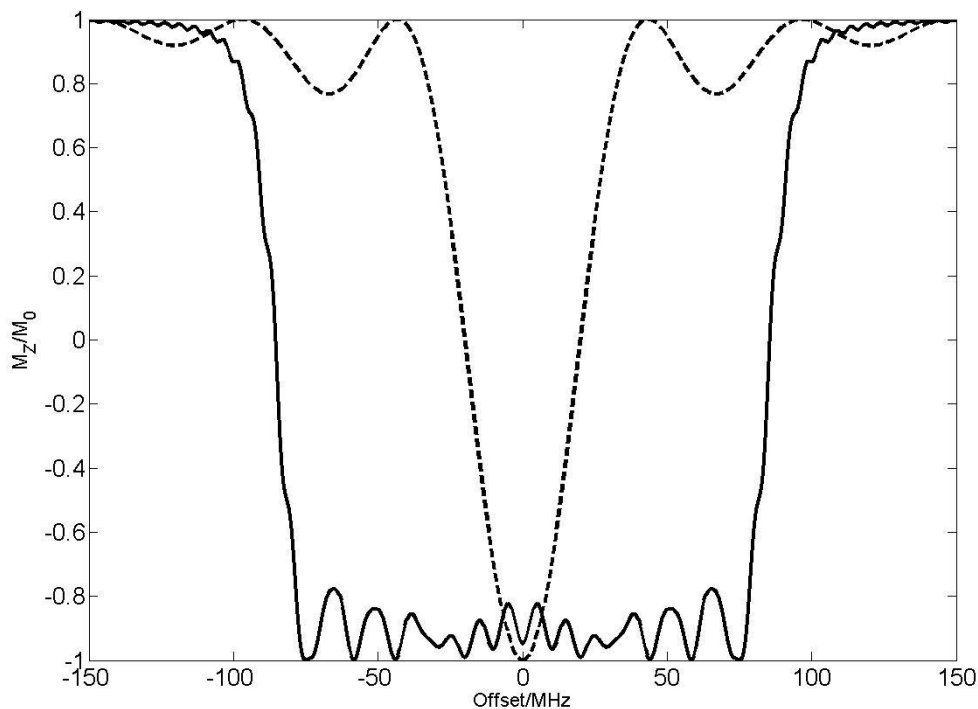


Figure 43 [53] Inversion profile of the 200 ns sech/tanh pump pulse (black) compared to a 20 ns rectangular shaped inversion pulse using the same peak B_1 -field of 8.9 G.

6.2.2 Broadband inversion PELDOR on a Bisnitroxide - and Cobalt(II)-porphyrin-Nitroxide-biradical

The following experiments have been carried out on a Bruker E580 pulse spectrometer operating at X-band frequencies. The biradical which was chosen to test the new pump pulse bears two nitroxides connected by a rigid linker. The structure of it is shown as inlet in Figure 44. The most probable distance between the two nitroxides is 3.4 nm which gives a perpendicular dipolar coupling frequency of 1.3 MHz corresponding to a oscillation period of 758 ns which is approximately four times the length of the sech/tanh pump-pulse introduced in the previous chapter. The sample was immobilized in o-terpheny which enabled to measure at room temperature. It was located in a 4 mm quartz tube and filled the whole active volume of a Bruker MD5 resonator which was fully overcoupled to give maximum bandwidth. The pump frequency was matched to the resonance frequency of the resonator. Two timetraces have been recorded under the same experimental conditions despite the pump probe offset. An offset of 70 MHz was chosen for the rectangular pump pulse to ensure that the maximum inversion efficiency coincides with max of the nitroxide spectrum. The pump probe offset for

the sech/tanh pump pulse had to be set to 112 MHz (see Figure 45) to keep the signal loss on the refocused echo within a tolerable level. The effect of off-resonant pump-pulses is discussed here[54]. The comparison of these experiments is depicted in Figure 44 and shows the significant increase in modulation depth obtained with the shaped pump pulse. The modulation depth was increased by a factor of 2.5 which is less than the increase in inversion bandwidth, but could be explained if the actual shape of the nitroxide spectrum is considered.

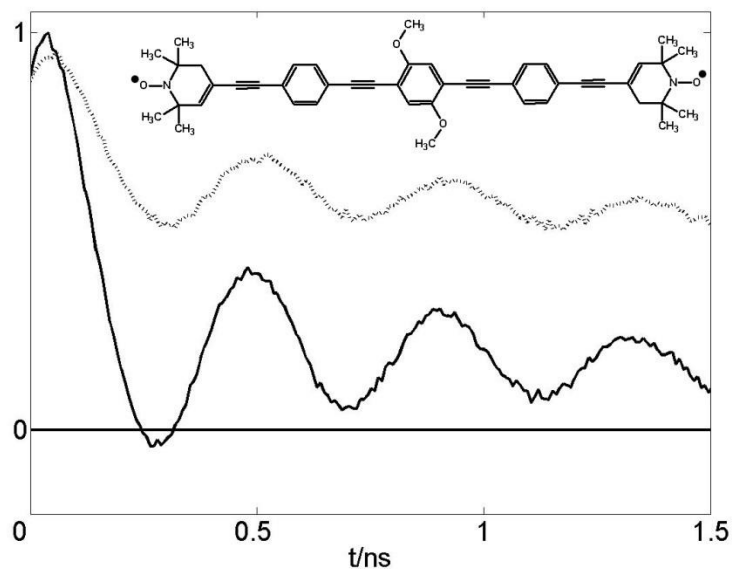


Figure 44 [53] PELDOR timetrace of the biradical shown as inlet. The 200 ns sech/tanh pump pulse (solid) achieves a 2.5 times higher modulation depth than the 20 ns rectangular pump pulse (dotted).

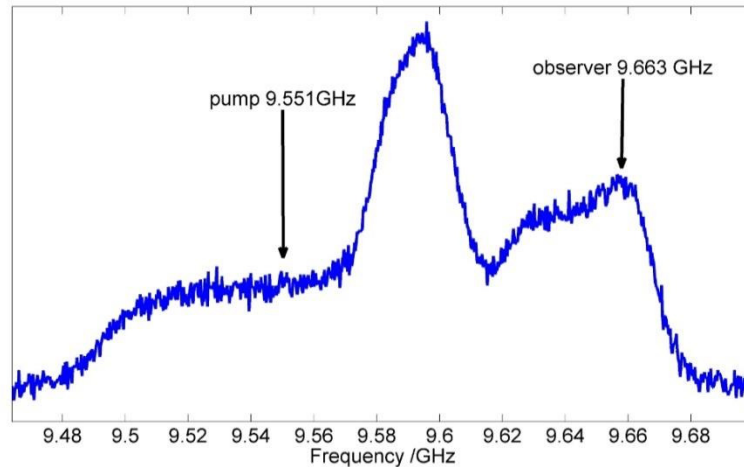


Figure 45 [53] Pump and probe position of in case of the sech/tanh pump pulse.

The analysis of the broadband PELDOR experiment done with Deer Analysis[55] reveals that even though the distance distributions coincide, a slight signal rounding in the time domain took place. If the distribution of dipolar frequencies (middle column of Figure 46) is compared a decrease towards higher frequencies is observable. Higher frequencies are of course more prone to signal rounding which played less of a role for this experiment since the dominating singularities of the Pake pattern are well resolved in case of the shaped pump pulse.

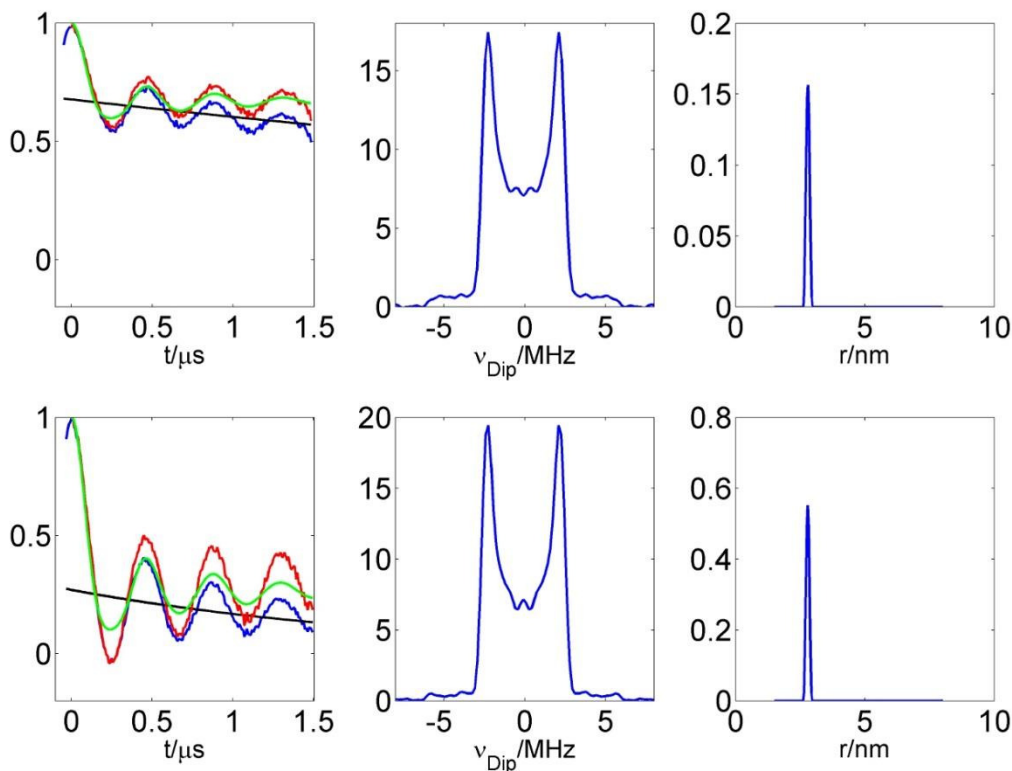


Figure 46 [51] Distance analysis of the nitroxide biradical obtained with DeerAnalysis[55]

Top ,left: Timetrace obtained with the 20ns rectangular pump pulse (blue); Background (black) ; Background corrected timetrace (red); Fit using Tikhonov regularization with regularization parameter 0.001 (green)

Top, middle : Fourier transform of the background corrected timetrace

Top, right: Distance distribution from Tikhonov regularization with a regularization parameter of 0.001

Bottom ,left: Timetrace obtained with the 200ns sech/tanh pump pulse (blue); Background (black) ; Background corrected timetrace (red); Fit using Tikhonov regularization with regularization parameter 1 (green)

Bottom, middle : Fourier transform of the background corrected timetrace

Bottom, right: Distance distribution from Tikhonov regularization with a regularization parameter of 0.001 [53]

The 150 MHz pump pulse was applied to a biradical which consists of a nitroxide and a spin- $\frac{1}{2}$ Co^{2+} ion. The structure of the biradical is shown as inset in Figure 47 with the two axial pyridine ligands missing. The Co^{2+} ion spans a spectral width of approximately 1.5 GHz which makes it an ideal test sample for broadband pump pulses. The PELDOR experiments have been carried out at X-band frequencies at 25 K. The sample was located in a 4 mm quartz tube and filled the full active volume of the fully overcoupled MD 5 resonator. The

pump probe positions shown in Figure 47 are in this case the same for both, the rectangular pump pulse as well as the sech/tanh pump pulse.

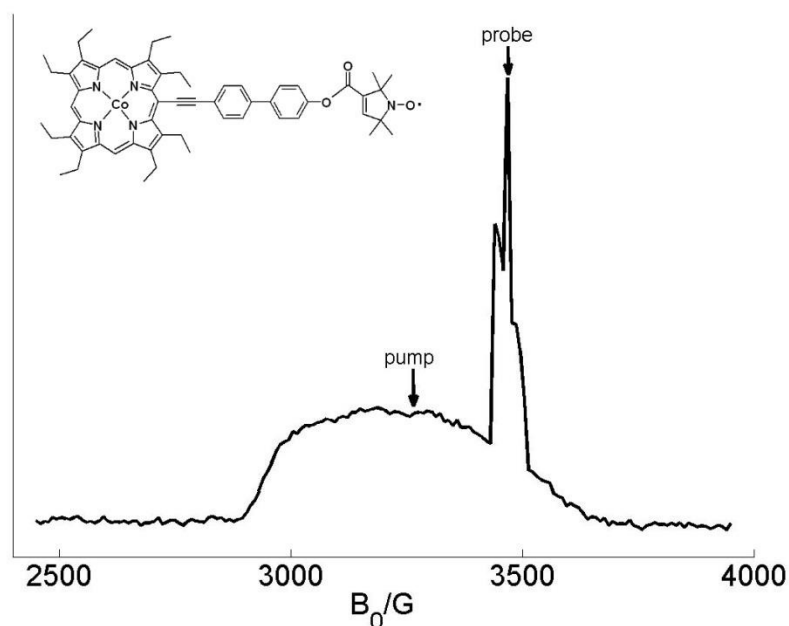


Figure 47 [53] Echo detected field sweep spectrum of the Co-NO biradical shown. The shot repetition time was set to 0.5 ms to partially saturate the nitroxide. The pump –probe positions for the PELDOR experiments performed on this system are approximate 600 MHz apart.

Pumping on the Co spin while observing the slowly relaxing nitroxide increases the shot repetition time and is therefore not the optimal way to perform a PELDOR experiment on this kind of system. It, however, is appropriate since only the gain in modulation depth in combination with the fidelity of the timetrace is of interest here. Also in this case a fully overcoupled MD 5 resonator was used to achieve the maximum possible bandwidth. The detection frequency was set to 9.113 GHz, 600 MHz lower than the pump frequency of 9.679 GHz which is far out of the bandwidth of the MD 5 resonator. Nonetheless a sufficient echo signal was detected. Also for this sample a comparison of the rectangular pulse with the 150 MHz sech/tanh pump pulse was made. The outcome is shown in Figure 48. The modulation depth increased from 0.021 for the rectangular pulse to 0.056 for the sech/tanh pump pulse which is a factor of 2.66, considerably less than expected due to the quasi uniform absorption profile of the Co ion. If one inspects the dipolar frequency spectrum obtained with the 200 ns sech/tanh pulse a rapid damping towards higher frequencies is visible when compared to the one obtained with the 20 ns rectangular pulse. Also the distance distribution is shifted towards larger distances and broadened when compared to the rectangular counterpart. The shift in distance is introduced by the shift of the singularities of the Pake pattern for the shaped pump

pulse (see Figure 48). The reason for these artifacts and their elimination by a new pulse sequence will be discussed in the following.

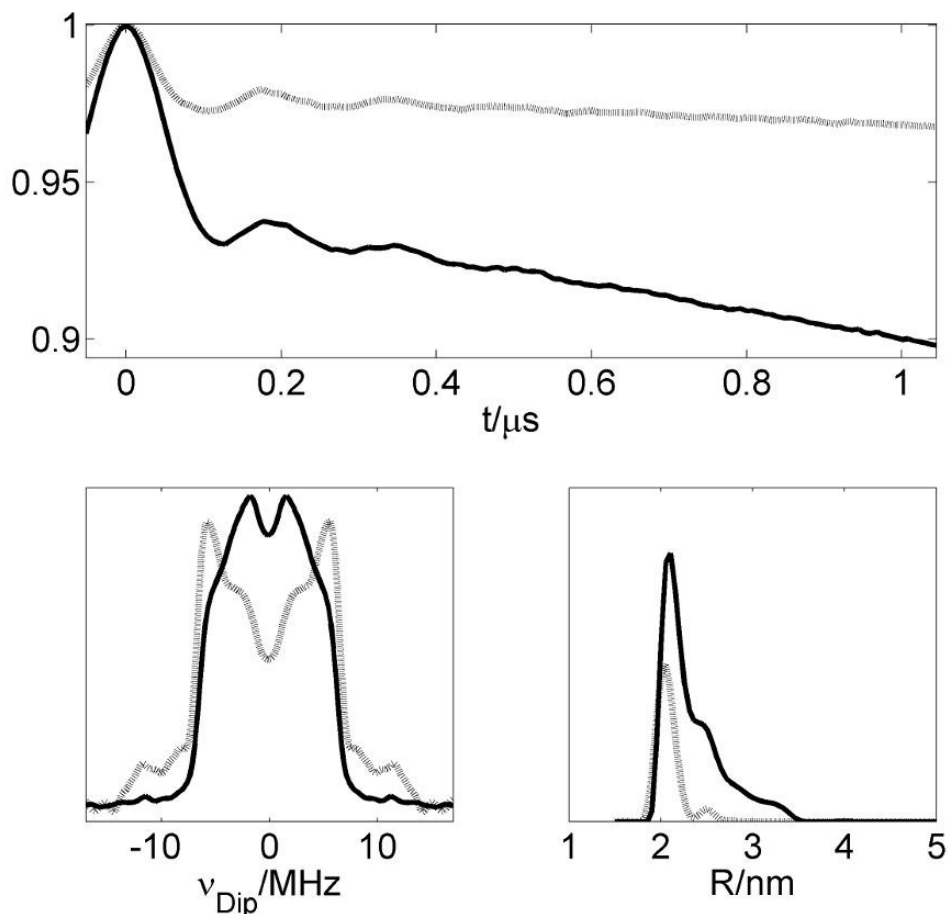


Figure 48 [53] Top: PELDOR timetraces of the Co-NO system (Figure 47) obtained with a 150 MHz sech/tanh pump pulse (solid) and with a 20 ns rectangular pump pulse (dotted). Bottom left : Fourier transform of the dipolar evolution after correction of the intermolecular background. Bottom right: distance distributions obtained with Tikhonov regularization by Deer Analysis[55].

6.2.4 Distortion introduced by the offset dependent zero time

It is useful to examine the time and offset dependent M_z -evolution of the sech/tanh pump-pulse to understand the mechanism of signal rounding in the time domain. Figure 49 shows the frequency offset dependent evolution of the M_z magnetization during the 200 ns sech/tanh pulse. It reveals that the time which is needed to flip an individual spin is comparable to the rectangular pulse, but spins with different resonance frequencies are flipped at unequal times during the pulse. The profile itself follows the frequency modulation which is a tanh-function (Figure 49). What also can be seen in Figure 49 is that the time in which the pulse inverts

most of the spins is shorter than the actual pulse length by almost a factor of 2. This of course reduces the effect for a given pulse length.

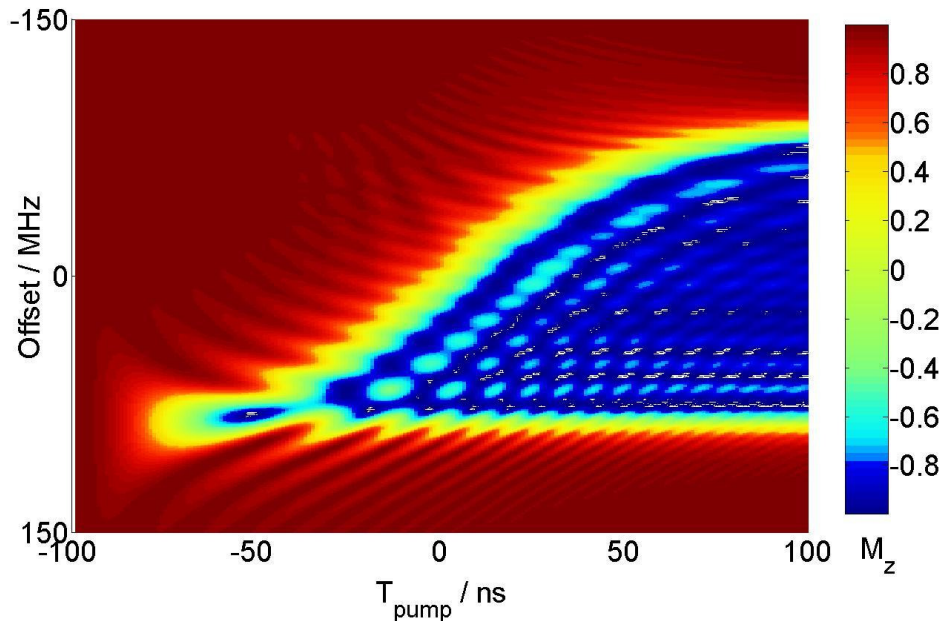


Figure 49 [53] time and offset dependent M_z profile for the 150 MHz sech/tanh inversion pulse.

To simulate the effect of the sech/tanh pump pulse several timetraces with different time-zeros recorded with the 20 ns rectangular pump pulse were summed up and renormalized. The zero points have been equally distributed over a 90 ns time window which was assumed to be the effective inversion time of the 200 ns pulse. The result is shown in Figure 50 with the original timetrace obtained with the rectangular pump pulse for comparison. The perpendicular component of the Pake pattern which cause the prolonged oscillation in the time-domain is washed out and the modulation depth is severely decreased which is due to the washing out of the parallel component of the Pake pattern. The parallel component is more prone to the signal rounding due to its shorter oscillation period. A removal of this distortions by a novel 5-pulse sequence involving two shaped pump-pulses is introduced in the following chapter.

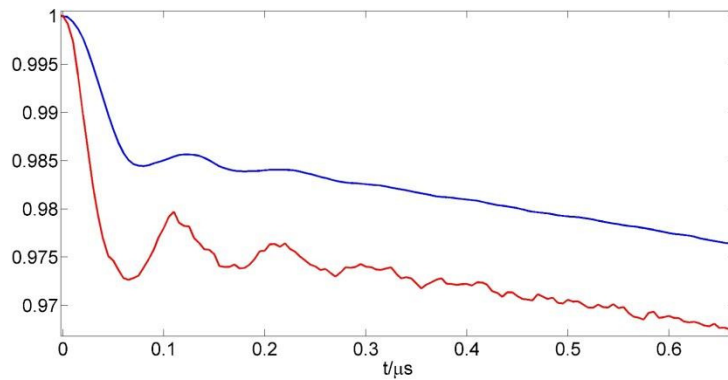


Figure 50 [53] red : PELDOR timetrace recorded with a 20 ns rectangular pump pulse. Blue: renormalized superposition of red timetraces which zero point is time shifted over a 90 ns window.

6.3.3 Offset independent 5-pulse sequence

Since one can assume that the resonance frequency of a B-spin does not change by a significant amount due to instantaneous diffusion during the PELDOR experiment a dipolar refocusing by applying a second time reversed pump pulse right after the refocusing pi-pulse of the A-sequence causes an equal net dipolar evolution time throughout all B-spin offsets. This second pulse is fixed in time during the experiment. The pulse sequence which is shown in Figure 51 contains two sech/tanh pump pulses which are time reversed with respect to each other. This sequence, as will be explained in the following, accomplishes not only an offset independent dipolar evolution time but also prolongs the maximum dipolar evolution time compared to the 4-pulse sequence utilizing the same shaped pump pulse.

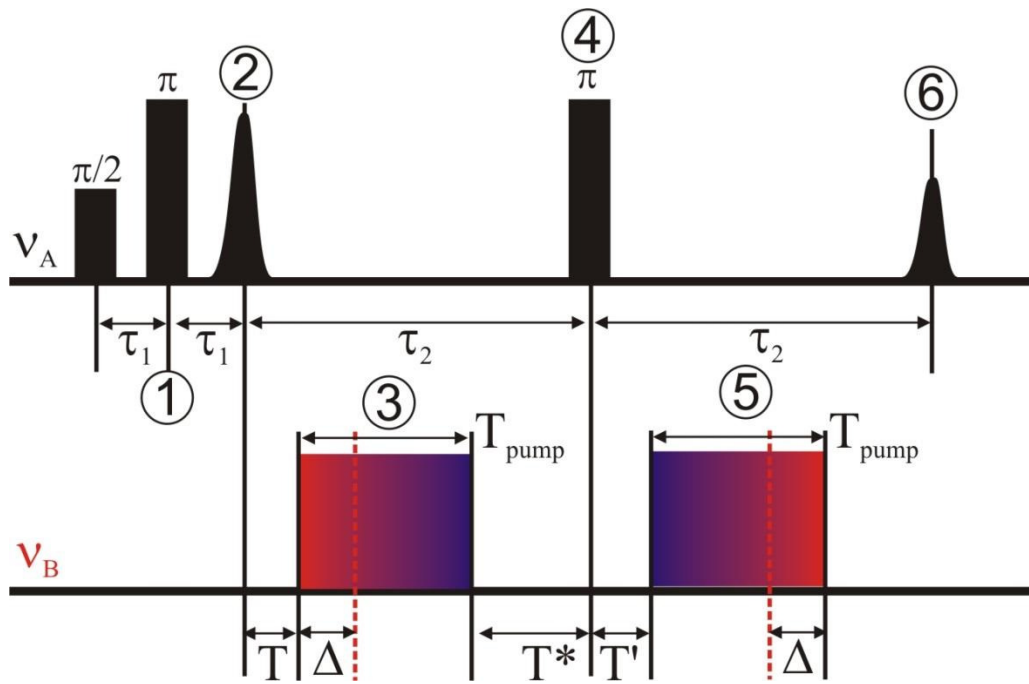


Figure 51 Novel 5-pulse PELDOR sequence for offset independent dipolar evolution time T is incremented during the experiment while T' is fixed.

Let ω_{dip} be the coupling strength between the A and B spin then the dipolar phase for different instances of time according to Figure 51 is:

$$1): -\tau_1 \frac{\omega_{\text{dip}}}{2} \quad (62)$$

$$2): -\tau_1 \frac{\omega_{\text{dip}}}{2} + \tau_1 \frac{\omega_{\text{dip}}}{2} = 0 \quad (63)$$

$$3): (T + \Delta) \frac{\omega_{\text{dip}}}{2} \quad (64)$$

$$4): -((T + \Delta) \frac{\omega_{\text{dip}}}{2} - \frac{\omega_{\text{dip}}}{2} (\tau_2 - \Delta - T)) = \frac{\omega_{\text{dip}}}{2} (\tau_2 - 2\Delta - 2T) \quad (65)$$

$$5): \frac{\omega_{\text{dip}}}{2} (\tau_2 - 2\Delta - 2T) - \frac{\omega_{\text{dip}}}{2} (T' + T_{\text{pump}} - \Delta) = \frac{\omega_{\text{dip}}}{2} (\tau_2 - \Delta - 2T - T' - T_{\text{pump}}) \quad (66)$$

$$\frac{\omega_{\text{dip}}}{2} (\tau_2 - \Delta - 2T - T' - T_{\text{pump}}) + \frac{\omega_{\text{dip}}}{2} (\tau_2 - T_{\text{pump}} + \Delta - T') = \omega_{\text{dip}} (\tau_2 - T' - T_{\text{pump}} - T)$$

$$6): \text{with } T^* = \tau_2 - T_{\text{pump}} - T \quad (67)$$

$$= \omega_{\text{dip}} (T^* - T')$$

According to equation (67) the dipolar evolution becomes independent of Δ which is the instant of time during the pump pulse when the respective spin is flipped. Therefore the dipolar evolution time becomes offset independent. In contrast to the common 4-pulse PELDOR the dipolar evolution has a different time zero which is, when the two pump pulses are symmetrically arranged around the second refocusing pulse. The time T' should be as short as possible to achieve the maximum dipolar evolution time. Remarkable is also that the dipolar evolution time is not limited to the second tau period τ_2 as in the 4-pulse sequence but to $T^*_{\text{max}} = \tau_2 + \tau_1 - T_{\text{pump}}$ (68)

These expressions have been derived neglecting the length of the rectangular pulses. The length of the pump pulses is as important for the 5-pulse sequence as for the 4-pulse sequence since according to equation (68) the max dipolar evolution time is reduced by T_{pump} however $\tau_1 - T'$ is gained.

The time reversed sech/tanh pump pulse is simply generated by inverting the sign of the imaginary part. The frequency sweep is then opposite. The pulse sequence was applied to the Co-NO system shown in Figure 47. The outcome of the measurement is compared with the 4-pulse signal with only one sech/tanh inversion pulse in Figure 52. A few things of this result are noticeable:

- a) The 5-pulse signal is narrower around its time zero
- b) The oscillations arising from the singularities of the Pake pattern are more pronounced;
- c) The modulation depth increased;
- d) An artifact is visible at the end of the timetrace. This artifact is nothing else than a 4-pulse signal which is superimposed on the 5-pulse signal. The 4-pulse signal is generated by B-spins which have been flipped by the first pump pulse but not by the second. For the 5-pulse experiment an inversion profile of the pump pulse would ideally be a box with an infinite steep transition between pass-and stop-band and an inversion efficiency of 1 in the pass band. A look at the inversion profile of the 150 MHz sech/tanh pulse shows dips in the inversion efficiency throughout the passband which result from the truncation. Also the relatively large transition region between pass and stop-band cause an incomplete inversion.

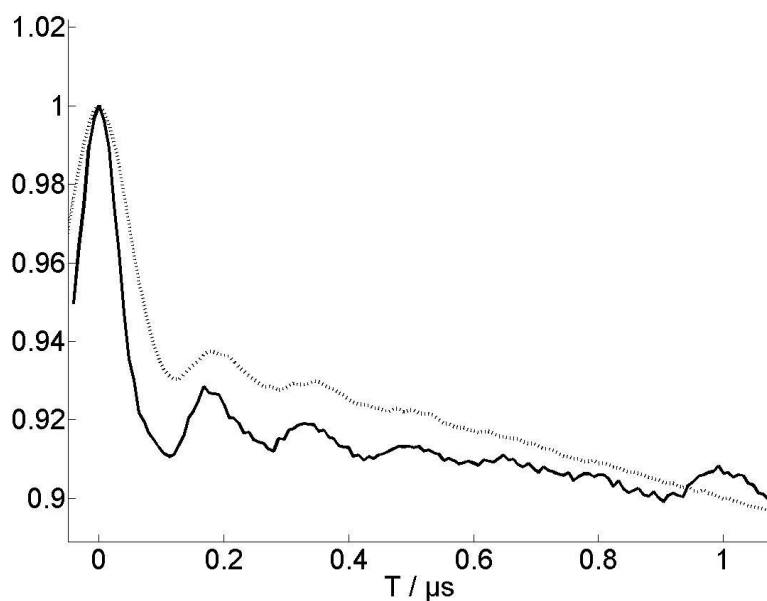


Figure 52 [53] solid: 5-pulse PELDOR measurement on Co-NO system with two 150 MHz sech/tanh pump pulses. Grey: 4-pulse PELDOR measurement with one 150 MHz sech/tanh pump pulse.

To reduce the 4-pulse signal in the 5-pulse sequence a pulse sequence which has a broader bandwidth second pump pulse was applied. The new second time fixed sech/tanh pump pulse was 225 MHz broad with approximately the same sweep rate (see Figure 54) while the incremented first pump pulse stayed the 150 MHz pulse which exclusively had been used previously. The comparison with the 5-pulse sequence utilizing two equal broad pump pulses shows that the 4-pulse signal is reduced to an large extend (see Figure 53). The length of the

second broader bandwidth pulse was increased to 300 ns to achieve a higher bandwidth while maintaining an equal sweep rate for dipolar refocusing. This increase in length corresponds to an increase of T' (see Figure 51).

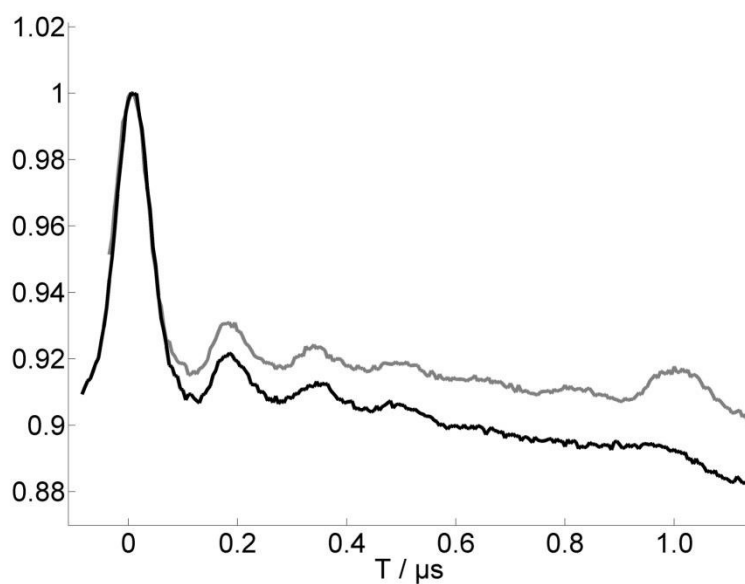


Figure 53[53] Black: 5-pulse Co-NO PELDOR signal obtained with a 150 MHz sech7tanh first pulse and a 225 MHz second pump pulse. Grey: 5-pulse signal obtained with two 150 MHz sech/tanh pump pulses.

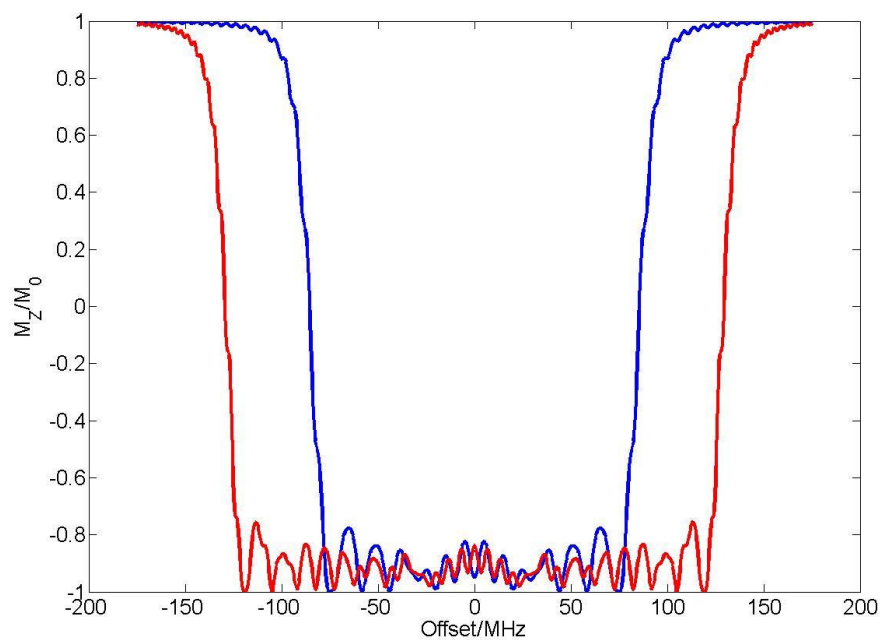


Figure 54 Bandwidth comparison of the sech/tanh pump pulses used for 5-pulse PELDOR. Blue: 150 MHz first pump-pulse; red: 225 MHz fixed second pump-pulse.

The comparison of the broadband 5-pulse PELDOR with the broadband 4-pulse PELDOR which is shown in Figure 55 and Figure 57 shows that the Pake pattern retrieved its undistorted structure seen for the rectangular pump pulse. The 5-pulse sequence shows no loss in signal intensity towards higher frequencies. The modulation depth of the 5-pulse sequence utilizing the 150 MHz and 225 MHz pump pulses was determined to 0.081 which is approximately four times the modulation depth of the 4-pulse sequence with one 20 ns rectangular shaped pump pulse. The 4-pulse sequence with one 150 MHz pump pulse achieved a modulation depth of 0.056. The increase in modulation depth of the 5-pulse sequence is explained by the eliminated signal rounding of the dipolar modulation which effectively reduces the modulation depth which is shown in Figure 50. An increase in modulation depth by a factor of 4 with almost no loss in dipolar evolution time translates directly into an increase in S/N by a factor of 4 and therefore reduces the measurement time by a factor of 16!

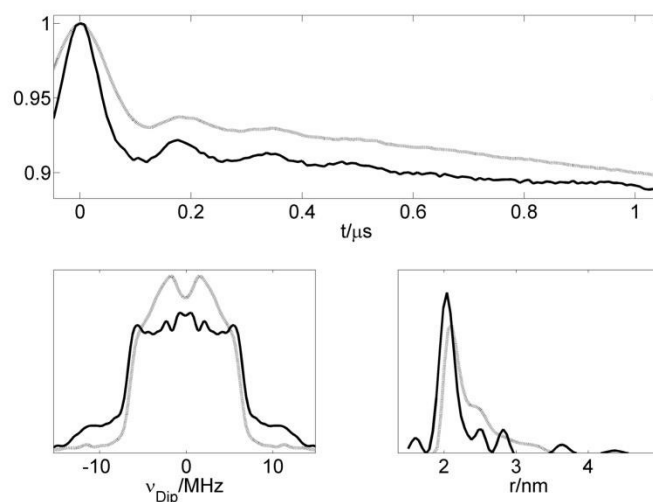


Figure 55 [53] Top: PELDOR timetraces of the Co-nitroxide biradical the normalized PELDOR timetraces recorded with a 20ns rectangular pump pulse (solid) or with the adiabatic pump pulse (dash) are shown. Bottom: The Fourier transformations for both cases as well as the distance distributions[17] are depicted. The less well resolved dipolar Pake pattern for the adiabatic pulse PELDOR (dashed) is clearly visible.

The above obtained results are only possible with the new shaped pulses which generate box shaped inversion profiles instead of the $\sin(x)/x$ shaped profiles produced by rectangular pulses. Figure 56 shows a 5-pulse PELDOR signal recorded under the same conditions as above but with two identical 20 ns 180° pulses as pump pulses. The 4-pulse signal which is almost completely suppressed with the 150 MHz and 225 MHz sech/tanh pump pulses is almost as large as the 5-pulse signal in the case of two 20ns rectangular pump pulses demonstrating their poor inversion efficiency towards off resonant frequencies.

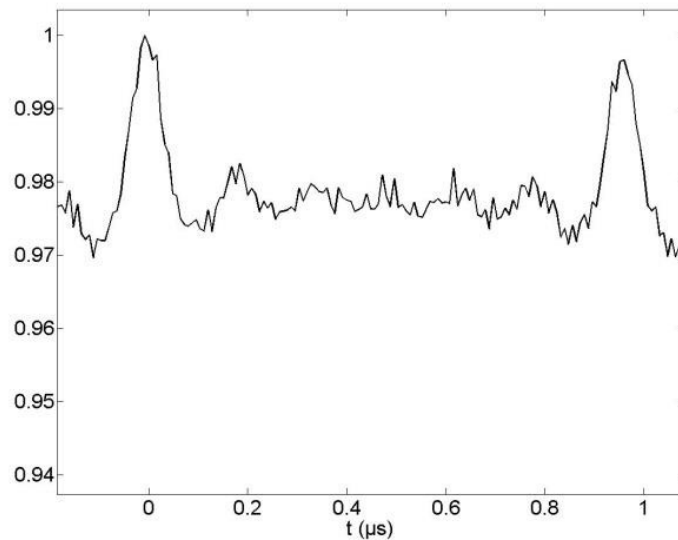


Figure 56 5-pulse PELDOR timetrace on Co-NO biradical obtained with two 20 ns 180° pulses as pump pulses. The time zero of the 5-pulse signal is at $t=1000$ ns.

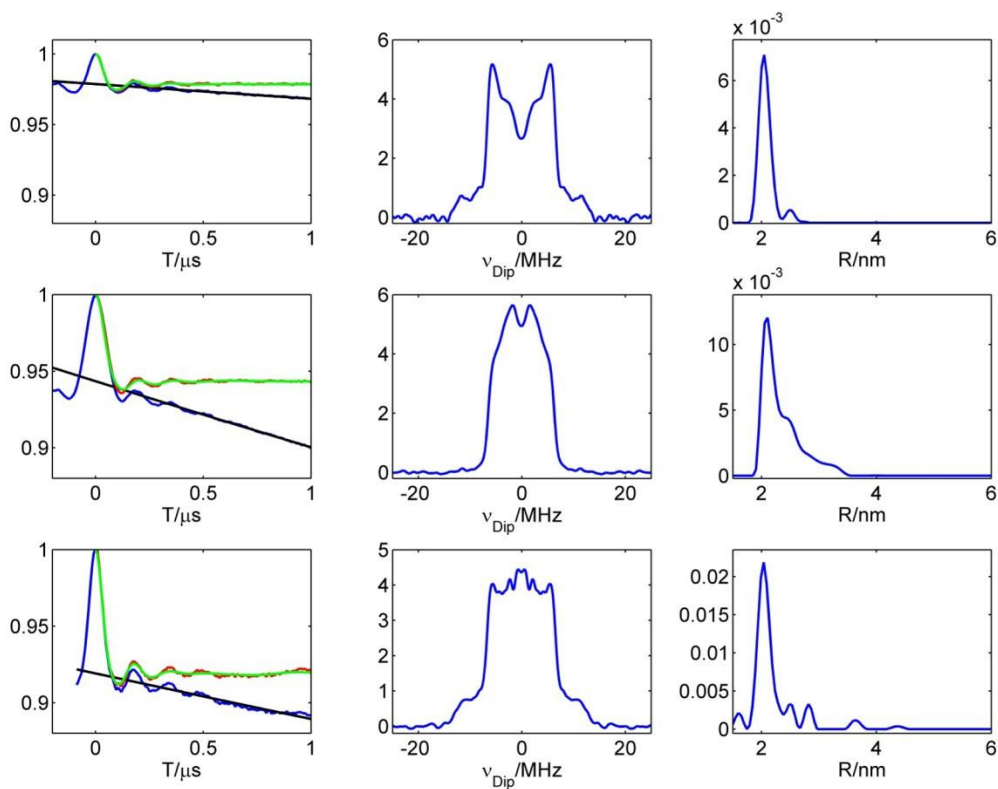


Figure 57 [53] Distance analysis of cobalt nitroxide biradical obtained with DeerAnalysis[55]

Top ,left: Timetrace obtained with the 20ns rectangular pump pulse (blue); Background (black) ; Background corrected timetrace (red); Fit using Tikhonov regularization with a regularization parameter of 1 (green)

Top, middle : Fourier transform of the background corrected timetrace

Top, right: Distance distribution from Tikhonov regularization with a regularization parameter of 1

Middle ,left: Timetrace obtained with the 200ns sech/tanh pump pulse (blue); Background (black) ; Background corrected timetrace (red); Fit using Tikhonov regularization with a regularization parameter of 1 (green)

Middle, middle : Fourier transform of the background corrected timetrace

Middle, right: Distance distribution from Tikhonov regularization with a regularization parameter of 1

Bottom ,left: Timetrace obtained with a 200ns sech/tanh pump pulse and a 300ns 225MHz sech/tanh pump pulse applied after the second pi pulse of the detection sequence (blue); Background (black) ; Background corrected timetrace (red); Fit using Tikhonov regularization with a regularization of parameter 1 (green)

Bottom, middle : Fourier transform of the background corrected timetrace

Bottom, right: Distance distribution from Tikhonov regularization with regularization parameter 1

6.3.4 5-pulse PELDOR on Co-NO biradical with ultra-wideband WURST pump pulses

WURST pulse[22] achieve a higher inversion bandwidth for given duration and peak B_1 -field than sech/tanh pulse (see chapter 4.3.4). For 5-pulse PELDOR only the maximum dipolar evolution time is reduced by a prolonged pump pulse duration and not the fidelity of the dipolar spectrum. In the following a 400 ns long WURST pulse with 400 MHz inversion bandwidth with an efficiency over 0.97 in the pass-band is applied on the Co-NO system. The actual pulse shape is shown in Figure 59. The inversion bandwidth of these pulses is compared to the rectangular pump pulse of the same microwave power in Figure 58. The higher bandwidth pulse (red line < 500 MHz bandwidth) is used as second, time fixed pump pulse for dipolar refocusing. Since both pulses must have the same sweep rate for optimum dipolar refocusing the second pulse is longer to achieve a higher bandwidth. The pulse parameters used to calculate the 400 MHz (a) and the 500 MHz (b) WURST pulses according to equation (38) and (39). have been:

a) $T = 400 \text{ ns} ; B_{1\text{max}} = 8.92 \text{ G} ; k = 2\pi 0.012 \text{ rad / ns} ; \beta = \pi / 430\text{ns} ; n = 30;$

b) $T = 480 \text{ ns} ; B_{1\text{max}} = 8.92 \text{ G} ; k = 2\pi 0.012 \text{ rad / ns} ; \beta = \pi / 430\text{ns} ; n = 30;$

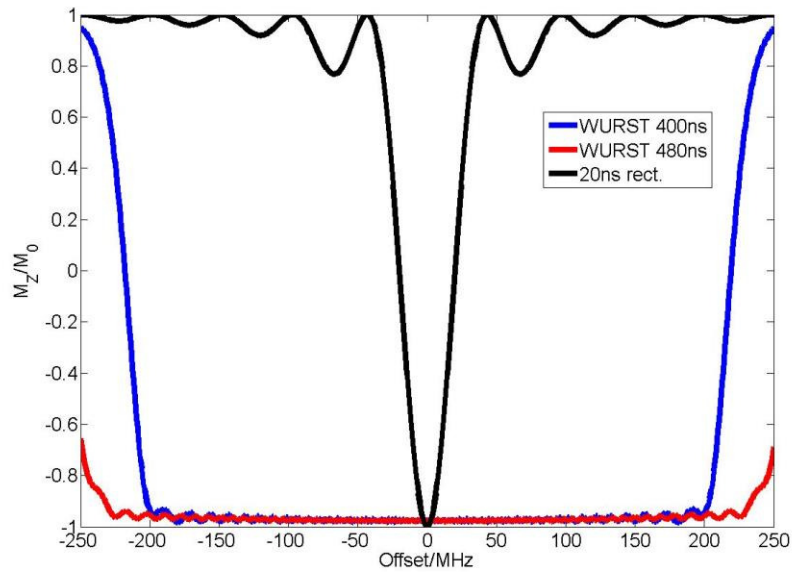


Figure 58 inversion profiles for three inversion pulses utilizing the same microwave power. The WURST pulses are applied as PELDOR pump pulses in a 5-pulse sequence. Black: rectangular shaped 20 ns pulse; blue: 400 MHz broad 400 ns WURST pulse; red: 500 MHz broad 480 ns long WURST pulse.

The comparison of the timetraces obtained with the 5-pulse sequence with 400- and 500 MHz WURST pulses and the 4-pulse sequence utilizing one 20 ns rectangular pump pulse is provided in Figure 60. A more than 7 times higher modulation depth is obtained with the 400 MHz WURST pulse.

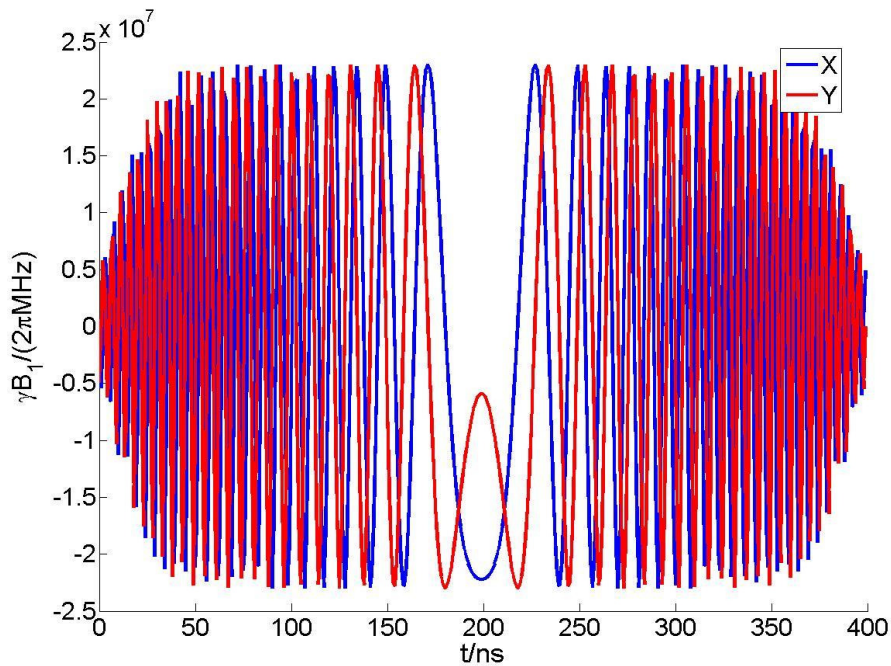


Figure 59 Pulseshape of the 400 ns 400 MHz WURST pulse used as moving pump pulse in the new 5-pulse sequence.

An interesting feature of the 5-pulse timetrace shown in Figure 60 is the absence of any residual 4-pulse signal which should occur at the end of the timetrace. Here the signal rounding by prolonged pump pulses eliminates the 4-pulse artifact. The distance of 2 nm between the nitroxide spin and the Co spin leads to a perpendicular coupling of approximately 6 MHz which gives an oscillation period of 166 ns while the length of the pump pulse is 400 ns which causes an almost complete washout of dipolar oscillation for the residual 4-pulse signal.

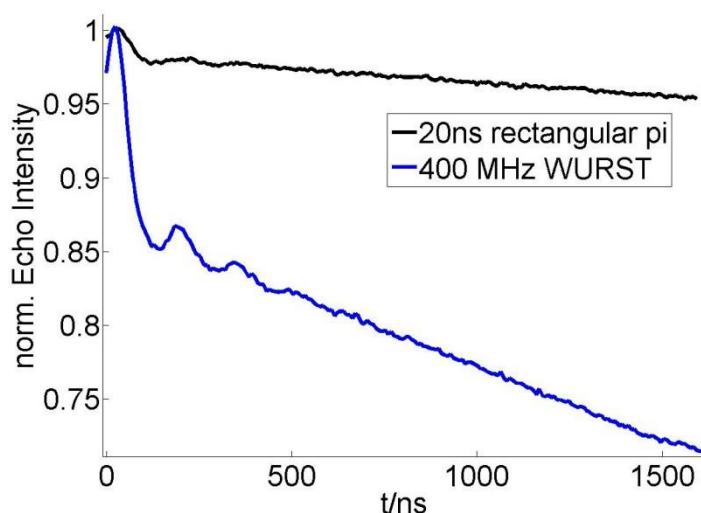


Figure 60 Black: 4-pulse PELDOR timetrace on Co-NO system recorded with a 20 ns rectangular pump pulse. Blue: 5-pulse timetrace recorded with a pair of 400- and 480 MHz WURST pulses. The modulation depth increased by a factor of 7.2.

To conclude this chapter a table of S/N values for the above shown experiments is provided which shows the actual increase of S/N for the sech/tanh pump pulses.

pump puls(es)	20ns rectangular	150 MHz sech/tanh	150MHz sech/tanh 225 MHz sech/tanh
biradical			
NO-NO biradical	39	86	
Co-NO biradical	35	87	109

Table 1: S/N ratios for the different pump pulse schemes. Black: 4-pulse PELDOR; blue: 5-pulse PELDOR.

The Signal to Noise Ratios have been calculated using:

$$\frac{S}{N} = \lambda \frac{S(t=0)}{\sigma} \quad (69)$$

with λ being the modulation depth obtained from Deer Analysis[55] , $S(t=0)$ being the signal amplitude at the origin of the timetrace and σ being the standard deviation of the imaginary part of the timetrace after background correction with a fourth degree polynomial fit.

6.3 7-pulse PELDOR for enhanced dipolar window

The attempts made so far to increase the S/N of PELDOR spectroscopy have been concentrated solely on enhancing the modulation depth. A recent publication by Freed and coworkers presented a new 5-pulse PELDOR sequence to increase the dipolar window[56]. The underlying principle is the reduction of decoherence on the A-spin induced by nuclear spin diffusion as described in chapter 4.4.4 and 4.4.5. The key idea was to make the first tau period equal to the second tau period while keeping the duration from the 90° pulse to the refocused echo. To avoid the loss in dipolar evolution time a second pump pulse was introduced which extended the dipolar evolution time from τ_2 for the 4-pulse sequence (see Figure 41) to $\tau_2 + \tau_1$ (see Figure 51).

The best solution certainly would be to substitute the refocused echo sequence on the A-spin by a CPMG sequence to achieve the longest possible observation window. Then, every refocusing pulse on the A sequence requires a pump pulse on the B-spin to achieve a complete dipolar defocusing. Rectangular pulses are not suitable for this task since their bad inversion efficiency of off-resonant spins makes it impossible to achieve multiple inversions over the pulse bandwidth with good efficiency. The problem could be solved for the 5-pulse sequence since the only additional dipolar pathway is suppressed by choosing a higher bandwidth second pump pulse[53, 56]. In the case of more than two pump pulses more than one additional dipolar pathway occurs due to incomplete inversion and a suppression of any particular pathway causes an increased weight of other dipolar pathways, thus pump pulses of equal bandwidth have to be used. The requirement on these pump pulses is an almost rectangular shaped inversion profile for quantitative inversion within a specified frequency band and zero inversion outside this band. This is best fulfilled for sech/tanh pulses described in chapter 4.3.2.

The actual pulse performance was experimentally found to be worse than expected from simulations which means that the average probability that a spin which was flipped by a sech/tanh pulse is also flipped by a second sech/tanh pulse is in the range of 80%. This reduced the max number of refocusing pulses to 3 and thus the new sequence is called the 7-pulse PELDOR sequence. A comparison between the standard 4-pulse sequence and the new 7-pulse sequence is given in Figure 61. The measurement time was approximately the same for both measurements. The huge increase in time window and S/N seen in Figure 61 shows the superiority of the 7-pulse CPMG-PELDOR method over the widely applied 4-pulse sequence[23].

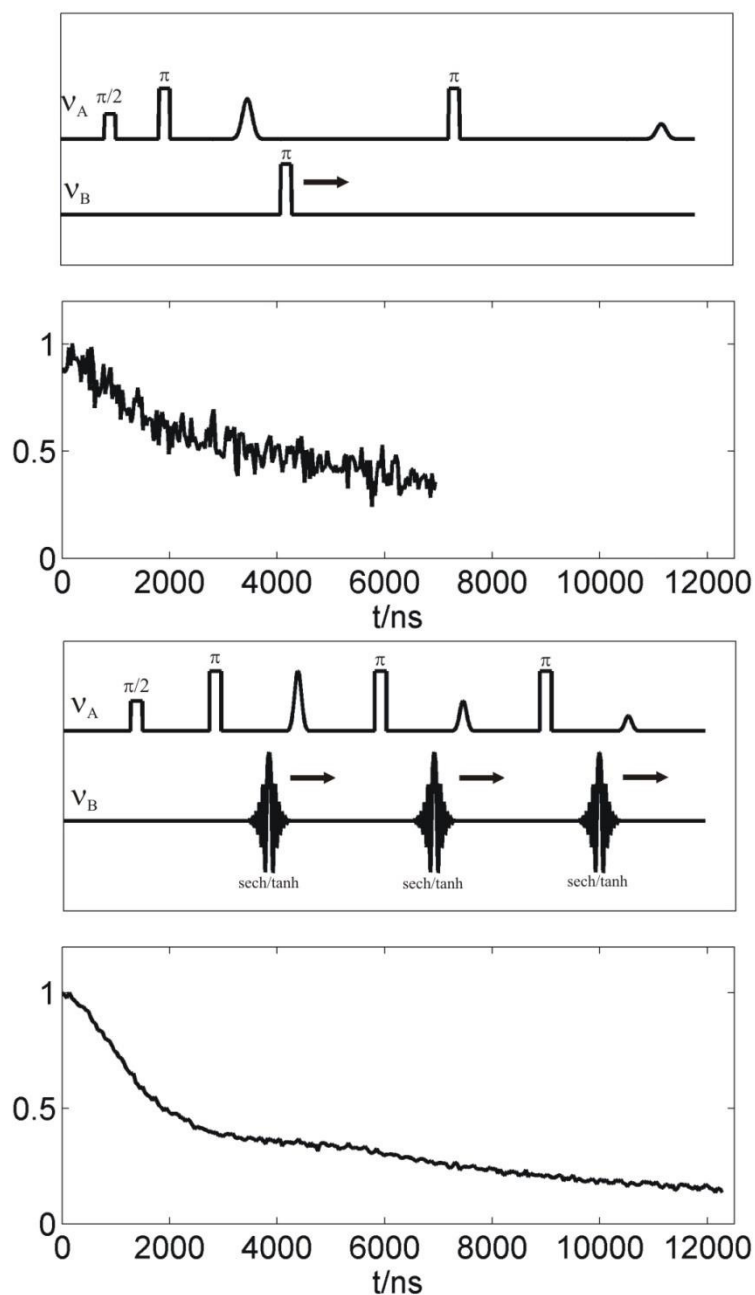


Figure 61 Comparison of dipolar evolution time traces of the BetP trimer obtained with the standard 4-pulse PELDOR sequence (upper two panels) and with the new 7-pulse CP PELDOR sequence (lower two panels). Both experiments are performed at 50 K temperature. The 7-pulse signal was recorded over 2.5 h with a 50 MHz bandwidth sech/tanh pump pulses, whereas the 4 pulse signal was averaged over 1 h and utilized a classical 12 ns rectangular pump pulse.

6.3.1 7-pulse CPMG-PELDOR Sequence

The 7-pulse CPMG-PELDOR sequence is shown in Figure 62. In contrast to the widely applied 4-pulse PELDOR sequence more than one possibility exists to increment the time evolution of the pump pulses. The phase of an A-spin which is coupled to a B-spin accumulates until the formation of the third refocused echo and is given by:

$$\varphi = \omega_{\text{dip}}(\mathbf{T}_1 + \mathbf{T}_2 + \mathbf{T}_3 - \tau_1 - \tau_2 - \tau_3) \quad (70)$$

This expression is derived as described in chapter 6.3.4 for the 5-pulse sequence. The dipolar coupling strength in radians is given by ω_{dip} . The other parameters are indicated in Figure 62.

From equation (70) it is clear that the max dipolar evolution is achieved if $\mathbf{T}_1, \mathbf{T}_2, \mathbf{T}_3 = 0$ which could only be achieved with overlapping A- and B-pulses which is experimentally not possible. To reach the time zero of dipolar evolution the condition $\mathbf{T}_1 + \mathbf{T}_2 + \mathbf{T}_3 = \tau_1 + \tau_2 + \tau_3$ has to be fulfilled. The three pump pulses can be arbitrarily incremented as long as no pulse overlap between the pump pulses and refocusing the pulses or between the last pulse and the third refocused echo (which is detected), occurs. However, as will be explained later, the way the pump pulses are incremented influences the position but not the intensity of unwanted PELDOR timetraces resulting from incomplete inversion of B-spins by the pump pulses.

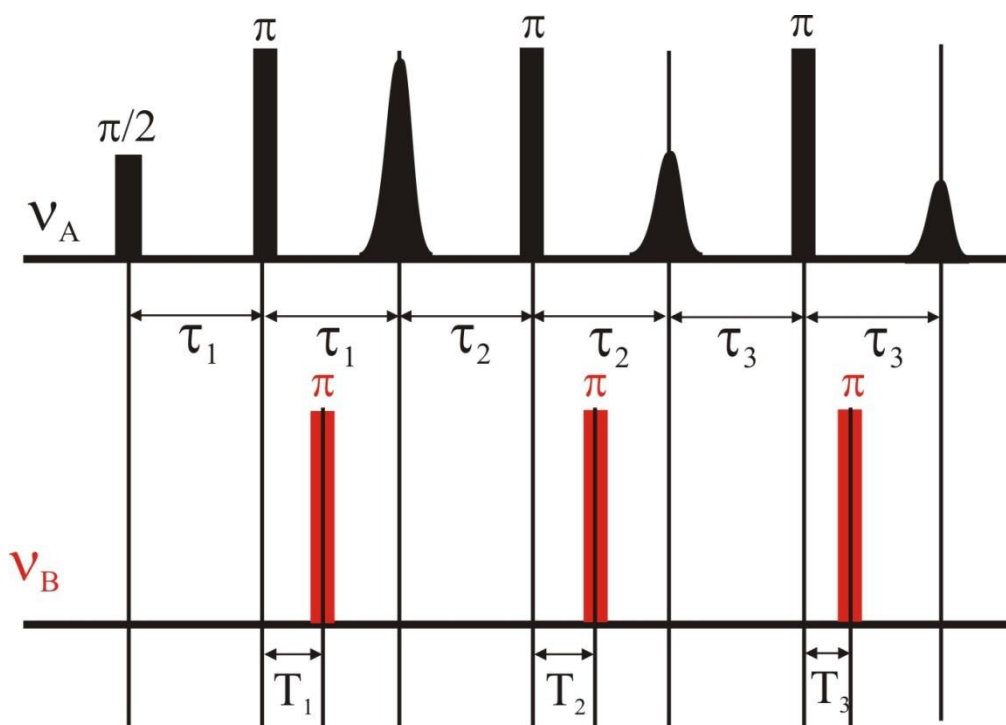


Figure 62 7-pulse PELDOR sequence

6.3.2 Signal for 7-pulse PELDOR

The modulation depth parameter λ , which stands for the fraction of B-spins which are flipped by the pump pulse in the standard 4-pulse PELDOR is not sufficient to describe the 7-pulse signal. A second parameter p is needed which is the average probability that a spin flipped by the first pump pulse is also flipped by a second pump pulse. If $p \neq 1$, $2^3=8$ dipolar signals with different intensities, time-zeros, and -steps contribute to the 7-pulse signal. These can be divided into three pathways weighted by $\lambda(1-p)^2$, where only one of the three pump pulses does flip the B-spin, three pathways weighted by $\lambda p(1-p)$ where two pump pulses flip the B-spin and finally the desired 7-pulse path with a weight of λp^2 . In Figure 63 All possible non-7-pulse pathways which contribute a time dependent signal all the possible pathways which constitute the time dependent non-7 pulse PELDOR signals are depicted. The phase φ of the dipolar evolution for each pathway (as numbered in Figure 63 All possible non-7-pulse pathways which contribute a time dependent signal) is given by equation 71-77 with $\varphi_{1\bar{2}\bar{3}}$ i.e. being the phase of the pathway where only the first pump pulse flips the B-spin:

:

$$1) : \varphi_{1\bar{2}\bar{3}} = (\tau_1 - T_1)\omega_{\text{dip}} \quad (71)$$

$$2) : \varphi_{\bar{1}2\bar{3}} = (\tau_2 - T_2)\omega_{\text{dip}} \quad (72)$$

$$3) : \varphi_{\bar{1}\bar{2}3} = (\tau_3 - T_3)\omega_{\text{dip}} \quad (73)$$

$$4) : \varphi_{1\bar{2}3} = (\tau_1 + \tau_2 - T_1 - T_2)\omega_{\text{dip}} \quad (74)$$

$$5) : \varphi_{\bar{1}23} = (\tau_3 - \tau_1 + T_1 - T_3)\omega_{\text{dip}} \quad (75)$$

$$6) : \varphi_{12\bar{3}} = (\tau_2 + \tau_3 - T_2 - T_3)\omega_{\text{dip}} \quad (76)$$

For all three pump-pulses flipping the B-spin:

$$\varphi_{123} = (\tau_1 + \tau_2 + \tau_3 - T_1 - T_2 - T_3)\omega_{\text{dip}} \quad (77)$$

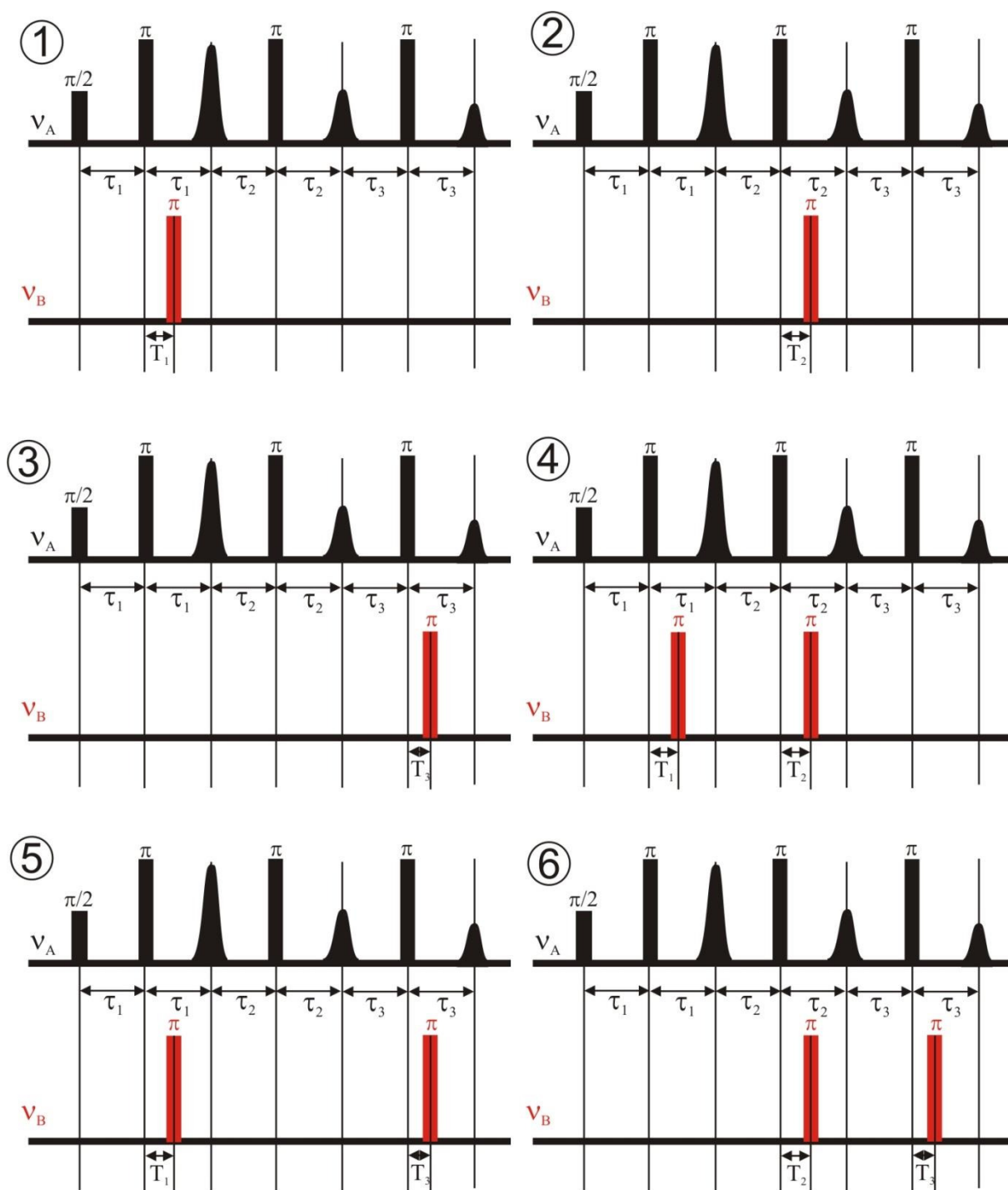


Figure 63 All possible non-7-pulse pathways which contribute a time dependent signal

The 7-pulse CPMG signal (V_7) is like the standard 4-pulse PELDOR signal a product of an intermolecular (V_{inter}) and an intramolecular (V_{intra}) contribution, averaged over all spatial orientations θ .

$$V_7 = \langle V_{intra} \rangle_{\theta} \cdot V_{inter} \quad (78)$$

A pair of one A- and one B-spin can only take one particular dipolar pathway in one experiment. Even if this pair takes another pathway in a successive experiment the amount of pairs which takes this particular pathway is the same as in the previous experiment due to the large number of spins typically involved in an EPR experiment. The fraction of spin-pairs which take a particular dipolar pathway does not affect the signal resulting from other dipolar pathways. Thus, the intramolecular signal is a superposition of all dipolar pathways weighted by their respective probability which is solely determined by the flip-probability p ; $\bar{p} = 1 - p$. The intramolecular 7-pulse signal as a function of the dipolar phase (equation (71)-(77)) and modulation depth parameter λ is given by

$$\begin{aligned}
V_{7\text{intra}} = & \lambda \bar{p}^2 (\cos(\varphi_{1\bar{2}\bar{3}}) + \cos(\varphi_{\bar{1}2\bar{3}}) + \cos(\varphi_{\bar{1}\bar{2}3})) + \\
& \lambda p \bar{p} (\cos(\varphi_{12\bar{3}}) + \cos(\varphi_{\bar{1}\bar{2}3}) + \cos(\varphi_{\bar{1}23})) + \\
& \lambda p^2 (\cos(\varphi_{123})) + 1 - \lambda
\end{aligned} \tag{79}$$

Each experiment divides the whole B-spin ensemble into certain sub-ensembles of which each corresponds to one particular dipolar pathway. The magnitude of each sub-ensemble is given by the weight of the respective dipolar pathway. Due to the large number of spins one can regard those B-sub-ensembles as homogeneous distributed throughout the sample but with different dipolar histories (pathways) and concentrations (weights). Each A-spin is affected by each B-sub-ensemble. The question of how the intermolecular decay looks like for the 7-pulse experiment can be answered by the intramolecular analogy: If more than one intramolecular B-spin is present the intramolecular signal is a product of the individual pairs signals constituted by the observed A-spin with one of each intramolecular B-spin[57]. This can be transferred to the case of more than one intermolecular B-spin ensembles. The pairs are then A-spins with different B-spin sub-ensembles. Thus, for 7-pulse PELDOR, the intermolecular decay function is a product of all individual background functions originating from different dipolar pathways.

$$V_{7\text{inter}} = \exp \left(-\lambda ac \left(\begin{array}{l} \bar{p}^2 (|\tau_1 - T_1| + |\tau_2 - T_2| + |\tau_3 - T_3|) + \\ p \bar{p} (|\tau_1 + \tau_2 - T_1 - T_2| + |\tau_3 - \tau_1 + T_1 - T_3| + |\tau_2 + \tau_3 - T_2 - T_3|) + \\ p^2 (|\tau_1 + \tau_2 + \tau_3 - T_1 - T_2 - T_3|) \end{array} \right) \right) \tag{80}$$

With c being the radical concentration and a being $\frac{2\pi g^2 \mu_B^2 \mu_0}{9\sqrt{3}\hbar}$, where μ_B is the Bohr magneton.

6.3.3 Application of the 7-pulse PELDOR sequence on the trimeric betaine transporter BetP.

The betaine transporter BetP consists of three identical monomers. 2 and 3-dimensional crystal structures have been obtained for the trimer. All of these structures show the subunits in different conformational states what suggests an asymmetric state[58, 59]. However, a common assumption for such systems is that each subunit adopts its most favorable state which is the same for all three and therefore leads to a symmetric trimer. Asymmetrically bound lipids may force the betp trimer to the asymmetric state during crystallization. To determine the symmetry properties of betp in more physiological conditions the monomers have been spin labeled[60] at the S140 position (see Figure 64) to enable distance measurements between the monomers by means of PELDOR spectroscopy.

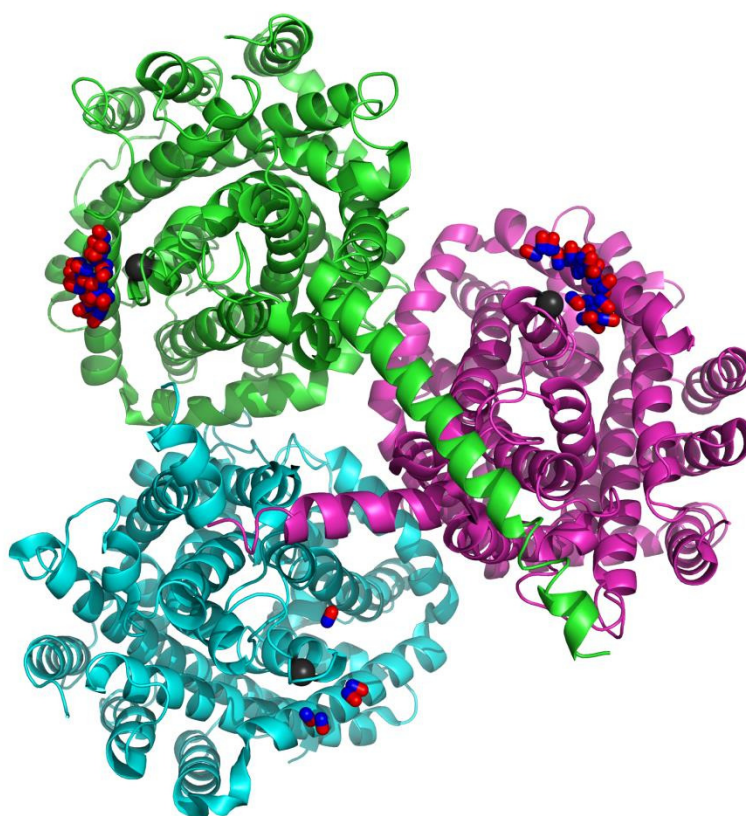


Figure 64 Crystal structure of BetP (4DOJ.pdb). The rotamers calculated by MMM[61] of the attached nitroxides (NO groups) at residue S140 are shown as balls (red/blue). The α -C's where the MTSSL spin labels are attached are marked as large red spheres. The rotamers have been calculated for a temperature of 298 K to obtain a reasonable population also for the blue protomer.

The distance between the labels in the trimer is approximately 6 nm whereas the 4-pulse dipolar window could only be extended to 5-7 μs due to nuclear spin diffusion of protons of BetP. This time window is by far too short to observe reliable distance distributions with a sub nm resolution at a mean distance around 6 nm. However, the time window could be extended to 12.5 μs with the 7-pulse PELDOR sequence.

The following 7-pulse PELDOR experiments on BetP were performed at Q-band frequencies at a static field of 1.2068 T. The frequencies ν_A and ν_B have been set to 33.741 GHz and 33.817 GHz which gives a pump-probe offset of 76 MHz. The pump and probe positions as well as the bandwidth of the pump pulse and the probe sequence are depicted in Figure 65.

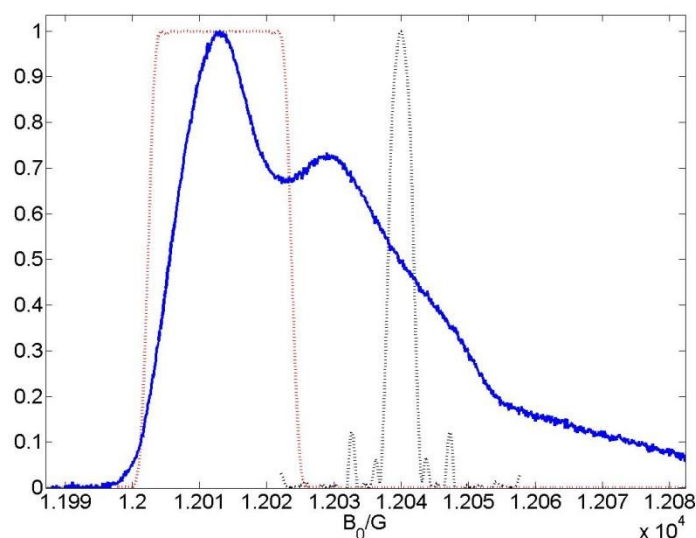


Figure 65 Bandwidth and position of the pump-pulse (red) and probe sequence (32 ns, 48 ns, 48 ns, 48 ns) (black) drawn into the nitroxide pulsed field sweep spectrum at Q-band.

The actual pulse sequence which enabled the 12.5 μs time window is depicted in Figure 66. For detection 32 ns $\pi/2$ and 64 ns π pulses have been used. The length of the π pulses was chosen to minimize the echo decay by instantaneous diffusion[62]. The delays d_2 and d_4 have been incremented with 16 ns whereas the third pump pulse (d_6) was incremented with 12 ns to avoid any disturbance of the echo induced by the pump pulse. The delays d_3 and d_5 have been incremented by -16 ns whereas d_7 has been incremented by -12 ns.

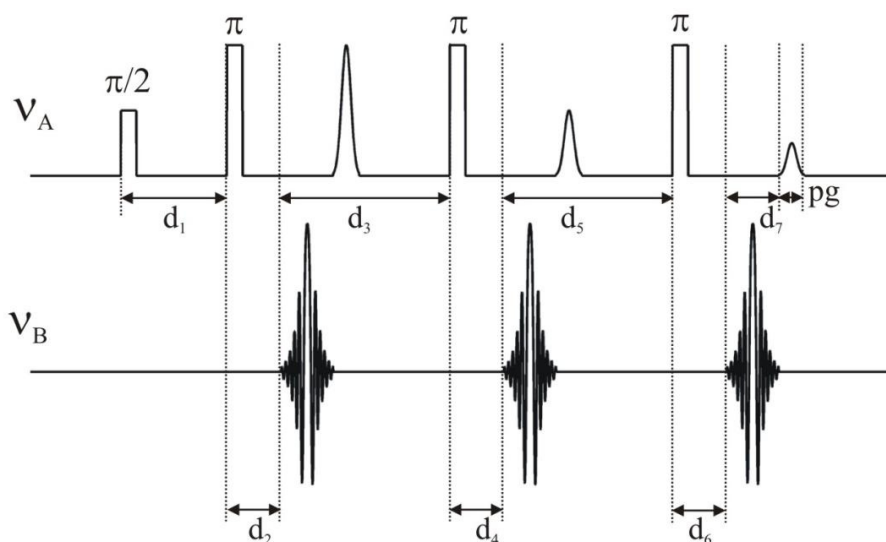


Figure 66 7-pulse PELDOR sequence with interpulse delays d1-d7. The initial-delays which had been set for the betp-measurement with a 12.5 μ s time window have been: d₁: 3900 ns; d₂: 64 ns; d₃: 8636 ns; d₄: 64ns; d₅: 8936ns; d₆: 64 ns; d₇: 4791 ns; pg: 140 ns (integration window). The video amplifier bandwidth was set to 25 MHz. All pump pulses have been sech/tanh pulses.

6.3.4 Requirements on pump pulses for 7-pulse PELDOR

The pump pulses have been optimized for a moderate bandwidth of 50 MHz to avoid a strong intermolecular decay of the echo. The duration of 400 ns seems high for a 50 MHz bandwidth pulse but was chosen to achieve an inversion profile which comes close to the ideal of a rectangular shaped inversion profile. The complete set of pulse parameters according to equations (36) and (37)

$\beta=0.02$; $T = 400$ ns ; $BW = 0.03$ GHz; $B_{1,max} = 7.1$ G. The actual shape of the pulse is depicted in Figure 67.

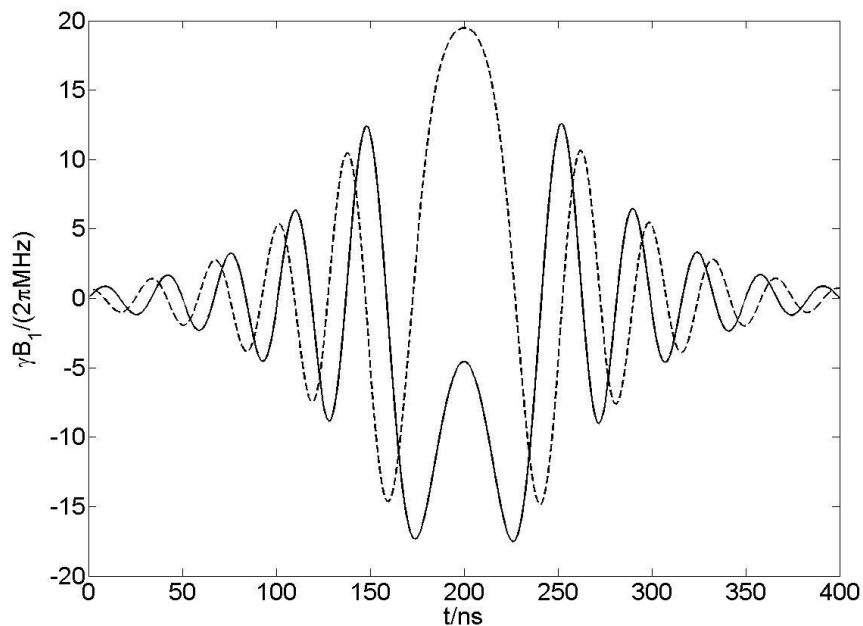


Figure 67 Shape of the 50 MHz sech/tanh pulse applied in 7-pulse PELDOR at Q-band frequencies.

The comparison of the sech/tanh inversion profile with that obtained with a rectangular shaped inversion pulse is depicted in Figure 68

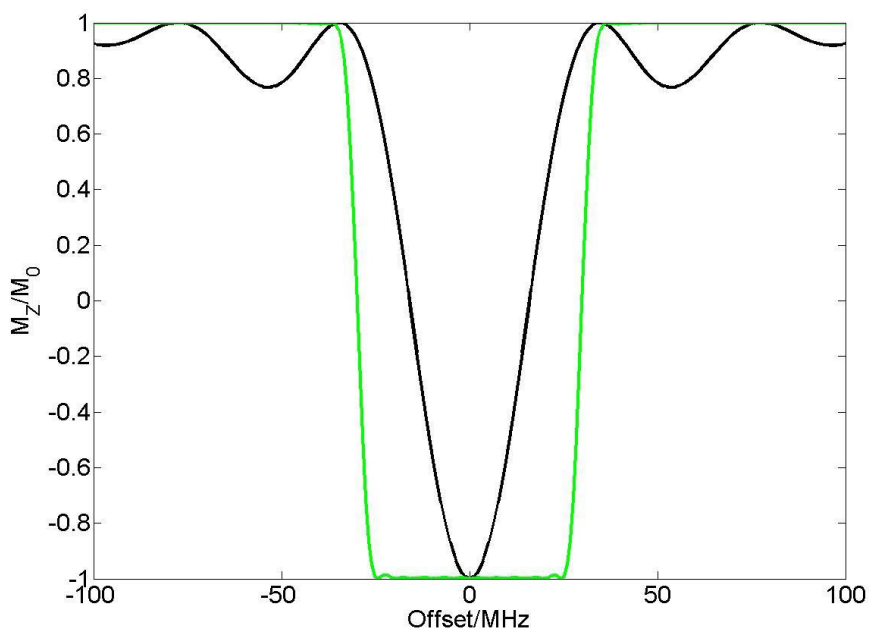


Figure 68 Inversion profiles of the 400 ns sech/tanh inversion pulse (green line) and a rectangular inversion pulse with a duration of 13 ns corresponding to $B_{1\max} = 7.1\text{G}$

6.3.5 Signal rounding in 7-pulse PELDOR

The offset dependent dipolar evolution time seen for the 4-pulse PELDOR with one sech/tanh pump pulse is also present in the 7-pulse sequence. Since there are three identical sech/tanh pump pulses the time zero of the dipolar evolution is distributed over three times the length of one pump pulse. This can be reduced to the time of one pump pulse if one pulse is substituted by its time reversed counterpart. The time reversed pulse is obtained by inverting the sign of the imaginary component of the pulse which reverses the direction of the frequency sweep. It is, in principle possible to make the time zero of the dipolar evolution offset independent for the 7-pulse sequence. This can only be achieved with at least one pump pulse differing in sweep rate from the other two which causes that the flip probability is not the same for each pump pulse. This then would complicate the analysis shown in the following. The problem of signal rounding could be easily overcome by a 9-pulse sequence with 4 equal bandwidth and duration pump pulses which are pairwise compensated. A 9-pulse sequence would need a higher p (flip probability) of the pump pulses to achieve the necessary weight of the 9-pulse signal, though.

6.3.6 Incrementation of the pump pulses.

The way how the pump pulses are incremented affects the time zero but not the weight of different possible dipolar pathways. The weight of each dipolar pathway is solely given by the flip probability p of a pump pulse. The two 7-pulse sequences shown in Figure 69 differ only in the incrementation of the last pump pulse.

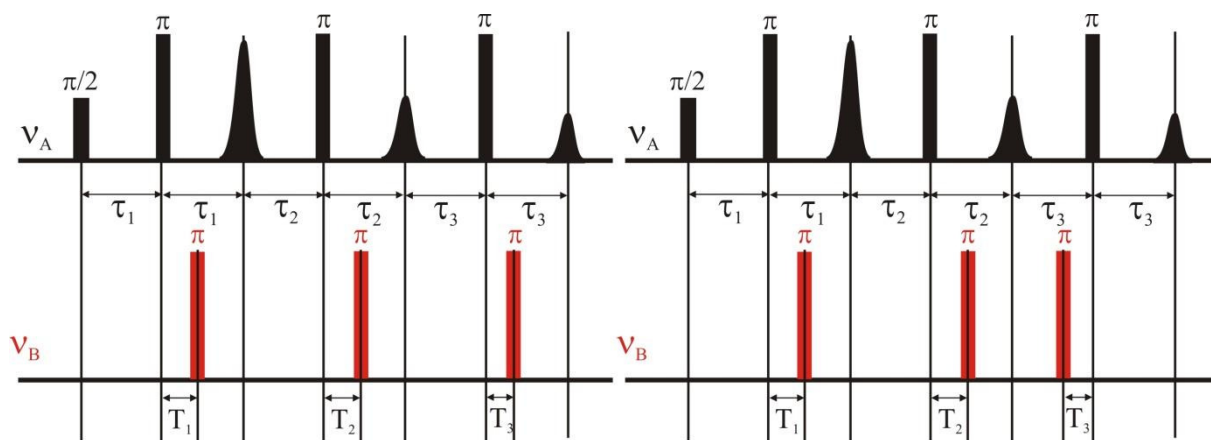


Figure 69 Two possible ways to conduct a 7-pulse PELDOR measurement. Left : all pump pulses are positioned directly after the refocusing pulses and are incremented to the right. Right: The third pump pulse is positioned left to the third refocusing pulse and incremented to the left.

The timetraces obtained with both ways of setting up the 7-pulse experiment (see Figure 69) are shown in Figure 70. The timetrace obtained with the sequence shown in the right panel of Figure 69 (black line Figure 70) has the time zero of non-7-pulse PELDOR signals lying approximately in the middle of the 7-pulse window. The relative intensity of the 7-pulse signal at this instance of time compared to the sum of all non-7 pulse signals is small which results in a strong distortion of the 7-pulse signal. The advantage of the pulse sequence shown in the left panel of Figure 69 is that the time zeros of the non-7 pulse signals almost coincide with the time zero of the 7-pulse signal thus causing a smaller distortion of the 7-pulse signal and making it therefore easier to correct.

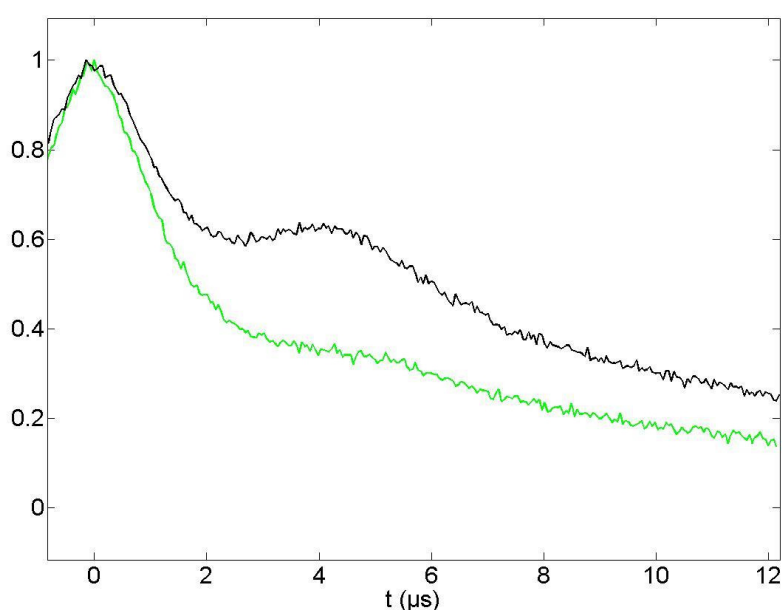


Figure 70 7-pulse PELDOR timetraces for different setups. The green trace is obtained with the incrementation shown in Figure 69 left panel (green) whereas the black trace is obtained with the incrementation shown in the right panel of Figure 69.

6.3.7 Separation of the intermolecular and intramolecular signal for 7-pulse PELDOR

The flip probability p has to be known for the intermolecular background correction according to equation (80) as well as the later shown subtraction of the non-7 pulse signals from the intramolecular signal (equation (79)). The flip probability was determined here experimentally by means of a 5-pulse PELDOR experiment[56] on a monoradical (200 μm Tempone) in d_8 -glycerol/ D_2O . Since no intramolecular signal is present only the

intermolecular decay function is visible. This decay however depends strongly on p . The signal of 5-pulse PELDOR on a homogeneous distributed monoradical is given by:

$$V(T) = E_0 e^{(-\lambda a c ((1-p)|t-t_4| + p|t-t_5|))} \quad (81)$$

Where t_4 is the time zero of the 4-pulse pathway, t_5 is the time zero of the 5-pulse pathway and t the time the first pump pulse has advanced. With c being the radical concentration and a being $\frac{2\pi g^2 \mu_B^2 \mu_0}{9\sqrt{3}\hbar}$, where μ_B is the Bohr magneton. Equation (81) was fitted to the experimental 5-pulse decay which gave $p=0.77$. The experimental data as well as the fit is shown in Figure 71.

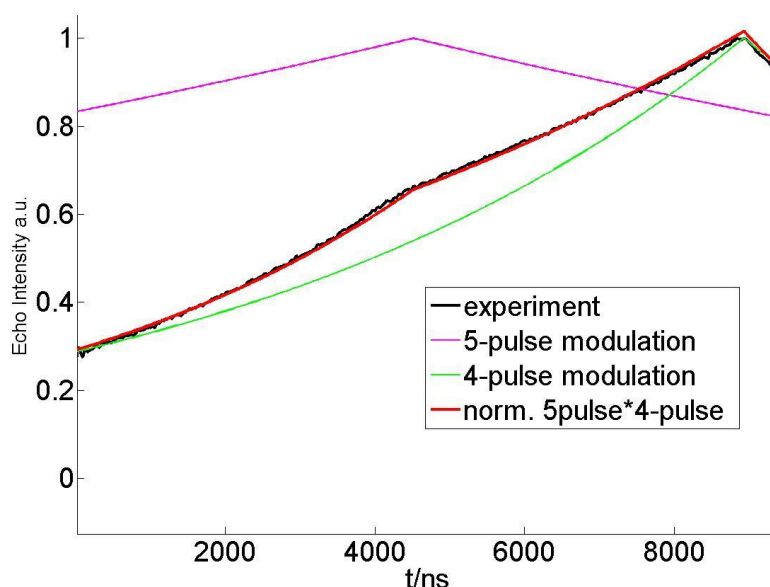


Figure 71 5-pulse PELDOR on a monoradical in frozen solution.

Since p was known from the 5-pulse experiment, the intermolecular decay of the 7-pulse experiment could be fitted to equation (80). The true intramolecular distance distribution is only obtained if the intermolecular decay is known and subtracted. A Pake pattern in the time domain can be considered as a superposition of a rapidly decaying part and a part originating from the singularities oscillating with a frequency $\nu_{\text{dip}\perp} = \frac{52 \text{ MHz}}{r^3}$. The first part is almost completely decayed during the time $\nu_{\text{dip}\perp}^{-1}$. The latter oscillates with only small damping thus allowing to fit the intermolecular background function to the experimental signal for

times longer than $\nu_{\text{dip},\perp}^{-1}$. A reasonable fit of the intermolecular decay thus requires at least two times the period of the perpendicular dipolar oscillation[62]. The intramolecular signal is damped to zero in case of broad distance distributions for times larger than T_{dd} [62]. The signal takes the form $E(T) = (1 - \lambda)B(T)$ for times $T > T_{\text{dd}}$ with $B(T)$ being the intermolecular decay function. This allows a very accurate estimation of the background function for $T > T_{\text{dd}}$.

The 7-pulse measurement was conducted such that the time zeros of the non-7-pulse signals are close to the time-zero of the 7-pulse evolution. This avoids disturbing signals from non-7 pulse evolutions towards the end of the timetrace. Thus a background function based on equation (80) could be fitted to the end of the experimental 7-pulse signal. The fit as well as all intermolecular decay function from different dipolar pathways is shown in Figure 72.

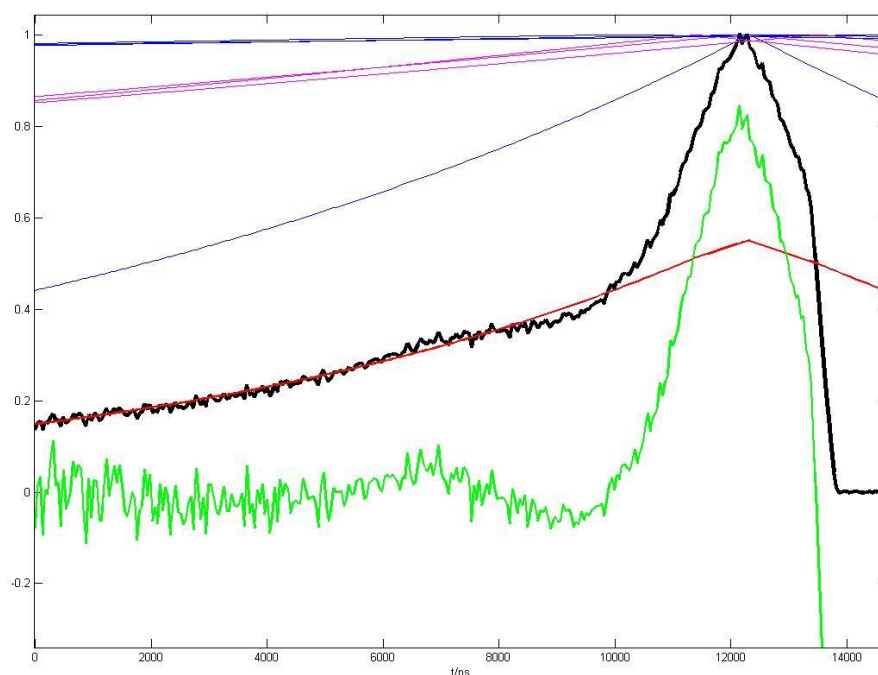


Figure 72 intermolecular decay functions in 7-pulse PELDOR. Orange: 5-pulse background functions; Blue : 4-pulse background function; violet : 7-pulse background function .The red line is the product of all individual background functions and a time independent factor which is then the intermolecular signal for the 7-pulse experiment. The green line shows the experimental signal (black) after background correction.

6.3.8 Extracting the 7-pulse evolution iteratively

After background correction and subtraction of the unmodulated part the measured 7-pulse signal is a superposition of all dipolar pathways of which the non-7 pulse signals have to be subtracted. Since the true timetrace is not known we choose an iterative way to correct the measured signal. The non-7-pulse signals are constructed from the uncorrected 7-pulse signal via resampling and shifting the time zero. The so constructed signals are weighted with their respective probability according to equation (79) and are then subtracted from the uncorrected 7-pulse signal. In a succeeding step the first order corrected signal is used to construct the non-7-pulse signals again which are then also subtracted from the uncorrected signal. These steps are repeated until convergence.

The following depicts the calculation of the signal origination from the pathway shown in the first panel of Figure 63.

The background corrected 7-pulse signal is symmetrized around the 7-pulse time zero given by equation (68). The outcome is shown in Figure 73.

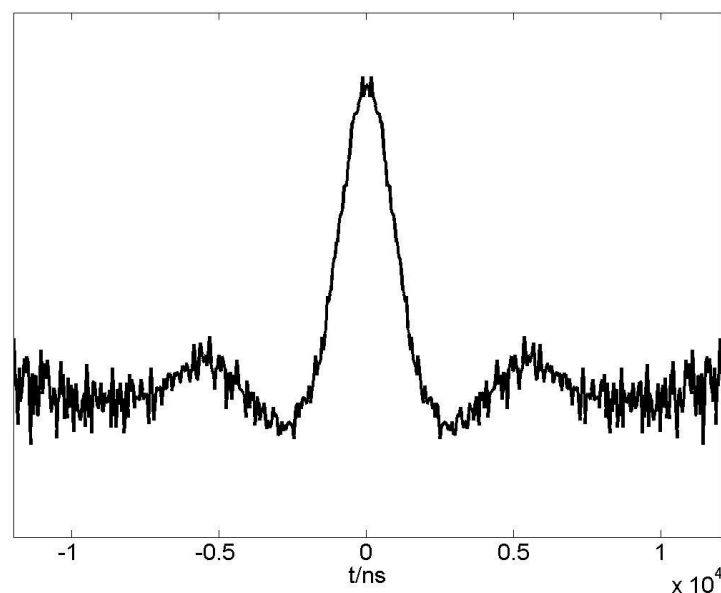


Figure 73 symmetrized background corrected 7-pulse measurement

The symmetrized signal is then resampled by a factor of $\frac{\Delta_1 + \Delta_2 + \Delta_3}{\Delta_1}$, with Δ_i being the time increment of the i th pump pulse. The resampling is necessary because this particular pathway evolves with $\Delta_1=16$ ns whereas the measured signal evolves with $\Delta_1 + \Delta_2 + \Delta_3=44$ ns per time step (Figure 74).

The time t_i advanced by the i th-pump pulse is incremented in steps Δ_i . The total time T_i advanced by the i th pump pulse is $T_i = n\Delta_i$. A zeropoint (zp) is the number of time steps until the time zero of an individual pathway is reached.

The zero points zp are calculated using equations (82)-(88) where for example $zp_{1\bar{2}\bar{3}}$ is the zero point of the pathway where only the first pump pulse flips the B-spin.

$$zp_{1\bar{2}\bar{3}} = \frac{\tau_1}{\Delta_1} \quad (82)$$

$$zp_{\bar{1}2\bar{3}} = \frac{\tau_2}{\Delta_2} \quad (83)$$

$$zp_{\bar{1}\bar{2}3} = \frac{\tau_3}{\Delta_3} \quad (84)$$

$$zp_{12\bar{3}} = \frac{\tau_1 + \tau_2}{\Delta_1 + \Delta_2} \quad (85)$$

$$zp_{\bar{1}23} = \frac{\tau_2 + \tau_3}{\Delta_2 + \Delta_3} \quad (86)$$

$$zp_{1\bar{2}3} = \frac{\tau_1 - \tau_3}{\Delta_1 - \Delta_3} \quad (87)$$

$$zp_{123} = \frac{\tau_1 + \tau_2 + \tau_3}{\Delta_1 + \Delta_2 + \Delta_3} \quad (88)$$

The number of time steps between the time zero of the 7-pulse evolution and the time zero of the first artificial trace (Figure 63) is $zp_{123} - zp_{1\bar{2}\bar{3}} = \frac{\tau_1 + \tau_2 + \tau_3}{\Delta_1 + \Delta_2 + \Delta_3} - \frac{\tau_1}{\Delta_1}$. The so shifted trace is multiplied by its probability $p\bar{p}^2$ and subtracted from the background corrected 7-pulse signal Figure 75. This is done for all dipolar pathways which contribute a time-dependent signal. The three 5-pulse and three 6-pulse dipolar pathways weighted with their probabilities are shown in Figure 76.

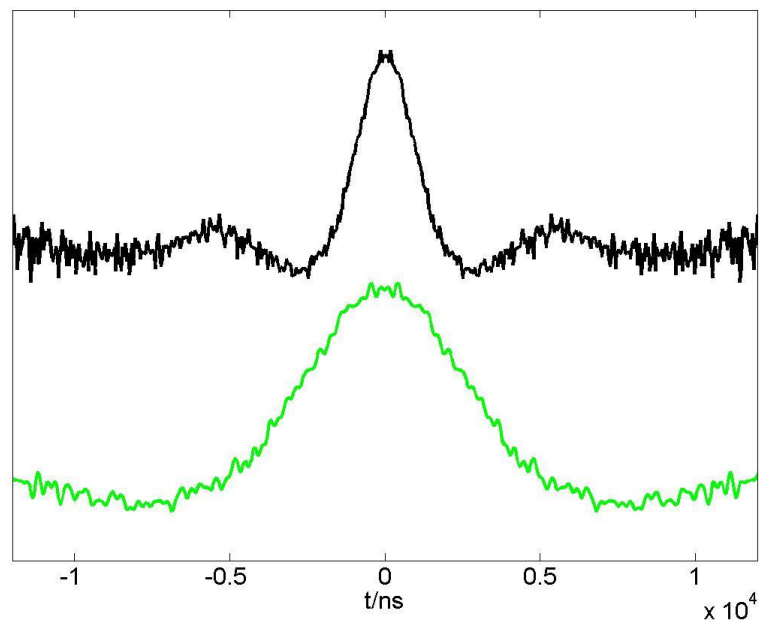


Figure 74 The green trace is resampled by a factor 44/16 to achieve the correct evolution of the 4-pulse trace.

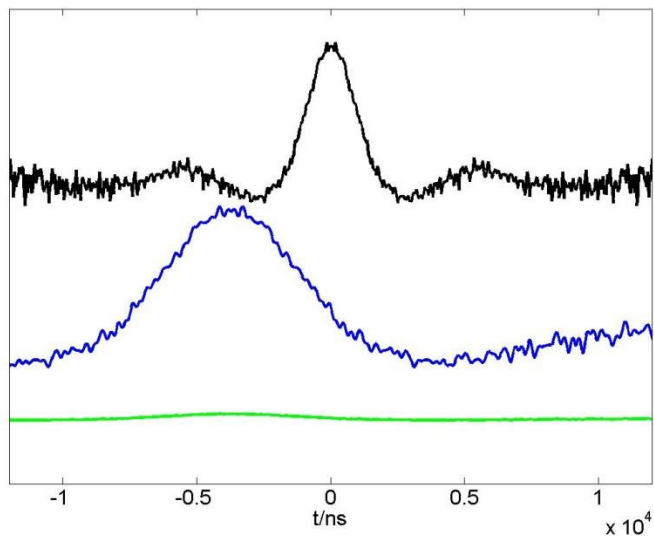


Figure 75 The 4-pulse trace is shifted horizontally to its time zero (blue). The green trace is obtained by weighting the blue trace with the probability of the 4-pulse pathway \bar{p}^2 .

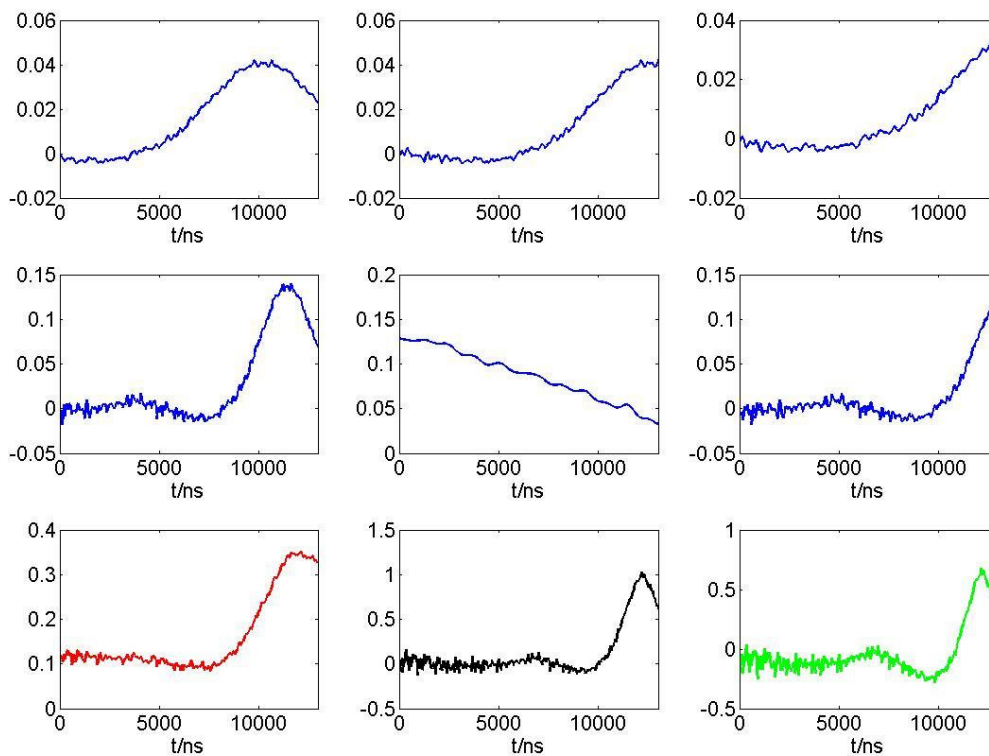


Figure 76 Corrected timetrace after the first iteration. The first row shows the three five-pulse pathways weighted with their probability. The middle row shows the three six-pulse artifacts weighted with their probability. The green trace is obtained by subtracting the red line which is the sum of the 5 -and 6-pulse traces from the background corrected 7-pulse measurement (black).

The first order corrected timetrace is closer to the true 7-pulse dipolar evolution. The succeeding iteration utilizes the previous corrected timetrace to calculate the 5-and 6-pulse traces again. These are then subtracted from the original background corrected 7-pulse evolution. Figure 77 shows the result after 20 iterations in comparison to the first iteration. At this stage no further change of the shape of the corrected timetrace could be observed.

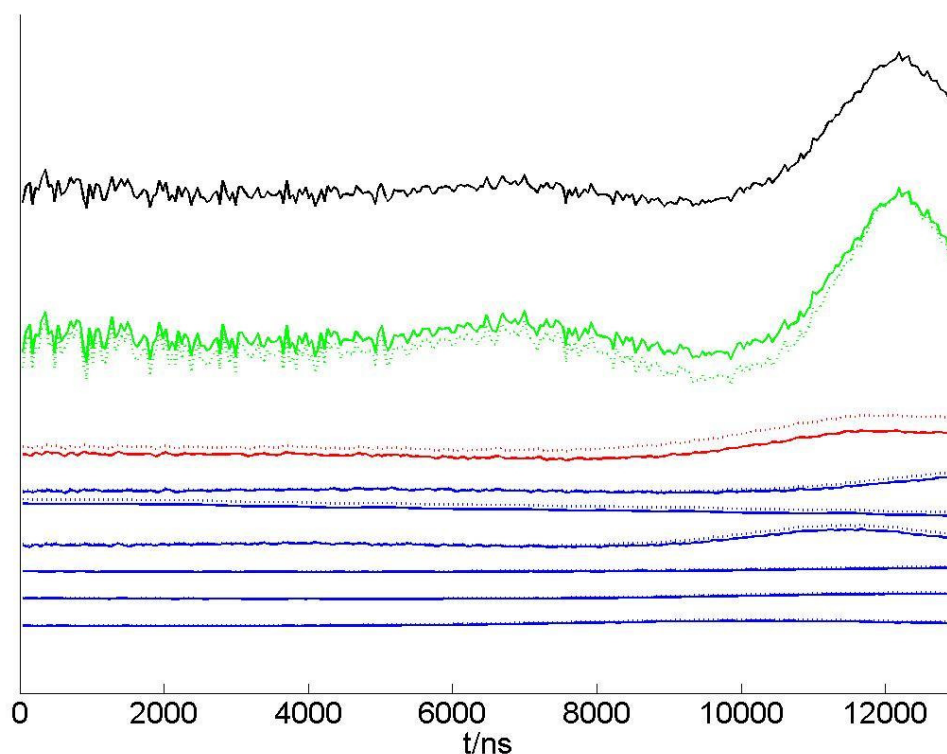


Figure 77 7-pulse evolution after 20 iterations. The green trace is obtained by subtracting the red line which is the sum of the 5 pulse artifacts (first three traces from bottom) –and the 6-pulse artifacts (three traces underneath the red trace) from the background corrected 7-pulse measurement (black). The dotted lines show the zeroth iteration.

The corrected 7-pulse evolution was then inverted utilizing Tikhonov regularization provided by DeerAnalysis which yielded the distance distribution shown in Figure 79. The fit is shown in Figure 78.

At this point no further analysis of the results obtained on BetP will be made despite a brief discussion. The distance distributions shown in Figure 79 reveal a slightly broader distribution for BetP in a frozen buffer solution than for the X-ray measurements. The splitting seen in the crystal structure is attributed to the rotamer[63] population of one protomer seen in Figure 64 (blue protomer). It should be emphasized that for the first time

PELDOR-distance measurements on a non-deuterated protein with a 12.5 μs time window have been performed. The high precision of this measurement enabled to draw the conclusion that the asymmetries found for the crystal structures are smaller than those which are observed in frozen detergent.

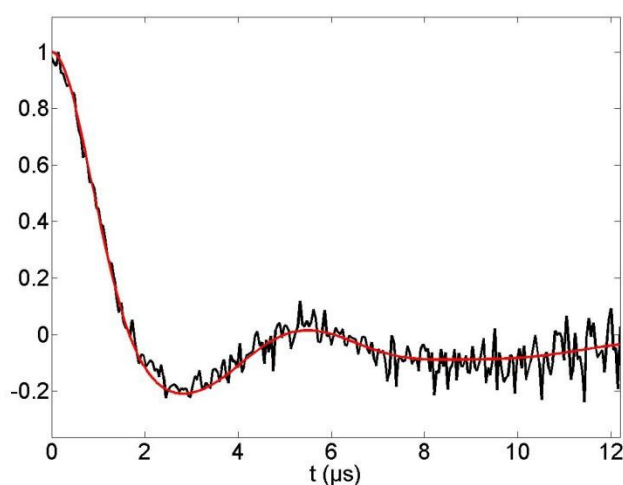


Figure 78 fully corrected 7-pulse signal (black) and Tikhonov regularization from DeerAnalysis [55] (red). Based on the L-curve criterion [64] a regularization parameter of 100 was chosen.

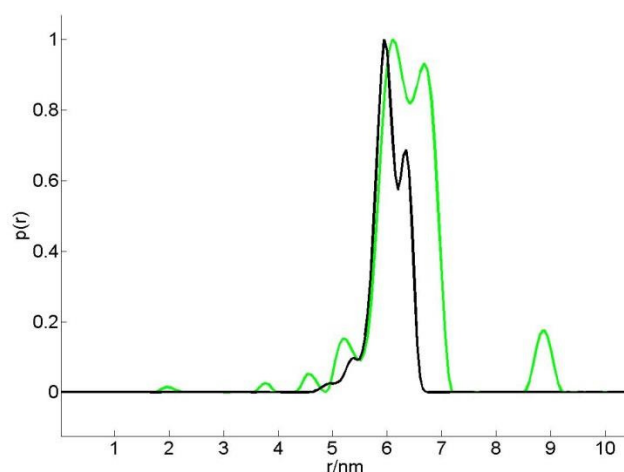


Figure 79 Comparison of the distance distributions obtained by MMM (multiscale modeling of macromolecular systems) from crystal structure 4DOJ.pdb(black) with the distance distribution obtained from the 7-pulse experiment by Tikhonov regularization (green).

6.3.9 3-Spin Effects

It is well known that for more than two spin labels per molecule also the sum and difference frequencies of the dipolar couplings occur, depending on the labeling efficiency and the inversion probabilities of the pump pulses λ and p . This can cause artifacts in the Tikhonov regularization and lead to ghost peaks in the distance distribution[57]. To test if in this case the 3-spin effects are negligible the following procedure was applied: The distance distribution obtained for the iteratively corrected 7-pulse signal for two spins was used to simulate the intramolecular 7-pulse signal taking into account the labeling efficiency of 0.85, the lambda parameter of 0.42 and the multi-flip probability p of 0.78. The 3-spin signal is then approximated by the square of the 2-spin signal. In Figure 80 the simulated 2 (blue)- and 3 (red)- spin signals are shown. For better comparability the 2-spin signal has been scaled to the modulation depth of the 3-spin signal (green). The Difference is below the S/N of the experiment allowing to neglect three-spin effects.

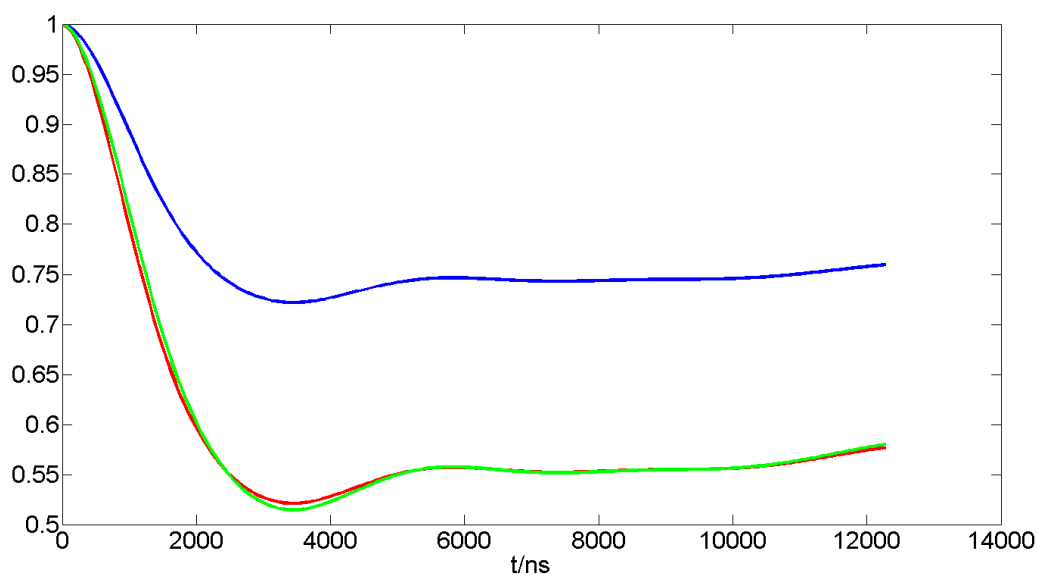


Figure 80 simulated 2-spin signal (blue) of the distance distribution shown in Figure 9 in the main article. The 3-spin signal (green) is the squared 2-spin signal. The 2-spin signal scaled to the modulation depth of the 3-spin signal is shown in red.

7 Conclusion and Outlook

In this work, for the first time, amplitude and phase modulated microwave pulses have been successfully applied in pulse EPR spectroscopy at X- and Q-band frequencies.

A dual channel AWG (arbitrary waveform generator) operating on a 1 ns time scale with 14-bit amplitude resolution which drives an IQ-modulator was implemented into a Bruker E580 pulse EPR spectrometer. In a first attempt excitation profiles of OCT (optimum control theory) derived pulses have been measured and showed substantial gain in excitation bandwidth compared to rectangular pulses. The experiments on OCT derived prefocused pulses showed that pulse distortions originating from the microwave resonator and other bandwidth limited components can cause severe deviations from the expected performance. The impulse response function of the whole spin excitation part was measured by means of a pseudo-stochastically sequence. Pulses optimized with the response function taken into account showed improved performance.

Adiabatic pulses have been applied as pump pulses for PELDOR (pulsed electron double resonance) spectroscopy. A significant increase in modulation depth and therefore S/N ratio was achieved. The problem of signal rounding for small distances induced by the resonance frequency dependent time of inversion was solved by a new 5-pulse PELDOR sequence incorporating two adiabatic pump pulses with opposed sweep direction.

The remarkable performance and efficiency of the sech/tanh inversion pulse led to the development of a CPMG PELDOR experiment for enhanced dipolar window. The 7-pulse PELDOR sequence with three sech/tanh pump pulses enabled to measure the distance distribution between the single spin labeled protomers of the trimeric betaine transporter BetP in frozen detergent with the necessary accuracy to show significant deviations from previous 2 and 3-dimensional X-ray structures.

Shaped pulses show in several potential issues compared to their classical counterpart. By increasing the bandwidth or efficiency in a certain range while keeping the max B_1 amplitude the pulses need to become longer. In all cases a substantial increase in pulse length causes a reduced S/N or a shorter time window of the experiment due to phase relaxation. The performance gain achieved by a shaped pulse has to compensate for that. Pulse distortions arising from the limited bandwidth of the microwave components in the spin excitation path are of course present since spectrometers are optimized for rectangular pulses. Future work

will not only comprise the development of new pulse schemes but will also adapt the hardware to the new possibilities. A first and important step will be the development of new microwave resonators with better B_1 homogeneity and higher bandwidth. Since the topic is still rather new a wide field of future possibilities for improved performance or totally new experiments may arise. A key application might be the development of UR (Universal Rotation) 90° and 180° pulses for EPR as building blocks for a broadband Hahn Echo or a the DQC (double quantum coherence) experiment for distance measurements. Pulses which compensate for a very large B_1 inhomogeneity might be useful to increase the performance of existing hardware. With that being said shaped pulses may never completely replace rectangular pulses but they will be a major part of future development in pulse EPR. At the time this is written Bruker already offers pulse EPR spectrometers with build in AWG's triggered by insights gained in this study.

8 References

- [1] A. Schweiger, Puls-Elektronenspinresonanz-Spektroskopie: Grundlagen, Verfahren und Anwendungsbeispiele, *Angewandte Chemie*, 103 (1991) 223-250.
- [2] A.P. Todd, J. Cong, F. Levinthal, C. Levinthal, W.L. Hubell, Site-directed mutagenesis of colicin E1 provides specific attachment sites for spin labels whose spectra are sensitive to local conformation, *Proteins: Structure, Function, and Bioinformatics*, 6 (1989) 294-305.
- [3] T. Prisner, O. Dobbert, K.P. Dinse, FT ESR Study of Photoinduced Electron Transfer, *J. Am. Chem. Soc.*, 110 (1988) 1622-1623.
- [4] A.D. Milov, A.B. Ponomarev, Y.D. Tsvetkov, Electron-electron double resonance in electron spin echo: Model biradical systems and the sensitized photolysis of decalin, *Chemical Physics Letters*, 110 (1984) 67-72.
- [5] R.G. Larsen, D.J. Singel, Double electron--electron resonance spin--echo modulation: Spectroscopic measurement of electron spin pair separations in orientationally disordered solids, *The Journal of Chemical Physics*, 98 (1993) 5134-5146.
- [6] G. Jeschke, Determination of the Nanostructure of Polymer Materials by Electron Paramagnetic Resonance Spectroscopy, *Macromol. Rapid. Commun.*, 23 (2002) 227-246.
- [7] H.-J. Steinhoff, N. Radzwill, W. Thevis, V. Lenz, D. Brandenburg, A. Antson, G. Dodson, A. Wollmer, Determination of interspin distances between spin labels attached to insulin: comparison of electron paramagnetic resonance data with the x-ray structure, *Biophys. J.*, 73 (1997) 3287-3298.
- [8] W.L. Hubbell, D.S. Cafiso, C. Altenbach, Identifying conformational changes with site-directed spin labeling, *Nat Struct Mol Biol*, 7 (2000) 735-739.
- [9] R.E. Martin, M. Pannier, F. Diederich, V. Gramlich, M. Hubrich, H.W. Spiess, Determination of End-to-End Distances in a Series of TEMPO Diradicals of up to 2.8 nm Length with a New Four-Pulse Double Electron Electron Resonance Experiment, *Angewandte Chemie International Edition*, 37 (1998) 2833-2837.
- [10] M. Pannier, V. Schädler, M. Schöps, U. Wiesner, G. Jeschke, H.W. Spiess, Determination of Ion Cluster Sizes and Cluster-to-Cluster Distances in Ionomers by Four-

Pulse Double Electron Electron Resonance Spectroscopy, *Macromolecules*, 33 (2000) 7812-7818.

[11] S. McDonald, W.S. Warren, Uses of shaped pulses in NMR: A primer, *Concepts in Magnetic Resonance*, 3 (1991) 55-81.

[12] K. Kobzar, B. Luy, N. Khaneja, S.J. Glaser, Pattern pulses: design of arbitrary excitation profiles as a function of pulse amplitude and offset, *Journal of Magnetic Resonance*, 173 (2005) 229-235.

[13] N. Khaneja, F. Kramer, S.J. Glaser, Optimal Experiments for Maximizing Coherence Transfer Between Coupled Spins, *J. Magn. Reson.*, 173 (2005) 116-124.

[14] M. Braun, S.J. Glaser, Cooperative Pulses, *J. Magn. Reson.*, 207 (2010) 114-123.

[15] N.I. Gershenson, T.E. Skinner, B. Brutscher, N. Khaneja, M. Nimbalkar, B. Luy, S.J. Glaser, Linear Phase Slope in Pulse Design: Application to Coherence Transfer, *J. Magn. Reson.*, 192 (2008) 235-243.

[16] K. Kobzar, T.E. Skinner, N. Khaneja, S.J. Glaser, B. Luy, Exploring the Limits of Broadband Excitation and Inversion Pulses, *J. Magn. Reson.*, 170 (2004) 236-243.

[17] K. Kobzar, T.E. Skinner, N. Khaneja, S.J. Glaser, B. Luy, Exploring the Limits of Excitation and Inversion Pulses II. RF-Power Optimized Pulses, *J. Magn. Reson.*, 194 (2008) 58-66.

[18] M.R. Fuchs, T.F. Prisner, K. Möbius, A high-field/high-frequency heterodyne induction-mode electron paramagnetic resonance spectrometer operating at 360 GHz, *Review of Scientific Instruments*, 70 (1999) 3681-3683.

[19] P.A.S. Cruickshank, D.R. Bolton, D.A. Robertson, R.I. Hunter, R.J. Wylde, G.M. Smith, A kilowatt pulsed 94GHz electron paramagnetic resonance spectrometer with high concentration, high sensitivity, high instantaneous bandwidth, and low deadtime, *Rev. Sci. Instrum.*, 80 (2009).

[20] D. Rosenfeld, Y. Zur, Is the sech/tanh Adiabatic Pulse Really Adiabatic?, *Journal of Magnetic Resonance*, 132 (1998) 102-108.

[21] M.S. Silver, R.I. Joseph, D.I. Hoult, Selective spin inversion in nuclear magnetic resonance and coherent optics through an exact solution of the Bloch-Riccati equation, *Phys. Rev. A*, 31 (1985) 2753-2755.

[22] E. Kupče, R. Freeman, Adiabatic Pulse for Wideband Inversion and Broadband Decoupling

J. Magn. Reson., 115 (1995) 273-276.

[23] M. Pannier, S. Veit, A. Godt, G. Jeschke, H.W. Spiess, Dead-Time Free Measurement of Dipole-Dipole Interactions between Electron Spins, *Journal of Magnetic Resonance*, 142 (2000) 331-340.

[24] E.L. Hahn, Spin Echoes, *Physical Review*, 80 (1950) 580-594.

[25] A. Marko, V. Denysenkov, T.F. Prisner, Out-of-phase PELDOR, *Molecular Physics*, 111 (2013) 2834-2844.

[26] V.V. Kurshev, T. Ichikawa, Effect of spin flip-flop on electron-spin-echo decay due to instantaneous diffusion, *Journal of Magnetic Resonance* (1969), 96 (1992) 563-573.

[27] A.M. Tyryshkin, S. Tojo, J.J.L. Morton, H. Riemann, N.V. Abrosimov, P. Becker, H.-J. Pohl, T. Schenkel, M.L.W. Thewalt, K.M. Itoh, S.A. Lyon, Electron spin coherence exceeding seconds in high-purity silicon, *Nat Mater*, 11 (2012) 143-147.

[28] G. Jeschke, Distance Measurements in the Nanometer Range by Pulse EPR, *ChemPhysChem*, 3 (2002) 927-932.

[29] S.A. Dzuba, Librational motion of guest spin probe molecules in glassy media, *Physics Letters A*, 213 (1996) 77-84.

- [30] A.N.A. Zecevic, G.R. Eaton, S.S. Eaton, M. Lindgren, Dephasing of electron spin echoes for nitroxyl radicals in glassy solvents by non-methyl and methyl protons, *Molecular Physics*, 95 (1998) 1255-1263.
- [31] V. Kathirvelu, C. Smith, C. Parks, M.A. Mannan, Y. Miura, K. Takeshita, S.S. Eaton, G.R. Eaton, Relaxation rates for spirocyclohexyl nitroxyl radicals are suitable for interspin distance measurements at temperatures up to about 125 K, *Chemical Communications*, (2009) 454-456.
- [32] M. Lindgren, G. R. Eaton, S. S. Eaton, B.-H. Jonsson, P. Hammarstrom, M. Svensson, U. Carlsson, Electron spin echo decay as a probe of aminoxyl environment in spin-labeled mutants of human carbonic anhydrase II [dagger], *Journal of the Chemical Society, Perkin Transactions 2*, (1997) 2549-2554.
- [33] H.Y. Carr, E.M. Purcell, Effects of Diffusion on Free Precession in Nuclear Magnetic Resonance Experiments, *Physical Review*, 94 (1954) 630-638.
- [34] S. Meiboom, D. Gill, Modified Spin-Echo Method for Measuring Nuclear Relaxation Times, *Review of Scientific Instruments*, 29 (1958) 688-691.
- [35] A. Doll, S. Pribitzer, R. Tschaggelar, G. Jeschke, Adiabatic and fast passage ultra-wideband inversion in pulsed EPR, *Journal of Magnetic Resonance*, 230 (2013) 27-39.
- [36] C. Kröhnke, V. Enkelmann, G. Wegner, Radikalkationensalze einfacher Arene – eine neue Familie „organischer Metalle“, *Angewandte Chemie*, 92 (1980) 941-942.
- [37] G. Sachs, W. Stöcklein, B. Bail, E. Dormann, M. Schwoerer, Electron spin relaxation of new organic conductors: fluoranthenyl radical cation salts, *Chemical Physics Letters*, 89 (1982) 179-182.
- [38] T.E. Skinner, T.O. Reiss, B. Luy, N. Khaneja, S.J. Glaser, Application of Optimal Control Theory to the Design of Broadband Excitation Pulses for High Resolution NMR, *J. Magn. Reson.*, 163 (2003) 8-15.
- [39] P.E. Spindler, Y. Zhang, B. Endeward, N. Gershernzon, T.E. Skinner, S.J. Glaser, T.F. Prisner, Shaped optimal control pulses for increased excitation bandwidth in EPR, *Journal of Magnetic Resonance*, 218 (2012) 49-58.
- [40] D.D. Rife, J. Vanderkooy, Transfer-Function Measurement with Maximum-Length Sequences, *J. Audio Eng. Soc.*, 37 (1989) 419-444.
- [41] L.G. Rowan, E.L. Hahn, W.B. Mims, Electron-Spin-Echo Envelope Modulation, *Physical Review*, 137 (1965) A61-A71.
- [42] W.B. Mims, Envelope Modulation in Spin-Echo Experiments, *Physical Review B*, 5 (1972) 2409-2419.
- [43] Z. Yang, J. Becker, S. Saxena, On Cu(II)–Cu(II) distance measurements using pulsed electron double resonance, *Journal of Magnetic Resonance*, 188 (2007) 337-343.
- [44] I.M.C. van Amsterdam, M. Ubbink, G.W. Canters, M. Huber, Measurement of a Cu–Cu Distance of 26 Å by a Pulsed EPR Method, *Angewandte Chemie International Edition*, 42 (2003) 62-64.
- [45] B.E. Bode, J. Plackmeyer, T.F. Prisner, O. Schiemann, PELDOR measurements on a nitroxide-labeled Cu(II) porphyrin: Orientation selection, spin-density distribution, and conformational flexibility, *J. Phys. Chem. A*, 112 (2008) 5064-5073.
- [46] C. Elsässer, M. Brecht, R. Bittl, Pulsed Electron-Electron Double Resonance on Multinuclear Metal Clusters: Assignment of Spin Projection factors Based on the Dipolar Interaction *J. Am. Chem. Soc.*, 124 (2002) 12606-12611.
- [47] M.M. Roessler, M.S. King, A.J. Robinson, F.A. Armstrong, J. Harmer, J. Hirst, Direct assignment of EPR spectra to structurally defined iron-sulfur clusters in complex I by double electron–electron resonance, *Proceedings of the National Academy of Sciences*, 107 (2010) 1930-1935.

- [48] A.M. Raitsimring, C. Gunanathan, A. Potapov, I. Efremenko, J.M.L. Martin, D. Milstein, D. Goldfarb, Gd³⁺ Complexes as Potential Spin Labels for High Field Pulsed EPR Distance Measurements, *Journal of the American Chemical Society*, 129 (2007) 14138-14139.
- [49] A. Potapov, H. Yagi, T. Huber, S. Jergic, N.E. Dixon, G. Otting, D. Goldfarb, Nanometer-Scale Distance Measurements in Proteins Using Gd³⁺ Spin Labeling, *Journal of the American Chemical Society*, 132 (2010) 9040-9048.
- [50] P. Lueders, G. Jeschke, M. Yulikov, Double Electron–Electron Resonance Measured Between Gd³⁺ Ions and Nitroxide Radicals, *The Journal of Physical Chemistry Letters*, 2 (2011) 604-609.
- [51] D. Banerjee, H. Yagi, T. Huber, G. Otting, D. Goldfarb, Nanometer-Range Distance Measurement in a Protein Using Mn²⁺ Tags, *The Journal of Physical Chemistry Letters*, 3 (2011) 157-160.
- [52] Y. Asada, R. Mutoh, M. Ishiura, H. Mino, Nonselective excitation of pulsed ELDOR using multi-frequency microwaves, *Journal of Magnetic Resonance*, 213 (2011) 200-205.
- [53] P.E. Spindler, S.J. Glaser, T.E. Skinner, T.F. Prisner, Broadband Inversion PELDOR Spectroscopy with Partially Adiabatic Shaped Pulses, *Angewandte Chemie International Edition*, 52 (2013) 3425-3429.
- [54] M.K. Bowman, A.G. Maryasov, Dynamic phase shifts in nanoscale distance measurements by double electron electron resonance (DEER), *Journal of Magnetic Resonance*, 185 (2007) 270-282.
- [55] G. Jeschke, V. Chechik, P. Ionita, A. Godt, H. Zimmermann, J. Banham, C.R. Timmel, D. Hilger, H. Jung, DeerAnalysis2006 - a comprehensive software package for analyzing pulsed ELDOR data, *Appl. Magn. Reson.*, 30 (2006) 473-498.
- [56] P.P. Borbat, E.R. Georgieva, J.H. Freed, Improved Sensitivity for Long-Distance Measurements in Biomolecules: Five-Pulse Double Electron–Electron Resonance, *The Journal of Physical Chemistry Letters*, 4 (2012) 170-175.
- [57] G. Jeschke, M. Sajid, M. Schulte, A. Godt, Three-spin correlations in double electron-electron resonance, *Physical Chemistry Chemical Physics*, 11 (2009) 6580-6591.
- [58] S. Ressler, A.C. Terwisscha van Scheltinga, C. Vonrhein, V. Ott, C. Ziegler, Molecular basis of transport and regulation in the Na⁺/betaine symporter BetP, *Nature*, 458 (2009) 47-52.
- [59] C. Perez, C. Koshy, S. Ressler, S. Nicklisch, R. Krämer, C. Ziegler, Substrate specificity and ion coupling in the Na⁺/betaine symporter BetP, *The EMBO Journal*, 30 (2011) 1221-1229.
- [60] G. Jeschke, C. Wegener, M. Nietschke, H. Jung, H.-J. Steinhoff, Interresidual Distance Determination by Four-Pulse Double Electron-Electron Resonance in an Integral Membrane Protein: The Na⁺/Proline Transporter PutP of *Escherichia coli*, *Biophysical Journal*, 86 (2004) 2551-2557.
- [61] Y. Polyhach, E. Bordignon, G. Jeschke, Rotamer libraries of spin labelled cysteines for protein studies, *Phys. Chem. Chem. Phys.*, 13 (2011) 2356-2366.
- [62] G. Jeschke, Y. Polyhach, Distance measurements on spin-labelled biomacromolecules by pulsed electron paramagnetic resonance, *Phys. Chem. Chem. Phys.*, 9 (2007) 1895-1910.
- [63] Y. Polyhach, E. Bordignon, G. Jeschke, Rotamer libraries of spin labelled cysteines for protein studies, *Physical Chemistry Chemical Physics*, 13 (2011) 2356-2366.
- [64] Y.-W. Chiang, P.P. Borbat, J.H. Freed, The determination of pair distance distributions by pulsed ESR using Tikhonov regularization, *Journal of Magnetic Resonance*, 172 (2005) 279-295.

9 Acknowledgement

I am deeply indebted to my supervisor Prof. Thomas Prisner who not only gave me the opportunity to work on this challenging and exciting topic but who also always had an open ear for discussions where he willingly shared his expertise and knowledge in spectrometer related hardware and spin physics.

I am also indebted to Dr. Burkhard Endeward who introduced me to the eEPR-spectrometers and with whom I performed my first EPR experiments. Burkhard helped me a lot to understand the principles of EPR spectroscopy and the underlying hardware. I thank him for the constant support theoretically as well as technically.

I thank Prof. Steffen Glaser from the TU Munich and Prof. Thomas Skinner from the Wright State University Ohio for providing me with the optimum control theory derived pulses. I thank Prof. Steffen Glaser and Prof. Thomas Skinner for the very fruitful and long discussions. I especially thank Prof. Thomas Skinner for providing me with the truncated sech/tanh pulse which was used for first broadband inversion PELDOR experiment.

I thank Dr. Jörn Plackmeyer for the synthesis of model compounds which have been of great usefulness during my whole work.

I thank the whole group present members and those who have left during my time for their friendliness and support.

10 List of Figures

- Figure 1 Shape of a CAP pulse according to Equation (2.1) utilizing an excitation field of 25 MHz and a duration of 2000 ns. 21
- Figure 2 Trajectory of an on resonant spin with the CAP pulse shown in Figure 1. 22
- Figure 3 Trajectory of an on resonant spin with the CAP pulse shown in Figure 1 in the frequency frame. 22
- Figure 4 sech/tanh inversion pulse with $\beta = 10.6/T$; $T=800\text{ns}$, $B_{1\text{max}}=25\text{ MHz}$ and $\text{BW}=100\text{ MHz}$. 24
- Figure 5 inversion profile of the sech/tanh pulse shown in Figure 4. 25
- Figure 6 WURST pulse with $k=0.7\text{ MHz/ns}$, $B_{1\text{max}}=25\text{ MHz}$, $n=80$. 27
- Figure 7 Inversion bandwidth comparison of a sech/tanh inversion pulse (blue) with a WURST pulse utilizing the same power and duration. 28
- Figure 8 Sech/tanh inversion pulse used for the comparison shown in Figure 7. The pulse is slightly truncated to increase bandwidth and efficiency. 29
- Figure 9 dipolar coupled spin pair for PELDOR spectroscopy. θ is the angle between the static magnetic field \vec{B}_0 and the interspin vector \vec{r} . 30
- Figure 10 3-pulse PELDOR sequence. A two pulse Hahn Echo sequence is applied on the observer frequency ν_A whereas a single inversion pulse is applied on the B-spin frequency ν_B in the first τ -period. 31
- Figure 11 Pake doublet. 33
- Figure 12 CPMG sequence. For EPR applications an equal spacing between the refocusing pulses may be not appropriate due to overlap with echoes resulting from an inhomogeneous line comparable to the excitation bandwidth of the pulses. 36
- Figure 13 Echoes of a sample containing protons after roughly 20 μs . The blue line is recorded with one refocusing pulse, the green with two and the red signal was created with three refocusing pulses. In case of one refocusing pulse the echo should appear between 19.6 μs and 20 μs but is not observed in the noise. The green echo appears at 19.7 μs whereas the red echo appears after 19.8 μs . 38
- Figure 14 conventional pulsed EPR spectrometers use fast microwave switches to generate pulses. 39
- Figure 15 amplitude modulation of microwave (LO) by an control voltage (AWG) 39
- Figure 16 arbitrary amplitude and phase setup with two modulators driven by LO's which differ in phase by 90° . 40
- Figure 17 block diagram of the pulse-shaping unit 41
- Figure 18 The pulse-shaping unit connected to the ELDOR source for PELDOR applications 41
- Figure 19 setup to generate shaped pulses while maintaining the standard +x, -x +y, -y channels. 44
- Figure 20 setup to generate shaped pulses using the amplitude and phase network of the microwave bridge as LO source 45
- Figure 21 setup for shaped ELDOR pulses 46
- Figure 22 Bebob pulse originally optimized for 50 MHz bandwidth and duration 2000 ns with peak B_1 of 3 MHz rescaled to a bandwidth of 200 MHz and a duration of 500 ns with peak B_1 of 12 MHz. 50

Figure 23 [37] comparison of a 200 MHz bebop pulse with a rectangular pulse utilizing the same peak B_1 field of 12 MHz. 52

Figure 24 PNT radical. 53

Figure 25 [37] Magnitude Fourier transform spectra of 1 mM PNT in paraffin oil measured at room temperature. Stick diagram of hyperfine spectra (a). Experimental spectra excited in the center of the EPR spectra with the bebop pulse (b) and with a 21 ns 90° pulse(c). Experimental spectra excited 53 MHz off-resonance from the center with the bebop (d) and with a 21 ns 90° pulse (e). 55

Figure 26 excerpt of the 13-bit mls sequence which was actually used to determine the spectrometer response function $h(t)$. The total length of the sequence is $2^{13} = 8192$ ns. 58

Figure 27 Autokorrelation of the 13 bit mls sequence which was used to determine the spectrometer response function $h(t)$. 58

Figure 28 [37] Experimental setup to measure the B_1 field in the stray field of the resonator. 60

Figure 29 The input mls sequence(black) with the measured B_1 response in in-phase(blue) and quadrature component (red). The field pick up coil was brought into the stray field app. 3-5mm above the MD 5 resonator.61

Figure 30 [37] Impulse response function obtained with the 13-bit mls sequence. In-phase component is drawn in solid black quadrature component dashed. 62

Figure 31 [37] Frequency response obtained with the impulse response shown in Figure 30. In phase component (black) and quadrature component (grey). 62

Figure 32 excitation pattern (measured: black) with a simulations taking the impulse response into account (red line) and with the undistorted pulse (blue line). 63

Figure 33 200 MHz prefocused pulse which focuses the transverse magnetization 200 ns after the end of the pulse. Both phases (x:blue; y: red) are shown. 64

Figure 34 [37] compares conventional and optimized pulses designed to acquire signal 200 ns after the end of the last pulse and their offset profiles. The left column rEPresents a conventional echo sequence based on rectangular 90° and 180° pulses. The middle and right columns rEPresent results of optimizations without (middle column) and with (right column) transient effects taken into account in the optimization. The panels in the first (a) and second (b) row show x- (red) and y-(blue) component of simulated input and output pulses, respectively. The third row (c) shows the simulated response for the input pulse (grey curves) and for the output pulse (black curves). Finally, the black curves in the fourth row (d, d', d'') rEPresent the simulated response of the output pulses multiplied by the measured frequency response of the video amplifier. In panels d' and d'', experimental spectra are shown as grey curves. 66

Figure 35 [37] BDPA-echo generated with the prefocused pulse shown in Figure 33. The time when the all magnetization is aligned is 200ns after the end of the pulse. 67

Figure 36 cos-Fourier transform of the BDPA FID generated with a 200 MHz prefocused pulse in comparison to a cw-reference (dashed). 68

Figure 37 simulated FID of the electron proton spin system excited with a 1 ns 90° pulse. 69

Figure 38 simulated FID of the electron proton spin system excited with a 1000 ns prefocused pulse. The maximum of the echo appears at $t = 1200$ ns which is the pulse length plus the delay time of 200 ns. 69

Figure 39 Cosine Fourier transforms of simulated fids for an IS spin system with anisotropic hyperfine coupling once excited by an 1ns 90° pulse (blue) and with a 200 MHz prefocused pulse (red). 70

Figure 40 \vec{B}_0 -field series of an $I=1/2$ $S=1/2$ system with an isotropic g-tensor and an anisotropic hyperfine tensor $A_{xx}= 0$ G; $A_{yy}= 0$ G; $A_{zz}= 20$ G. Shown is the Fourier transform of the simulated FIDs for different static magnetic fields. The blue spectra are obtained with an 1ns 90° excitation pulse whereas the red

spectra are generated with a 200 MHz prefocused optimum control pulse. The optimum control pulse was optimized assuming only isotropic Zeeman interaction. 71

Figure 41 4-pulse PELDOR sequence. The shaped pump pulse is sketched as red boxes with a length T_{pump} . The two boxes represent the position of the pulse at the beginning and at the end of the PELDOR timetrace. The maximum dipolar evolution time is: $T_{\text{max}} = \tau_2 - T_{\text{pump}} - \frac{L_{\pi A}}{2}$ with $L_{\pi A}$ being the length of the A-spin refocusing pulse. 73

Figure 42 [51] Truncated sech/tanh inversion pulse used as a pump pulse for PELDOR spectroscopy. X-component (black) and Y-component (grey) are depicted. 74

Figure 43 [51] Inversion profile of the 200 ns sech/tanh pump pulse (black) compared to a 20 ns rectangular shaped inversion pulse using the same peak B_1 -field of 8.9 G. 75

Figure 44 [51] PELDOR timetrace of the biradical shown as inset. The 200 ns sech/tanh pump pulse (solid) achieves a 2.5 times higher modulation depth than the 20 ns rectangular pump pulse (dotted). 76

Figure 45 [51] Pump and probe position of in case of the sech/tanh pump pulse. 77

Figure 46 [51] Distance analysis of the nitroxide biradical obtained with DeerAnalysis[53] 78

Figure 47 [51] Echo detected field sweep spectrum of the Co-NO biradical shown. The shot repetition time was set to 0.5 ms to partially saturate the nitroxide. The pump –probe positions for the PELDOR experiments performed on this system are approximate 600 MHz apart. 79

Figure 48 [51] Top: PELDOR timetraces of the Co-NO system (Figure 47) obtained with a 150 MHz sech/tanh pump pulse (solid) and with a 20 ns rectangular pump pulse (dotted). Bottom left : Fourier transform of the dipolar evolution after correction of the intermolecular background. Bottom right: distance distributions obtained with Tikhonov regularization by Deer Analysis[53]. 80

Figure 49 [51] time and offset dependent M_z profile for the 150 MHz sech/tanh inversion pulse. 81

Figure 50 [51] red : PELDOR timetrace recorded with a 20 ns rectangular pump pulse. Blue: renormalized superposition of red timetraces which zero point is time shifted over a 90 ns window. 82

Figure 51 Novel 5-pulse PELDOR sequence for offset independent dipolar evolution time T is incremented during the experiment while T' is fixed. 83

Figure 52 [51] solid: 5-pulse PELDOR measurement on Co-NO system with two 150 MHz sech/tanh pump pulses. Grey: 4-pulse PELDOR measurement with one 150 MHz sech/tanh pump pulse. 85

Figure 53 [51] Black: 5-pulse Co-NO PELDOR signal obtained with a 150 MHz sech/tanh first pulse and a 225 MHz second pump pulse. Grey: 5-pulse signal obtained with two 150 MHz sech/tanh pump pulses. 86

Figure 54 Bandwidth comparison of the sech/tanh pump pulses used for 5-pulse PELDOR. 86

Figure 55 [51] Top: PELDOR timetraces of the Co-nitroxide biradical the normalized PELDOR timetraces recorded with a 20ns rectangular pump pulse (solid) or with the adiabatic pump pulse (dash) are shown. Bottom: The Fourier transformations for both cases as well as the distance distributions[17] are depicted. The less well resolved dipolar Pake pattern for the adiabatic pulse PELDOR (dashed) is clearly visible. 87

Figure 56 5-pulse PELDOR timetrace on Co-NO biradical obtained with two 20 ns 180° pulses as pump pulses. The time zero of the 5-pulse signal is at $t = 1000$ ns. 88

Figure 57 [51] Distance analysis of cobalt nitroxide biradical obtained with DeerAnalysis[53] 88

Figure 58 inversion profiles for three inversion pulses utilizing the same microwave power. The WURST pulses are applied as PELDOR pump pulses in a 5-pulse sequence. Black: rectangular shaped 20 ns pulse; blue 400 MHz broad 400 ns WURST pulse; red: 500 MHz broad 480 ns long WURST pulse. 90

Figure 59 Pulseshape of the 400 ns 400 MHz WURST pulse used as moving pump pulse in the new 5-pulse sequence. 90

Figure 60 Black: 4-pulse PELDOR timetrace on Co-NO system recorded with a 20 ns rectangular pump pulse. Blue: 5-pulse timetrace recorded with a pair of 400- and 480 MHz WURST pulses. The modulation depth increased by a factor of 7.2. 91

Figure 61 Comparison of dipolar evolution time traces of the BetP trimer obtained with the standard 4-pulse PELDOR sequence (upper two panels) and with the new 7-pulse CP PELDOR sequence (lower two panels). Both experiments are performed at 50 K temperature. The 7-pulse signal was recorded over 2.5 h with a 50 MHz bandwidth sech/tanh pump pulses, whereas the 4 pulse signal was averaged over 1 h and utilized a classical 12 ns rectangular pump pulse. 94

Figure 62 7-pulse PELDOR sequence 96

Figure 63 All possible non-7-pulse pathways which contribute a time dependent signal 98

Figure 64 Crystal structure of BetP (4DOJ.pdb). The rotamers calculated by MMM[59] of the attached nitroxides (NO groups) at residue S140 are shown as balls (red/blue). The α -C's where the MTSSL spin labels are attached are marked as large red spheres. The rotamers have been calculated for a temperature of 298 K to obtain a reasonable population also for the blue protomer. 100

Figure 65 Bandwidth and position of the pump-pulse (red) and probe sequence (32 ns, 48 ns, 48 ns, 48 ns) (black) drawn into the nitroxide pulsed field sweep spectrum at Q-band. 101

Figure 66 7-pulse PELDOR sequence with interpulse delays d1-d7. The initial-delays which had been set for the betp-measurement with a 12.5 μ s time window have been: d₁: 3900 ns; d₂: 64 ns; d₃: 8636 ns; d₄: 64 ns; d₅: 8936 ns; d₆: 64 ns; d₇: 4791 ns; pg: 140 ns (integration window). The video amplifier bandwidth was set to 25 MHz. All pump pulses have been sech/tanh pulses. 102

Figure 67 Shape of the 50 MHz sech/tanh pulses applied in 7-pulse PELDOR at Q-band frequencies. 103

Figure 68 Inversion profiles of the 400 ns sech/tanh inversion pulse (green line) and a rectangular inversion pulse with a duration of 13 ns corresponding to $B_{1,max} = 7.1$ G 103

Figure 69 Two possible ways to conduct a 7-pulse PELDOR measurement. Left: all pump pulses are positioned directly after the refocusing pulses and are incremented to the right. Right: The third pump pulse is positioned left to the third refocusing pulse and incremented to the left. 104

Figure 70 7-pulse PELDOR timetraces for different setups. The green trace is obtained with the incrementation shown in Figure 69 left panel (green) whereas the black trace is obtained with the incrementation shown in the right panel of Figure 69. 105

Figure 71 5-pulse PELDOR on a monoradical in frozen solution. 106

Figure 72 intermolecular decay functions in 7-pulse PELDOR. Orange: 5-pulse background functions; Blue: 4-pulse background function; violet: 7-pulse background function. The red line is the product of all individual background functions and a time independent factor which is then the intermolecular signal for the 7-pulse experiment. The green line shows the experimental signal (black) after background correction. 107

Figure 73 symmetrized background corrected 7-pulse measurement 109

Figure 74 The green trace is resampled by a factor 44/16 to achieve the correct evolution of the 4-pulse trace. 111

Figure 75 The 4-pulse trace is shifted horizontally to its time zero (blue). The green trace is obtained by weighting the blue trace with the probability of the 4-pulse pathway \bar{p}^2 . 112

Figure 76 Corrected timetrace after the first iteration. The first row shows the three five-pulse pathways weighted with their probability. The middle row shows the three six-pulse artifacts weighted with their probability. The green trace is obtained by subtracting the red line which is the sum of the 5 -and 6-pulse traces from the background corrected 7-pulse measurement (black). 112

Figure 77 7-pulse evolution after 20 iterations. The green trace is obtained by subtracting the red line which is the sum of the 5 pulse artifacts (first three traces from bottom) –and the 6-pulse artifacts (three traces underneath the red trace) from the background corrected 7-pulse measurement (black). The dotted lines show the zeroth iteration. 113

Figure 78 fully corrected 7-pulse signal (black) and Tikhonov regularization from DeerAnalysis [53] (red). Based on the L-curve criterion [62] a regularization parameter of 100 was chosen. 114

Figure 79 Comparison of the distance distributions obtained by MMM from crystal structure 4DOJ(black) with the distance distribution obtained from the 7-pulse experiment by Tikhonov regularization (green). 114

Figure 80 simulated 2-spin signal (blue) of the distance distribution shown in Figure 9 in the main article. The 3-spin signal (green) is the squared 2-spin signal. The 2-spin signal scaled to the modulation depth of the 3-spin signal is shown in red. 115

12 Curriculum Vitae

Personal Data

Philipp Emanuel Spindler
Institut für Physikalische und Theoretische Chemie
J.W. Goethe Universität Frankfurt
Max von Laue Str. 7
60438 Frankfurt am Main
philipp@epr.uni-frankfurt.de
Born Sep. 15th 1984 Schrobenhausen, Germany

Education

2010-2014

Johann Wolfgang Goethe Universität
PhD student
Supervisor Prof. Dr. Thomas. Prisner
PhD thesis: Amplitude and phase modulated microwave pulses
for EPR

2004-2010

Technische Universität Kaiserslautern
Diploma in Chemistry , grade 1.0
diploma thesis: "Aufbau und Inbetriebnahme einer magnetischen
Flasche"
Supervised by Prof. Dr. Markus Gerhards

1996-2004

Gymnasium Birkenfeld
Abitur, grade 1.6

14 Publications

- 1) P.E. Spindler, Y. Zhang, B. Endeward, N. Gershernzon, T.E. Skinner, S.J. Glaser, T.F. Prisner, Shaped optimal control pulses for increased excitation bandwidth in EPR, *Journal of Magnetic Resonance*, 218 (2012) 49-58.
- 2) P.E. Spindler, S.J. Glaser, T.E. Skinner, T.F. Prisner, Broadband Inversion PELDOR Spectroscopy with Partially Adiabatic Shaped Pulses, *Angewandte Chemie International Edition*, 52 (2013) 3425-3429.
- 3) P.E. Spindler, I. Waclawska, B. Endeward, E. Schleiff, C. Ziegler, T.F. Prisner, Asymmetry of Betaine Transporter BetP Probed by a CPMG-PELDOR Methode, *Journal of American Chemical Society*, (2014)- **submitted**